ESD-TR-77-169

ADA044309

Technical Note

1977-7

R. A. Goundry
C. J. Kurys

Waveform and Clutter Filter Design for a Satellite-Borne Bistatic Radar for Aircraft Detection

28 June 1977

Prepared for the Defense Advanced Research Projects Agency
under Electronic Systems Division Contract F19628-76-C-0002 by

Lincoln Laboratory
MASSACHUSETTS INSTITUTE OF TECHNOLOGY
LEXINGTON, MASSACHUSETTS

AD NO. DDC FILE COPY

Approved for public release; distribution unlimited.

The work reported in this document was performed at Lincoln Laboratory, a center for research operated by Massachusetts Institute of Technology. This work was sponsored by the Defense Advanced Research Projects Agency under Air Force Contract F19628-76-C-0002 (ARPA Order 600).

This report may be reproduced to satisfy needs of U.S. Government agencies.

The views and conclusions contained in this document are those of the contractor and should not be interpreted as necessarily representing the official policies, either expressed or implied, of the United States Government.

This technical report has been reviewed and is approved for publication.

FOR THE COMMANDER

Raymond L. Loiselle

Raymond L. Loiselle, Lt. Col., USAF
Chief, ESD Lincoln Laboratory Project Office

MASSACHUSETTS INSTITUTE OF TECHNOLOGY

LINCOLN LABORATORY

WAVEFORM AND CLUTTER FILTER DESIGN FOR A SATELLITE-BORNE BISTATIC RADAR FOR AIRCRAFT DETECTION

R. A. GOUNDRY

Group 37

C. J. KURYS

Group 31

TECHNICAL NOTE 1977-7

28 JUNE 1977

DDC

RECEIVED

SEP 1977

B

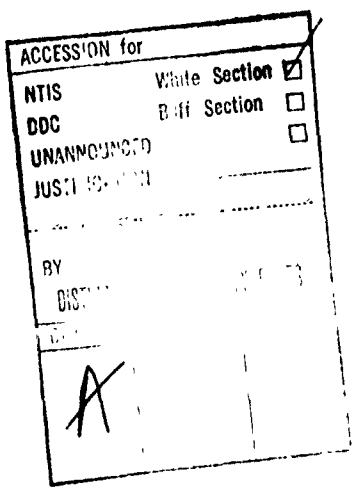
Approved for public release; distribution unlimited.

LEXINGTON MASSACHUSETTS

Preceding Page BLANK - NOT FILMED

ABSTRACT

Waveform and clutter filtering for the detection of moving aircraft in the presence of ground clutter by a space-borne bistatic radar are described. The waveform designs are based on mappings of the aircraft and clutter onto the bistatic range-Doppler plane. Low sidelobe digital filter designs for the required clutter rejection, coverage characteristics of a bistatic radar on representative satellite orbits, and system requirements for a North American surveillance fence for bomber detection are included.



Preceding Page BLANK - FILMED

Contents

	Abstract	iii
I.	Introduction	1
II.	System Requirements	3
	2.1 Fence Configuration	3
	2.2 Typical Aircraft Flight Paths	5
	2.3 Surveillance Time	8
	2.4 Potential Advantages of Bistatic Systems	12
III.	Radar Parameter Estimates	13
	3.1 Search Power-Aperture Product	14
	3.2 Track Power-Aperture Product	19
	3.3 System Realizability	25
IV.	Representative Satellite Orbits	31
	4.1 General Categories	31
	4.2 Virtual Radar Location	31
	4.3 Examples of Coverage	32
V.	Range-Doppler Maps and Waveform Designs	46
	5.1 Doppler Resolution Limitations	49
	5.2 Range Resolution Limitations	51
	5.3 Bistatic Clutter Cross-Section	52
	5.4 Sample Waveforms from Range-Doppler Maps	55
	5.4.1 Low Altitude Satellites	55
	5.4.2 High Altitude Satellites	72

VI. Filter Design 82

6.1 Waveform Weighting 82

6.1.1 Hamming Weighting 83

6.1.2 Weights from Digital Filter Design 84

6.2 Implementation Considerations 88

VII. Summary and Recommendations 94

Appendix A Bistatic R-Ṙ Maps 96

A.1 Bistatic Range and Range Gradient 96

A.2 Bistatic Angles 102

A.3 Clutter Density in the R-Ṙ Plane 102

A.4 Example Mappings onto the R-Ṙ Plane 111

Appendix B Range Gating Ground Clutter in a Monostatic Satellite-Bourne Radar 123

B.1 Geometry 123

B.2 Mathematical Development 126

B.3 Discussion of Results 132

B.4 Summary 133

References 144

I. INTRODUCTION

A satellite-borne radar system for aircraft detection will be viewing targets against the background of the earth (ground clutter) for most viewing geometries. A bistatic radar system may offer the potential for target cross section enhancement and clutter cross section reduction by virtue of the viewing geometry. Whether this potential exists would have to be established by measurements. A performance measure of a radar system is its ability to detect targets in a cluttered environment by either avoiding or suppressing the clutter. Clutter suppression can be achieved through a judicious choice of waveform and filter design. This report presents the results of an investigation of waveform design and clutter filtering techniques for use in a satellite-borne bistatic radar for aircraft detection.

System requirements for detection of a Soviet bomber attack on the United States are presented and the potential advantages of a bistatic radar system over a monostatic radar system are reviewed. Estimates of the power-aperture required of a satellite-borne bistatic radar system to provide various coverage rates are made to indicate the relative size of the system. Any satellite-borne sensor system requires communication and ground control centers which make use of the information gathered by the system. These issues are recognized but were not investigated since they do not impact the investigation of

waveforms and clutter filtering.

A satellite-borne bistatic radar system requires two satellites, one for the transmitter and one for the receiver. Two satellites in the same or different orbits can provide unique coverage of certain portions of the earth that cannot be provided by a monostatic system. Representative orbits and satellite configurations are analyzed which provide coverage of a surveillance fence deployed along a constant latitude. These orbits are used to generate bistatic range-Doppler maps of the ground clutter and of aircraft on representative flight paths through the surveillance fence. Range-Doppler maps of the clutter and aircraft form the basis for waveform design. The examples considered indicate that on the order of 60 dB of clutter rejection is needed. Analog filter techniques have been able to achieve sidelobe responses ~40 dB below the main lobe response. Advances in digital filtering techniques indicate sidelobe levels much lower than 40 dB below the main lobe response of the waveform ambiguity function are possible. Examples of waveforms are presented which, with suitable weighting, could provide clutter rejection on the order of the needed 60 dB.

II. SYSTEM REQUIREMENTS

The objectives of this surveillance system are to search for, detect and track hostile aircraft approaching the North American continent. The primary approach corridor can be considered to be from the Soviet Union over the polar region to North America. Two additional attack corridors could also exist from the broad ocean areas east and west of CONUS. Use of these corridors by the Soviet Union requires a large scale refuel operation over the broad ocean areas. Coverage of them is considered a secondary issue. They could be covered at the expense of increasing the system capability.

The amount of warning time required of a surveillance system is a function of many variables. Some of these variables are attacking aircraft velocity, interceptor velocity, interceptor reaction time, minimum distance from CONUS where an intercept engagement may occur, etc. We chose arbitrarily that the near edge of the surveillance fence be at least 500 nautical miles from CONUS.

2.1 Fence Configuration

The surveillance required to meet the objectives of searching for, detecting and tracking aircraft approaching North America could be provided by many configurations of fences. This analysis will attempt to evaluate the placement of a fence which

would be capable of intercepting a major portion of threatening aircraft flight paths to North America. The East - West (width) extent of the fence depends on which flight paths into North America must be detected. A requirement also to detect flights from Europe and South America, for example, would require a fence be constructed which completely encircles North America. The width of the fence depends on aircraft velocity and revisit search time. The distance between the fence and the border of North America is determined by the desired warning time and aircraft velocity.

The primary aircraft threat considered in this analysis is an USSR long range bomber force. The Soviet airfields which are suitable for and capable of serving as launching and staging areas for an attack against North America extend across the entire continent of Asia from 23^{o} to 177^{o} East Longitude. A wide range of attack azimuths could be employed against North American targets which places severe constraints on a fence configuration and location.

A bistatic satellite-borne radar system places further constraints on the type of fence that can be constructed. The satellites must be placed in high altitude orbits to obtain long viewing times of the fence with a minimum number of satellites. A low altitude orbit will require a much larger number of satellites, which tends to increase the complexity and cost but allows a

graceful degradation of overall system performance if some satellites are lost. In addition, a requirement for a constant bistatic angle or small range of bistatic angles as the fence is searched will place constraints on the placement and configuration of the surveillance fence.

2.2 Typical Aircraft Flight Paths

The threat considered for this analysis consists of USSR based aircraft attacking CONUS. The threat may be either a single aircraft, a squadron or a massive coordinated attack The Surveillance system should accommodate any size of attack. Without attempting to establish likely paths between USSR airfields and CONUS strategic targets, we considered only great circle paths from northern USSR to CONUS. Flight paths over the broad ocean areas with in-flight refueling are a possibility. A system designed to include these cases will require additional capacity, depending on the additional volume to be searched. It is possible that the terminal phase of the flight might occur at a low altitude and supersonic velocities; however, this should not affect our analysis in any significant manner.

The aircraft will be assumed to fly at a nominal cruise altitude, (~10 km) and cruise velocity (925 km/hr.). Table 1-1 is a matrix of flight paths chosen to represent typical attack azimuths. Figure II-1 shows the locations of the targets and the nominal origin of the aircraft (airfield) with a straight line

TABLE I-1

THREAT SCENARIO

Flight Path	Airfield		Target		Range (km)
	Latitude ^{O}N	Longitude ^{O}E	Latitude ^{O}N	Longitude ^{O}E	
1	55	157	35	-120	6475
2	55	157	35	- 75	8850
3	65	75	40	-105	8350
4	55	30	35	-120	9610
5	30	30	35	- 70	7750

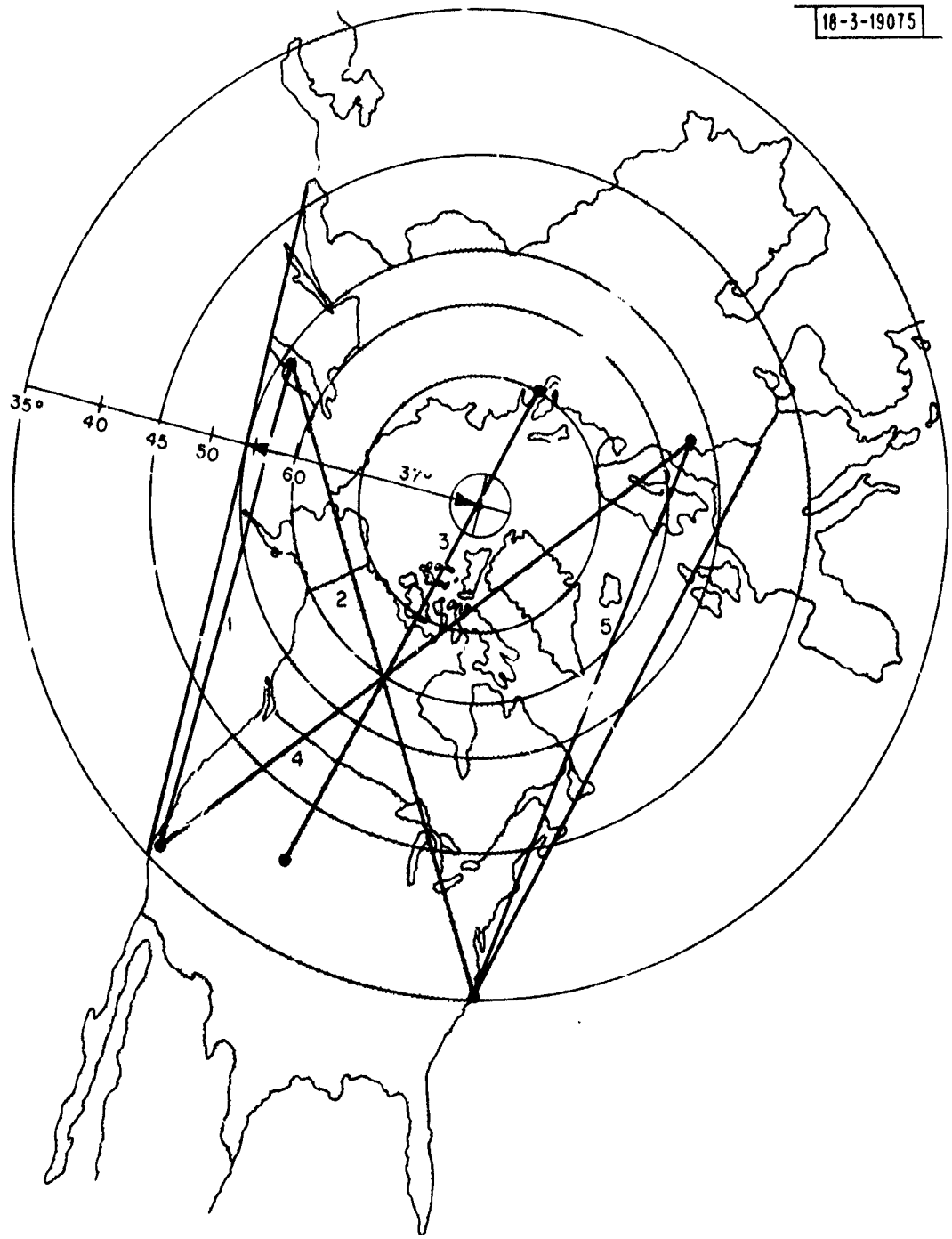


Fig. II-1. Typical aircraft flight paths.

joining the target and airfield. Table 1 also contains the great circle distance between the targets and airfields.

2.3 Surveillance Time

One of the parameters in the radar equation which determines system performance is the solid angle search rate. A large solid angle search rate requires large power-aperture products. In this section we attempt to minimize the search rate requirements consistent with the objectives of the surveillance system.

An aircraft flight path that traverses the shortest distance through the fence (a worst case) will determine the maximum allowable time between successive looks. The aircraft is assumed to follow a great circle route and does not perform evasive maneuvers. Flight paths in an easterly or westerly direction from the USSR will most likely require an in-flight refueling, however, this scenario does not impact the waveform and clutter design requirements. Additional radar fences could be erected along the satellites orbital path without increasing the power-aperture requirements. Figure II-2 shows the geometry of the problem and defines some terms for the analysis that follows. The minimum angular extent of the fence is θ. The aircraft flight path in the plane of Fig. II-2 represents a worst case condition since all other flight paths through the fence are longer, permitting longer search times.

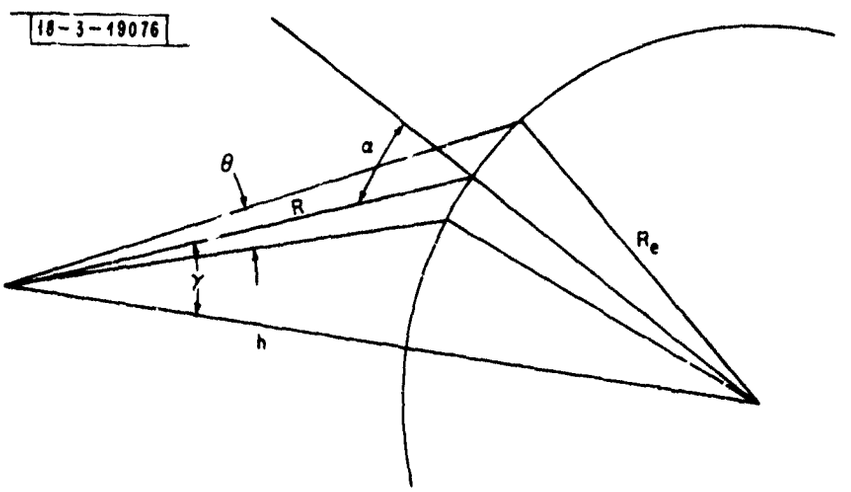


Fig. II-2. Geometry defining minimum distance through fence.

The altitude of the satellite is much greater than the altitude of the aircraft. The range from the satellite to the aircraft can be approximated by the range from the satellite to the earth.

The minimum distance through the fence is approximately:

$$\dot{x} = \frac{R\theta}{\cos \alpha}$$

An aircraft traveling at a velocity v_t will pass through the fence in a time given by

$$t = \frac{x}{v_t} \doteq \frac{R\theta}{v_t \cos \alpha}$$

If we require two independent looks at the aircraft while it is in the fence, the search period becomes

$$t_s = \frac{R\theta}{2v_t \cos \alpha}$$

The maximum allowable search time to insure at least two looks at the aircraft is plotted in Fig. II-3 vs the distance the aircraft must travel through the fence. The velocity of the aircraft is a parameter. As the distance through the fence increases, the allowable search time increases proportionally. If, for example,

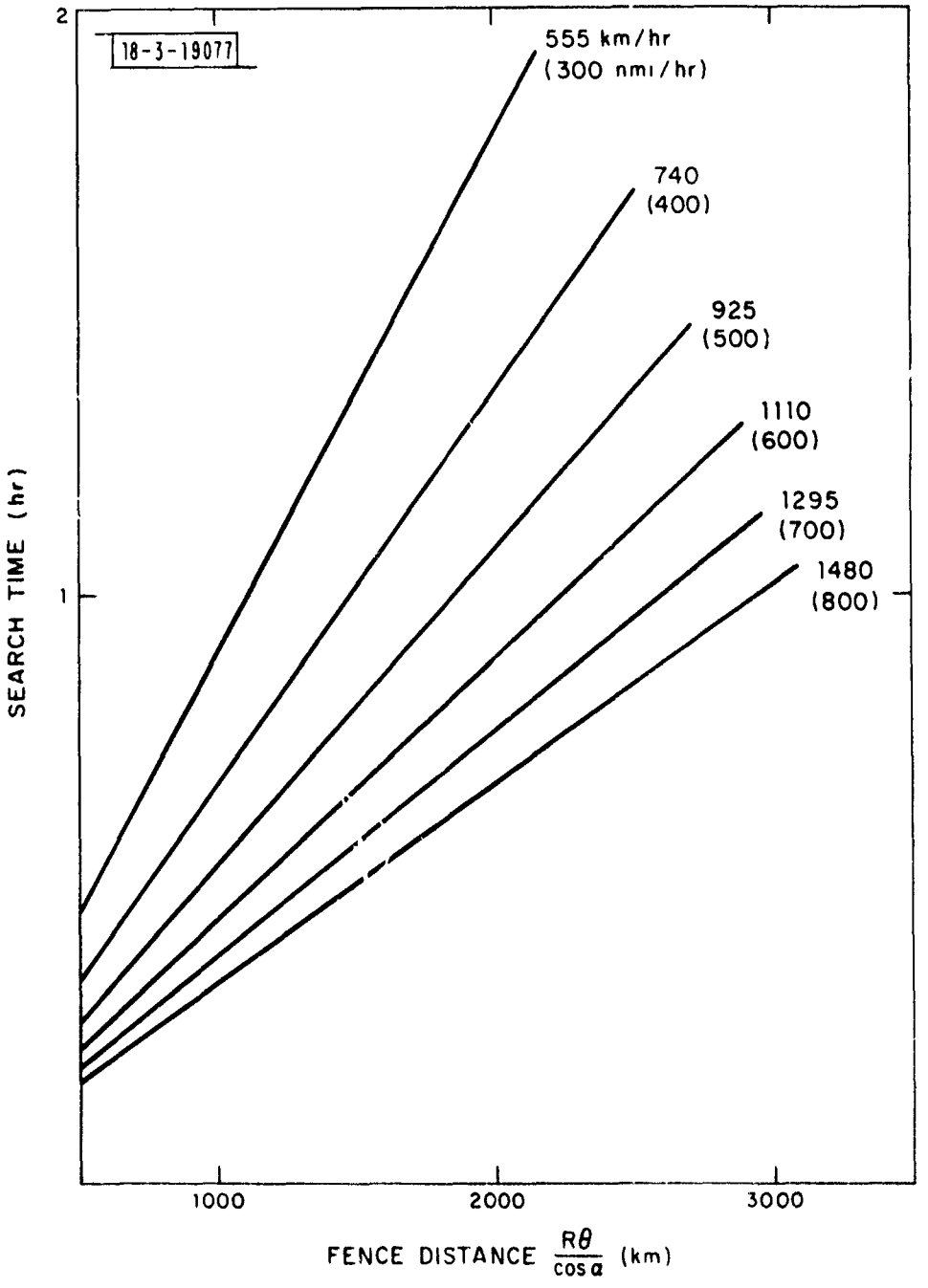


Fig. II-3. Search time requirements.

a 925 km (500 nautical mile) fence were used and the average aircraft velocity were 925 km/hour, the fence would have to be searched every half hour.

2.4 Potential Advantages of Bistatic Systems

The principal potential advantages of a bistatic radar for aircraft detection are aircraft cross-section enhancement and ground clutter cross-section density diminution. The combination of these two potential effects is to increase the signal-to-clutter ratio, S/C, and thereby simplify the detection process. The existence and extent of these potential advantages must ultimately be determined by measurements.

Bistatic radar cross-sections of simple shapes have been calculated in the literature.[1] The forward scatter cross-section of simple shapes has been shown to be many times the backscatter cross-section when the wavelength is small compared to the target dimensions. However, it is difficult to predict whether a complicated target, such as an aircraft, will exhibit this large cross-section enhancement.

Bistatic clutter measurements have been made[2] for various terrain conditions but only over limited bistatic geometries. Additional data are needed before definitive conclusions about potential advantages of bistatic clutter cross-section can be made.

III. RADAR PARAMETER ESTIMATES

In this section, the size of a radar to perform search from a satellite-borne platform is estimated as a function of search rate. Several example designs are presented and some comments about system realizability are made. Included are some remarks about communications and control. The results of the power-aperture product estimates are parameterized over a large range interval to include satellite orbits up to geosynchronous altitude. At geosynchronous altitude, the ground clutter will appear at zero Doppler with a small spread. In general, the target will present a Doppler different from the clutter Doppler. At lower satellite altitudes, the clutter Doppler will be offset from zero frequency and will be a function of the angle the radar line of sight makes with the velocity vector. This tends to complicate Doppler filtering. Furthermore, a geostationary satellite radar system allows a fence to be placed at any desired location within the field of view and its location can be changed at any time. It provides for continuous viewing of a specific area and allows for continuous tracking of detected targets for extended periods of time. In addition it allows for repeated looking at specific areas such as most likely flight paths. The main disadvantage of a geosynchronous altitude system is that a very large power-aperture product is required, as will be seen in this section. A lower altitude system requires a lower power-aperture product; however, more satellites are required to provide

the desired coverage.

3.1 Search Power-Aperture Product

A useful form of the radar equation for sizing a search radar system operating in a bistatic mode is given by

$$PA = \frac{4\pi\, k\, T\, L}{\sigma_b} \left(\frac{S}{N}\right) R_t^2\, R_r^2\, \dot{\Omega} \qquad (1)$$

where

$\dot{\Omega}$ = solid angle search rate

R_r = range from target to receiver

R_t = range from target to transmitter

$\frac{S}{N}$ = signal to noise ratio

L = system losses

T = system temperature

k = Boltzmann's constant

σ_b = bistatic target cross-section

A = aperture area

P = average radiated power

The equation can be put in a more useful form if we relate the solid angle search rate to the ground coverage rate. The intersection of the beam with the surface of the earth determines the

ground coverage per beam position. For a narrow circular beam, this area is given by

$$\text{Area} \approx \frac{R^2 \theta^2}{\cos \alpha} \tag{2}$$

where

α = angle the radar LOS makes with the target local vertical

θ^2 = solid angle subtended by the beam (omitting a factor $\approx \pi/4$)

R = range to target

For a bistatic system the area illuminated is determined by the smaller of the transmitter or receiver illumination. If the transmitter and receiver are at the same altitude, hence at nearly equal ranges in most cases, the smaller beamwidth will determine the illuminated area. Differentiating both sides of equation (2) and assuming the range and radar angle, α , to remain essentially constant over the search volume, we obtain

$$\frac{d\ \text{Area}}{dt} \approx \frac{R^2}{\cos \alpha} \cdot \frac{d(\theta^2)}{dt} = \frac{R^2}{\cos \alpha}\ \dot{\Omega} \tag{3}$$

Substituting equation (3) into equation (1) we have

$$PA \approx \frac{4\pi\ k\ TL}{\sigma_b} \left(\frac{S}{N}\right) R^2 \left(\frac{d\ Area}{dt}\right) \cos\ \alpha \qquad (4)$$

An aircraft attack against CONUS would most likely use routes across the northern portion of Canada. A small portion of these routes might occur over the broad ocean areas; however, for this analysis only flights over Northern Canada are considered. The angle the radar line of sight (from geostationary altitude) makes with the target local vertical varies between 64 and 82 degrees for a 100 n.mi wide fence centered about 65° N latitude. Therefore, an average value for α of 70 degrees will be used. The ground coverage search rate ($\frac{d\ Area}{dt}$) is plotted in Fig. III-1 as a function of the power aperture product given by equation (4) with range a parameter.

The strong dependence of the power-aperture product on search rate is demonstrated in Fig. III-1 and illustrates the need to minimize the search rate to maintain system realizability. The ground search rate is given by:

$$\frac{d\ Area}{dt} = \frac{T \times W}{t_s}$$

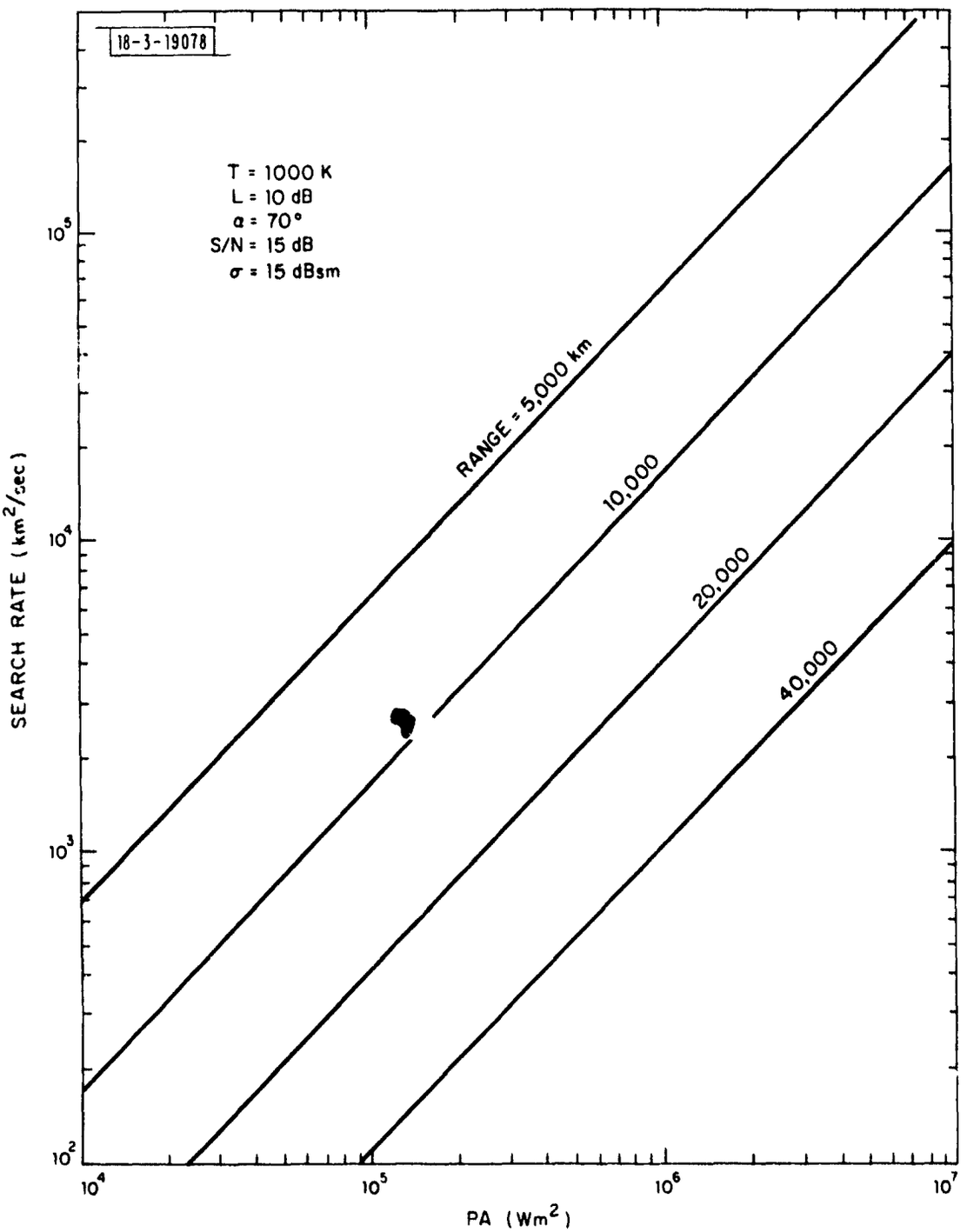


Fig. III-1. Search rate vs. power aperture product.

where

T = thickness of fence

W = width of fence

t_s = time to search entire fence

$$t_s = \frac{T}{n\, v_t}$$

where

n = number of opportunities provided to observe a target (uniform search assumed)

v_t = target velocity

$$\frac{d\ \text{Area}}{dt} = n\, v_t\, W$$

Note that the ground search rate is independent of fence thickness. It depends only on the number of independent opportunities to view the target (assuming a uniform search), the aircraft velocity and the width of fence. For this analysis, we will assume an average aircraft velocity of 500 n. mi./hour (0.26 km/s). If we require at least two opportunities to view the aircraft while it is in the fence and we assume that the fence will be covered once per hour, the fence must be 1000 n. mi. (1800 km) thick. The width of the fence should be such that it intercepts the major portion of possible direct flight paths from the Soviet Union to the United States. This implies a fence approximately 3000 n. mi. (5500 km)

wide. The ground search rate for this set of conditions is 3×10^6 sq. n. mi./hour or 2.85×10^3 sq. km/s. Note that wavelength does not appear explicitly in equation (4) so that this result applies at any wavelength provided the system temperature, losses and target cross-section used are the same at these wavelengths. The wavelength dependence is implicit in the expression for aperture.

$$A \approx \left(\frac{\lambda}{\theta}\right)^2 \tag{5}$$

The wavelength dependence of the power and/or aperture can be plotted once an operating altitude (range) or a beamwidth is chosen. Figures III-2 and III-3 are example plots showing the power and aperture dependence on wavelength at nominal ranges of 5000 and 40000 km respectively. Antenna beamwidth is a parameter. The power-aperture product increases by 18 dB when the range is increased from 5000 km to geosynchronous altitude ranges.

3.2 Track Power-Aperture Product

The requirements for a tracking radar system are described by the following form of the radar equation

$$P_t A^2 = \frac{4\pi\, k\, T\, L\, B}{\sigma_b} \left(\frac{S}{N}\right) R_t^2\, R_r^2\, \lambda^2 \tag{6}$$

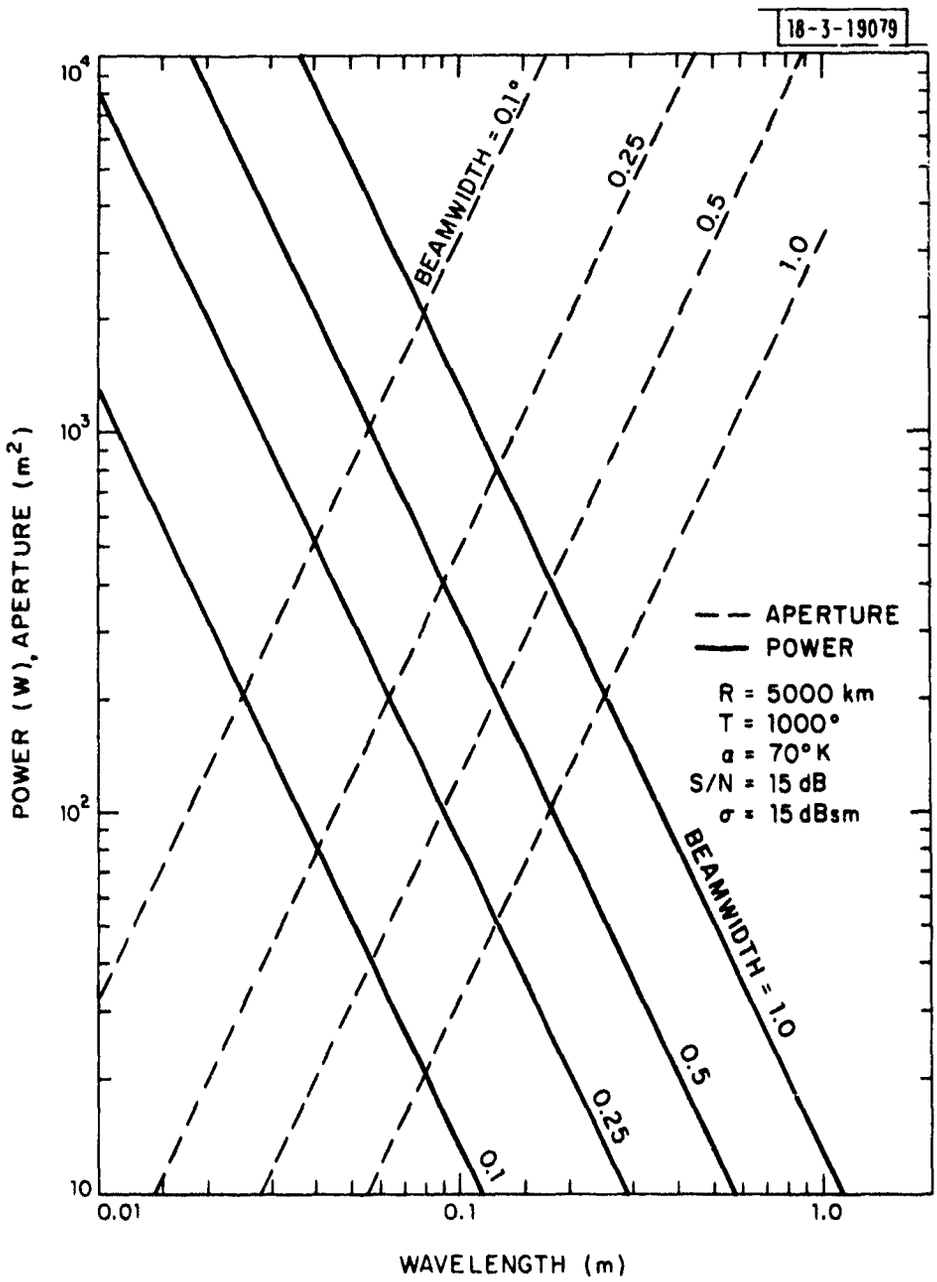


Fig. III-2. Power and aperture vs. wavelength for 500 km range.

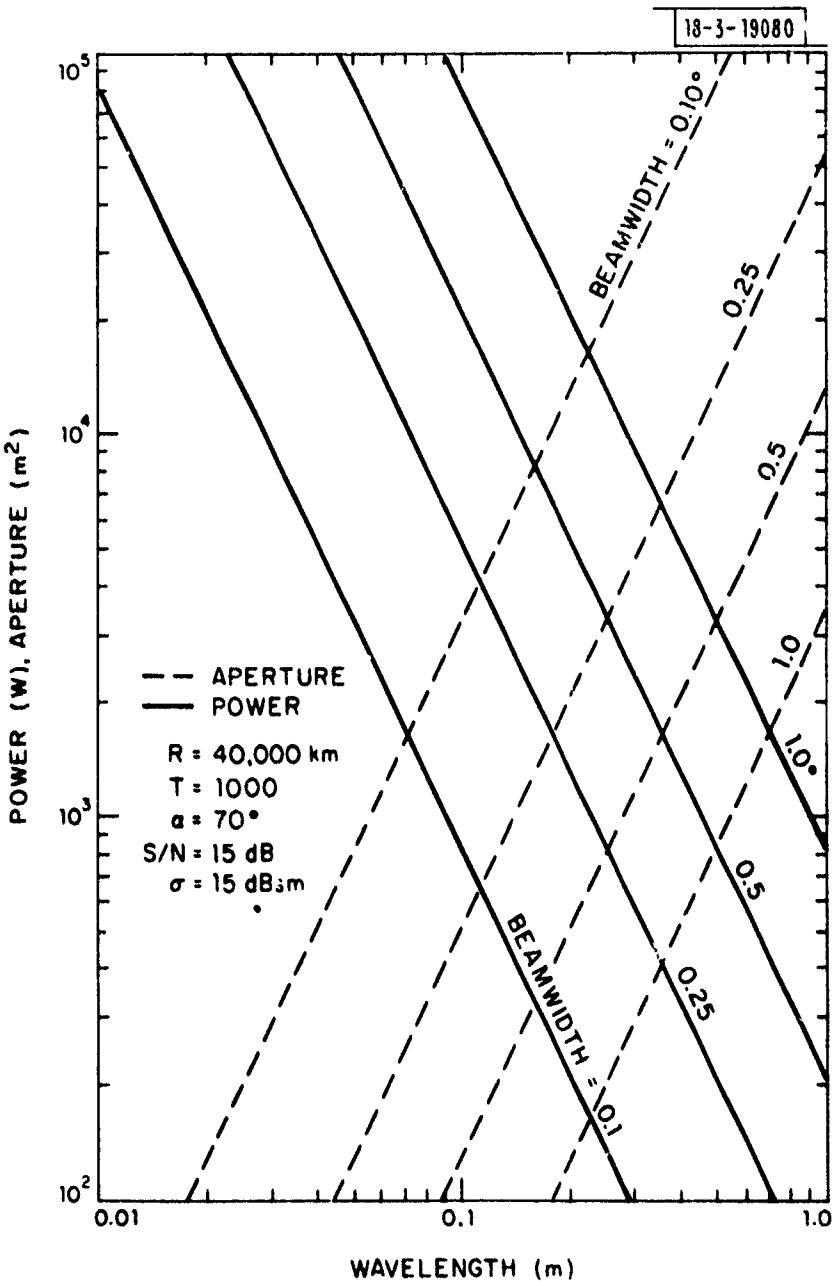


Fig. III-3. Power-aperture vs. wavelength for 40,000 km range.

For

$$B = \frac{1}{\tau}$$

and

$$P_{av} = P_t \tau \, (PRF)$$

let PRF = BRF (Burst repetition frequency) equation (6) becomes

$$PA^2 = \frac{4\pi \, k \, T \, L}{\sigma_b} \left(\frac{S}{N}\right) (BRF) \, R_t^2 \, R_r^2 \, \lambda^2 \qquad (7)$$

A pulse burst waveform is needed for clutter filtering and is discussed in Section VI. The track rate is 1 burst per dwell. If the bistatic transmitter and receiver are in satellites at the same altitude, the ranges from the transmitter to the target and the receiver to the target will be nearly equal in most cases. For this analysis, we set $R_t = R_r = R$. The aperture and wavelength are related to the beamwidth by equation (5). Substituting this relationship into equation (7) and rearranging terms we have

$$\frac{PA}{\theta^2} = \frac{4\pi \, k \, T \, L}{\sigma_b} \left(\frac{S}{N}\right) R^4 \, (BRF) \qquad (8)$$

Figure III-4 plots the burst repetition frequency, BRF, as a function of the tracking performance parameter PA/θ^2 with range a parameter.

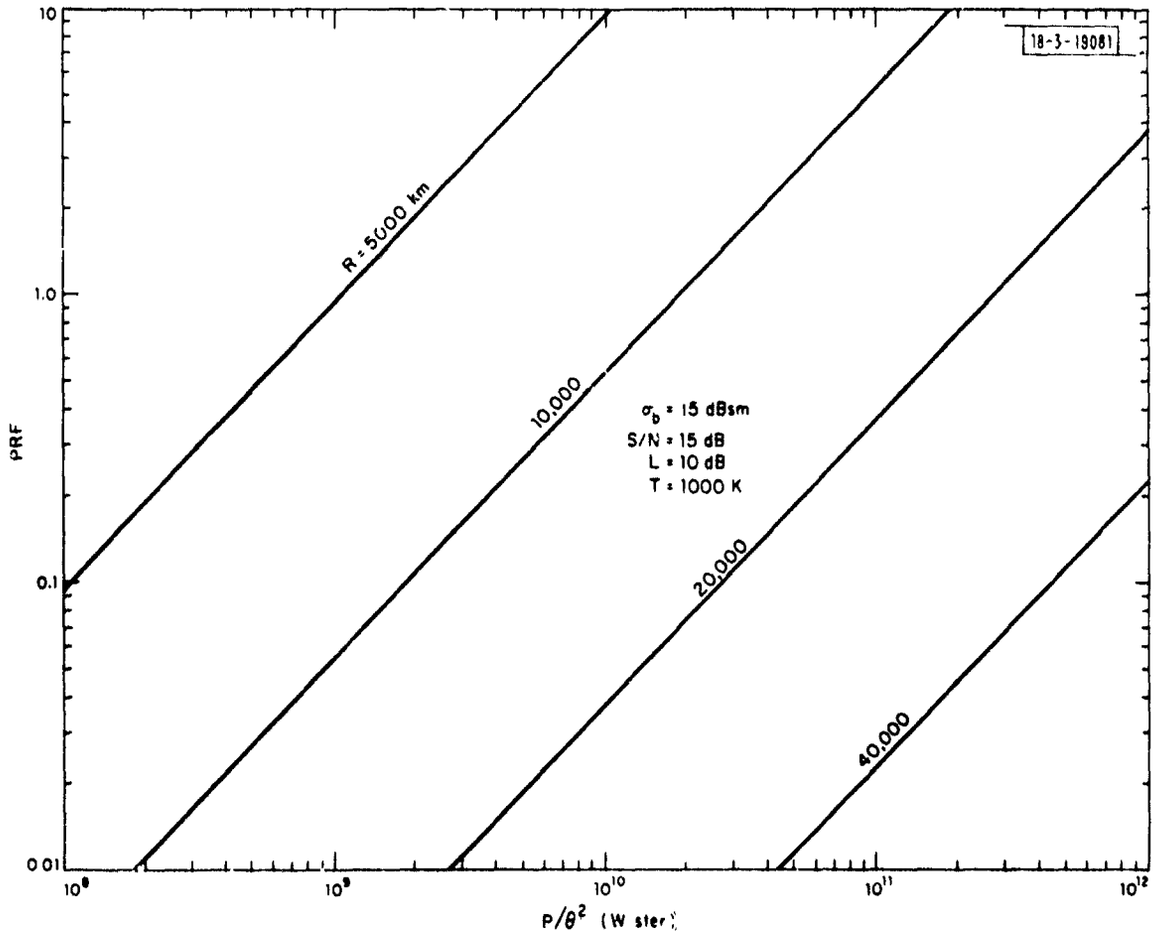


Fig. III-4. PRF vs. power-inverse beamwidth squared product.

The track function requirement is in addition to the primary surveillance requirement. The additional system capability to perform the track function can be easily determined using Fig. III-4 and the search radar beamwidth. The revisit time, or 1/BRF, is determined by the target velocity, antenna beamwidth and range to the target. The most stringent requirement is when the target is allowed to maneuver between pulse bursts. In this case, the BRF becomes:

$$BRF \geq \frac{v_t}{R\theta}$$

If the target is restricted to fly a great circle route, the BRF track requirement becomes a function of the tracking algorithm and the measurement accuracy. In general, this requirement will not be as severe as that given for the maneuvering target example above.

As an example, consider the radar system at geosynchronous altitude. The target is assumed to be moving at 500 n. mi./hour and the beamwidth is 0.1 degree. The BRF becomes 3.68×10^{-3} sec^{-1}. If we allow the target to move a maximum of one-half beamwidth between successive track pulses, the average power becomes 30.4 watts per target. An operating wavelength of 0.1 meter was assumed. This represents a small increase in average power; however, if many targets (>100) must be tracked, a sizeable increase in system

performance will be necessary.

3.3 System Realizability

The power-aperture curves presented in the previous sections form the basis for determining the tradeoff between power, aperture and range. The other parameters in the search radar equation are fairly well defined constants. The parameter least defined is the bistatic radar cross-section. It remains to be better defined by measurements. In this analysis we have assumed the target cross-section is 15 dBsm and remains constant with changes in aspect angle and wavelength.

A satellite-borne radar system viewing targets against a background of the earth will have to detect targets imbedded in clutter. The amount of clutter competing with the target is determined by the resolution cell size in range and cross-range (Doppler) and the reflectivity (σ_o) of the clutter. Measurements have been made[3] of isolated samples of ground clutter at L-band and X-band. These data are for small bistatic angles and are mainly in the plane containing the transmitter and local vertical. Wide bistatic angle data out of the plane described above does not exist so far as we have been able to determine. The existing data suggest that there is a large variation in the bistatic clutter cross-section and that there is little systematic difference between it and monostatic clutter cross-section. A satellite-borne bistatic system will be viewing large areas which are composites of various

types of surfaces. It is difficult to predict the behaviour of the bistatic clutter return as the satellite passes over varying terrain such as cities, smooth fields, mountains, ice, snow, etc.

The available data suggest that the resolution cell size should be made as small as practicable. The techniques for achieving resolution in the range direction are well known. Bistatic range resolution on the order of the maximum dimensions of the target ($30m < \delta < 100m$) is well within the state of the art. The resolution in the cross-range direction is obtained by making the antenna beamwidth small. This implies a large aperture which may not be easily achieved on a spaceborne platform. The largest antenna known to us to be deployed aboard a space platform is a 10 meter diameter parabolic dish structure. Techniques which are tolerant of mechanical errors and still capable of maintaining a reasonable antenna beamwidth (gain) will have to be exploited for space-borne applications.[4]

The intersection of the antenna beam and the surface of the earth will be approximately an ellipse with the major axis oriented along the range direction and the minor axis normal to the range direction. The cross-range dimension vs range to the satellite is plotted in Fig. III-5 with antenna beamwidth a parameter. At geosynchronous altitudes (range = 40,000 km), an antenna beamwidth of 0.1 degree gives a cross-range dimension of approximately 70 km.

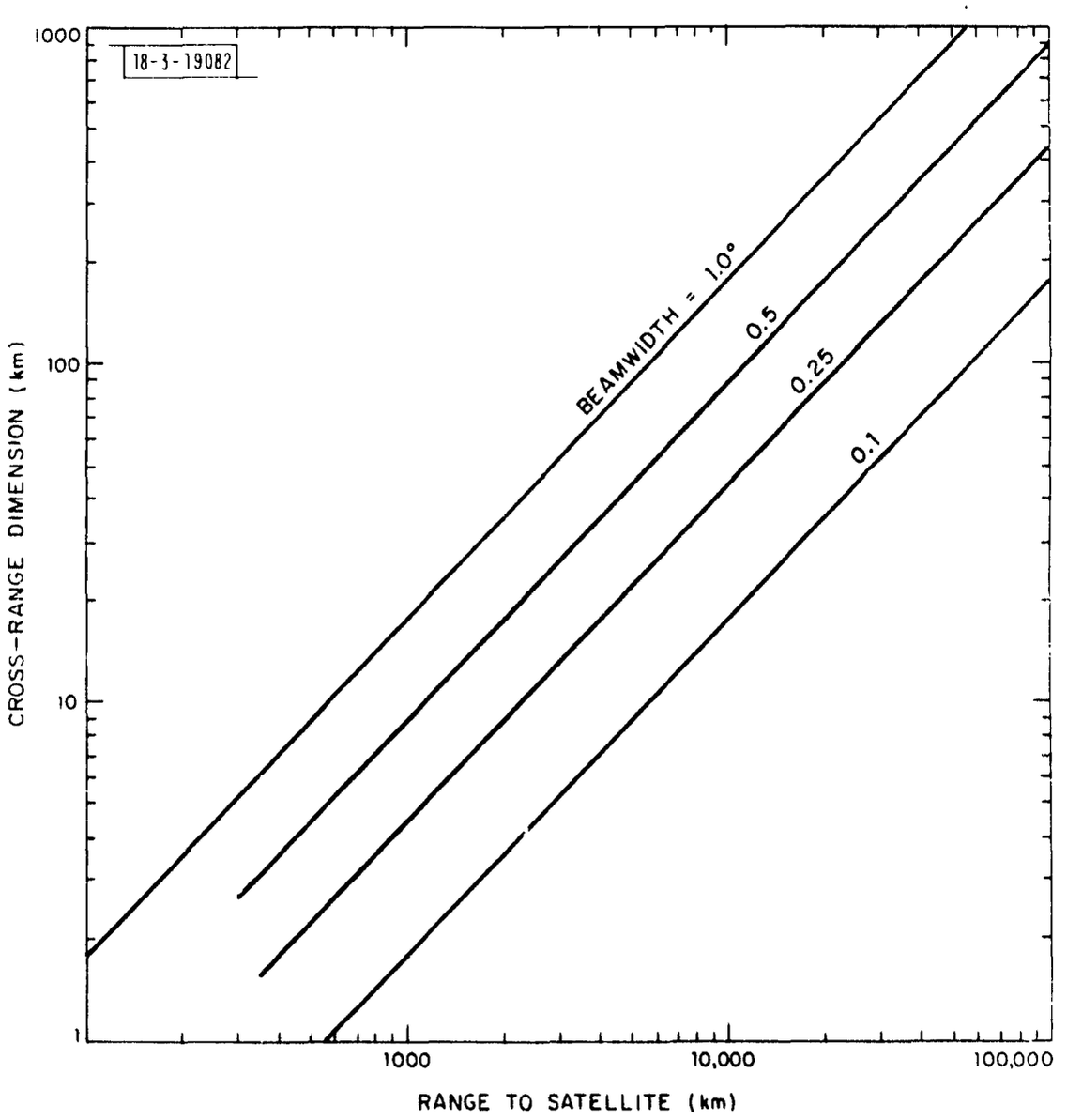


Fig. III-5. Cross range vs. range to satellite.

The parameters used to generate the power-aperture vs wavelength curves of the previous section will be used in a sample design for a bistatic radar system at geosynchronous altitude. The power-aperture product to search a 1000 x 3000 n. mi. ground area once per hour is

$$PA = 2.7 \times 10^6 \text{ w m}^2$$

For this example, let us assume the following additional parameters.

σ_o = clutter reflectivity = -10 dBsm/m^2

θ = beamwidth = 0.1 degree

R = range to target = 40,000 km

δ_r = range resolution = 100 m

$\frac{S}{C}$ = required target-to-clutter ratio after filtering = +15 dB

The bistatic clutter cross-section in a range cell can be approximated, for small bistatic angles, by

$$\sigma_c \sim \sigma_o A = \sigma_o (R\theta)(\delta r)$$

$$\sigma_c \sim 60 \text{ dBsm}$$

To achieve a target to clutter ratio of +15 dB on a target cross section of 15 dBsm, a clutter filter with a -60 dB sidelobe response is required. Other examples are discussed in Section V.

Let us arbitrarily choose an operating frequency of S-band (wavelength = 0.1 m). The aperture to generate a 0.1 degree circular beamwidth becomes

$$A = \frac{\lambda^2}{\theta^2} = 3282 \text{ m}^2$$

The required average power is

$$P \approx 825 \text{ watts}$$

The system parameters are summarized in Table III-1. The parameters of this sample system are ambitious. The generation of approximately 1 kw average power for an extended period of time in space, deployment of a large aperture in space and advanced clutter filtering techniques would need to be developed. Some filter designs are discussed in Section VI.

TABLE III-1

An Example

Radar System Parameters

Average Power	825 watts
Wavelength	0.1 meter
Beam Width	0.1 degree
Antenna Diameter	60 m
Range Resolution	100 m
System Temperature	1000^{o} K
Losses (Transmit & Receive)	10 dB
Target cross-section	15 dBm^2
Range	40,000 km
Search Time	1 hour
Search Area	1.03×10^{13} m^2
Clutter Filter Response	≥60 dB clutter rejection
S/C required after filtering	+ 15 dB
S/N	+ 15 dB

IV. REPRESENTATIVE SATELLITE ORBITS

4.1 General Categories

Satellite orbits for bistatic surveillance can be grouped into several categories which relate to various system design objectives. Low altitude satellites allow shorter ranges and therefore reduced power-aperture product but at the expense of small coverage per satellite. Geostationary satellites are always in position to scan a fence but their high altitude results in large power-aperture requirements. Intermediate altitude satellites may provide a compromise between coverage and power-aperture requirements. Satellites whose periods are commensurate with that of the earth will have repetitive ground traces and coverage. This characteristic is desirable to minimize the number of satellites, but not essential. Additional objectives are to select bistatic geometries which: (1) ease the clutter rejection problem by advantageous placement of the clutter relative to targets in the range-Doppler (R-$\dot{R}$) plane and (2) exploit any potential target bistatic cross-section enhancement and/or clutter diminution.

4.2 Virtual Radar Location

The location of a satellite borne bistatic radar can be characterized by the sub-satellite point of a virtual satellite-borne monostatic radar on the bisector of the lines-of-sight to an arbitrarily located target. The range of the virtual radar

from the target is selected so that, for all other parameters of the bistatic and virtual monostatic radars the same, the S/N ratio is the same for both radars. This range is the geometric mean of the receiver-target and transmitter-target ranges of the bistatic radar. The virtual radar sub-satellite point is illustrated in Fig. IV-1.

A second characterization of the virtual radar location is the sequence of points on the earth's surface at which the clutter can be separated from an aircraft by range gating. The local vertical at these points lies along the bistatic range vector and their locus is generated by the motion of the satellites and the earth. Figure IV-2, illustrates the geometry for one of these points. For a satellite-borne monostatic radar these points are the sub-satellite points.

Examples of coverage from bistatic radars are given below for representative orbits. The R-$\dot{R}$ characteristics of clutter and aircraft are discussed in Section V.

4.3 Examples of Coverage

The virtual radar location as defined above provides a convenient means of indicating the viewing aspects of various points on the earth's surface. Plots of these locations for four representative bistatic configurations are presented in Figs. IV-3 to IV-9.

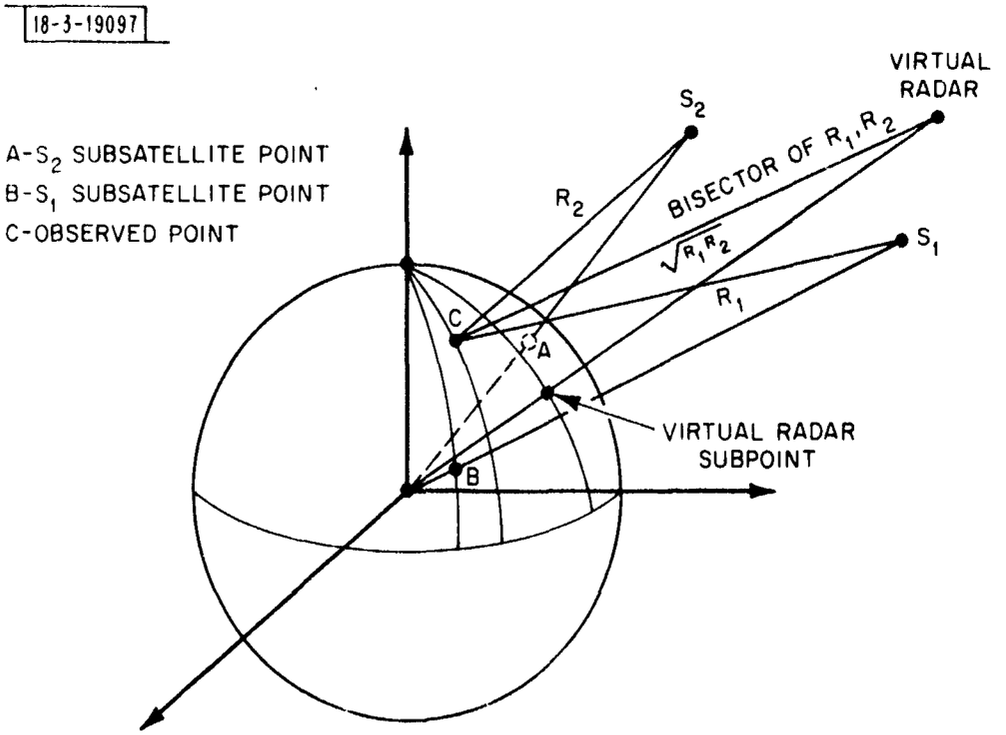


Fig. IV-1. Geometry illustrating virtual radar sub-point for a bistatic radar viewing a general point on the earth.

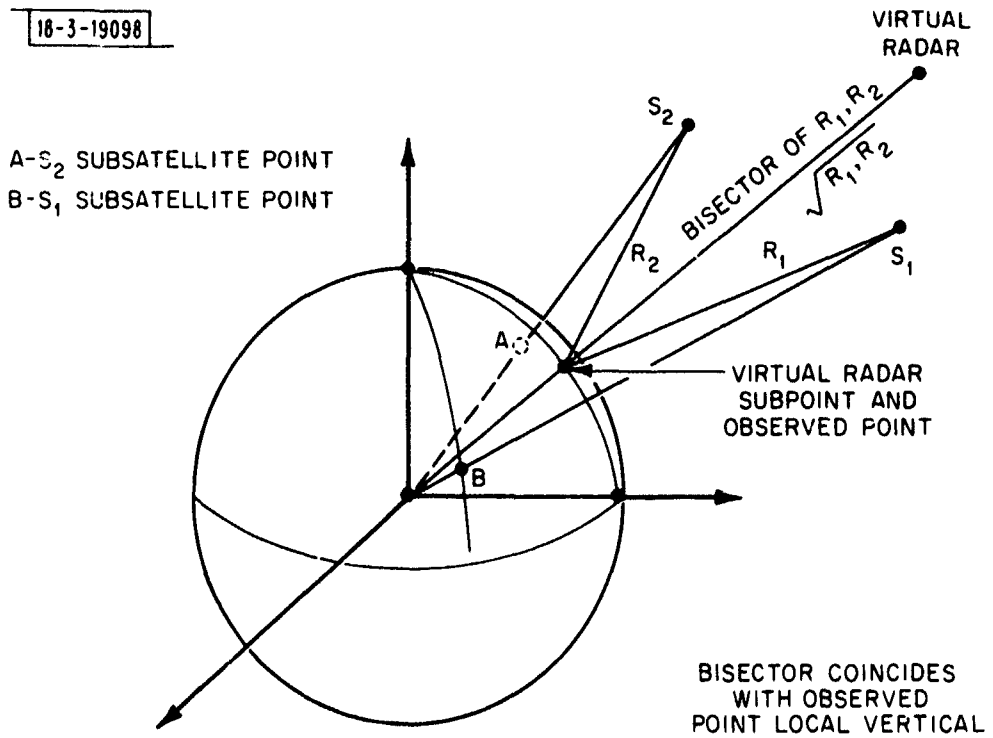


Fig. IV-2. Geometry illustrating coincidence of virtual radar sub-point and observed point.

Figure IV-3 shows the sequence of virtual radar locations of a bistatic radar viewing five points at 60° N latitude and within the surveillance fence. The receiver and transmitter of the bistatic radar are each on a 12 hour period satellite whose elements are included in Fig. IV-3. Note that the nodes are 180° apart. The periods and inclinations of these satellites are equal and are adjusted so that their angular rates at apogee match the angular rate of the Earth. The periods are also made commensurate with that of the Earth. Because of this matching of angular rates the virtual radar location does not move greatly during the time the viewed points are visible to the satellites. Also, since the satellites are on opposite sides of the North Pole, the bistatic range vector to the pole lies along the Earth's axis and consequently the pole is visible (about 9 hours), that is the virtual radar is stationary over the pole.

Figure IV-4 similarly shows the virtual radar locations for two 6 hr. period satellites in the same plane, nodes 180° apart, moving in opposite directions and with apogees at 105° E longitude. The virtual locations tend to be at a constant latitude (the orbit plane inclination) during much of the time the viewed points are visible. Figure IV-5, for the same pair of satellites, shows the sequence of locations for which clutter can be range-gated. This sequence is nearly at constant latitude and covers about half of the fence width in 4.4 hours. This is a consequence of the virtual

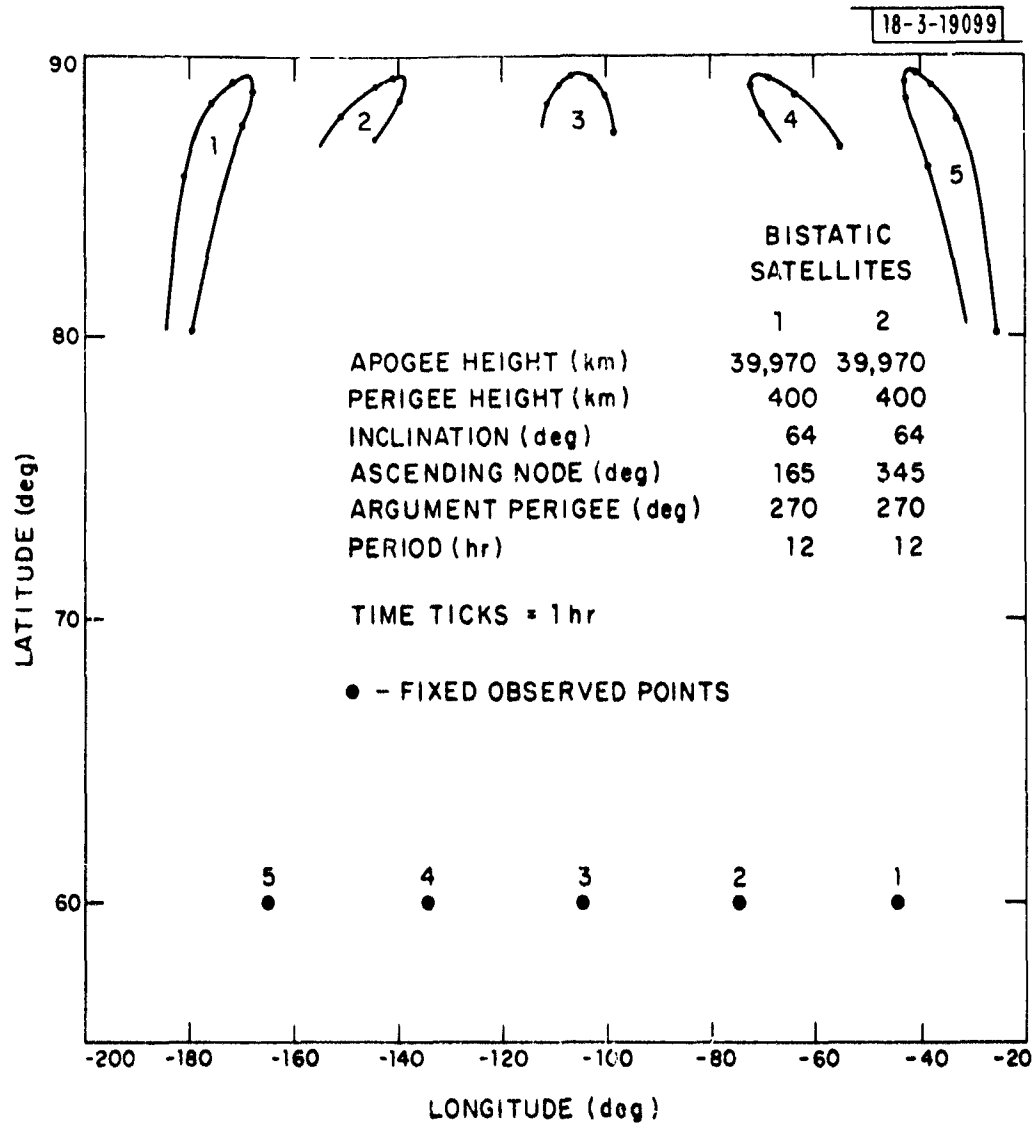


Fig. IV-3. Ground traces of virtual satellite observing various points: example 1.

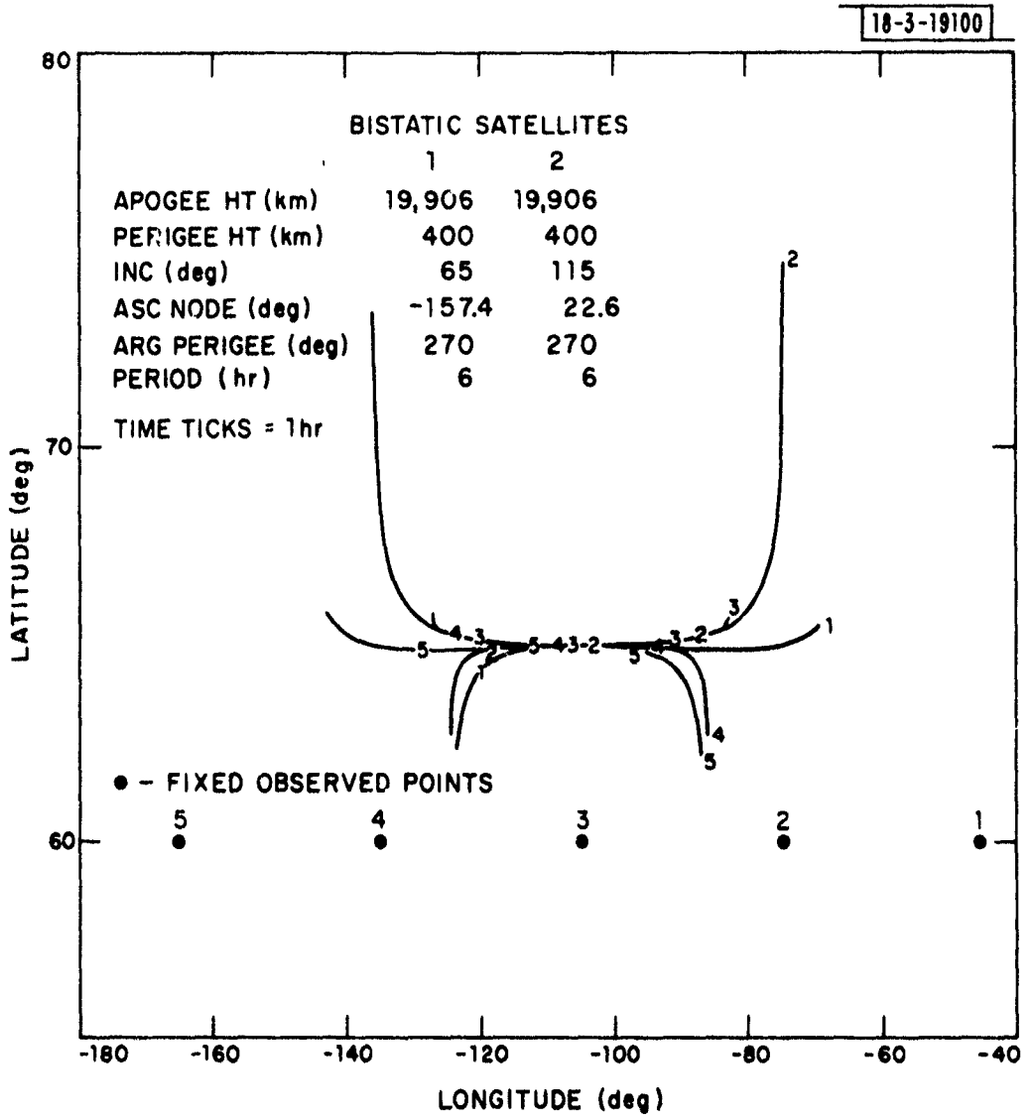


Fig. IV-4. Ground traces of virtual satellite observing various points: example 2.

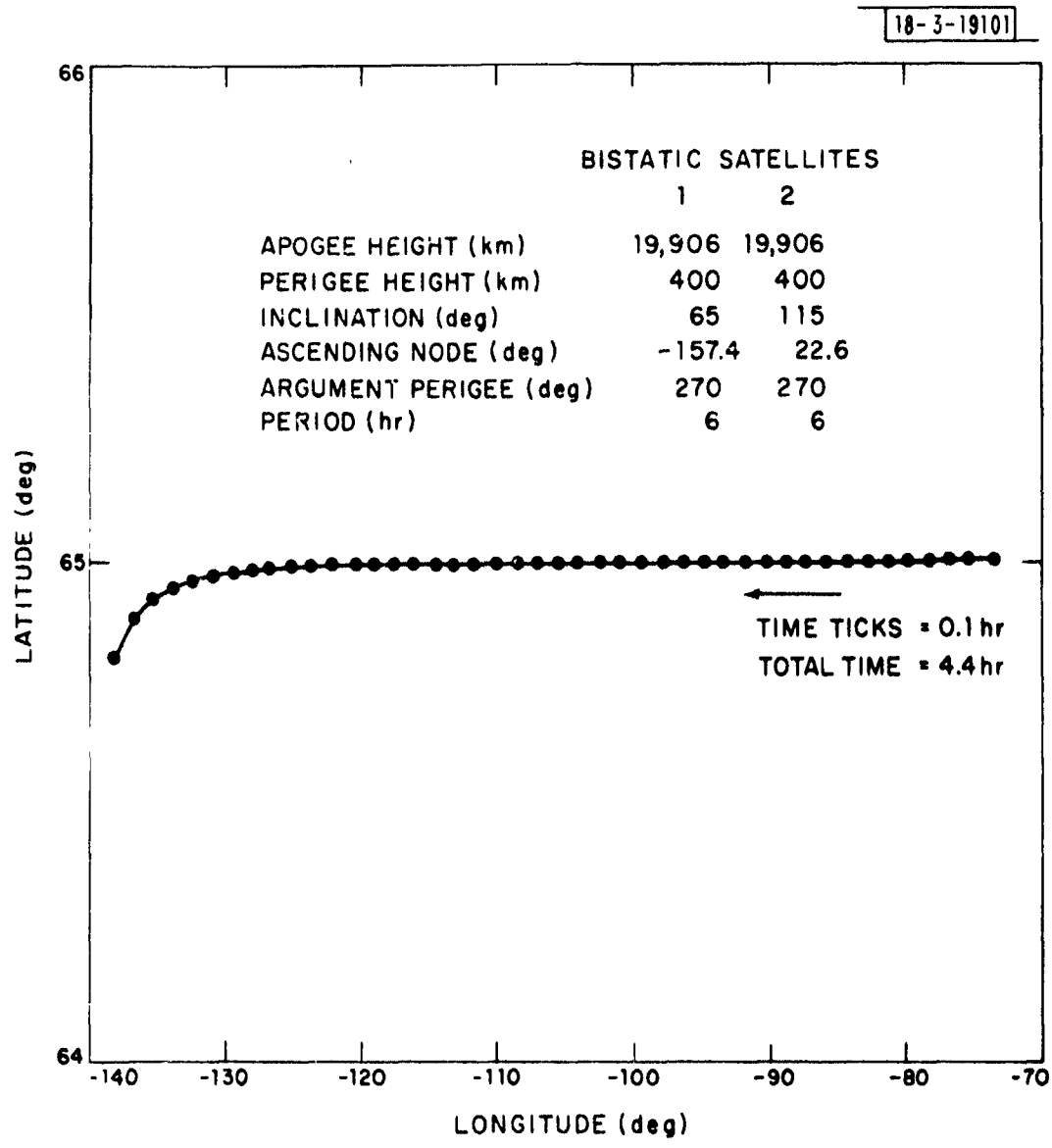


Fig. IV-5. Sequence of points for which Clutter can be Range Gated.

radar being nearly fixed in inertial space for this example. Although the location of this sequence is within the fence, many satellites would be required to provide similar virtual radar traces to fill out the complete width and length of the fence. It is unlikely that the virtual radar location of either Fig. IV-4 or Fig. IV-5 can be closely approximated by a monostatic radar, although operationally equivalent performance may be possible by altering the shape of the fence. The bistatic angle for this system will vary with time from 0^{o} to near 180^{o}.

Figures IV-6 and IV-7 show virtual radar locations for a geostationary satellite at -105^{o} E longitude and a 6 hr. period polar satellite that has its apogee over the pole. The traces of Fig. IV-6 essentially overlap so that the virtual radars for all of the five points in the fence have comparable "orbits". The trace of Fig. IV-7 indicating points where clutter may be range gated is mostly at low latitudes and hence not useful as a fence.

Figures IV-8 and IV-9 are for a pair of 6 hr. period satellites with 65^{o} inclination but with nodes 90^{o} apart. These traces are similar to those of Figs. IV-6 and IV-7 but have greater extent in both latitude and longitude. The trace of Fig. IV-9 is suggestive of a fence covering East and West approaches to the US as well as from the North.

The virtual radar locations for low-altitude co-orbital satellites lie on a narrow strip above the ground trace of the

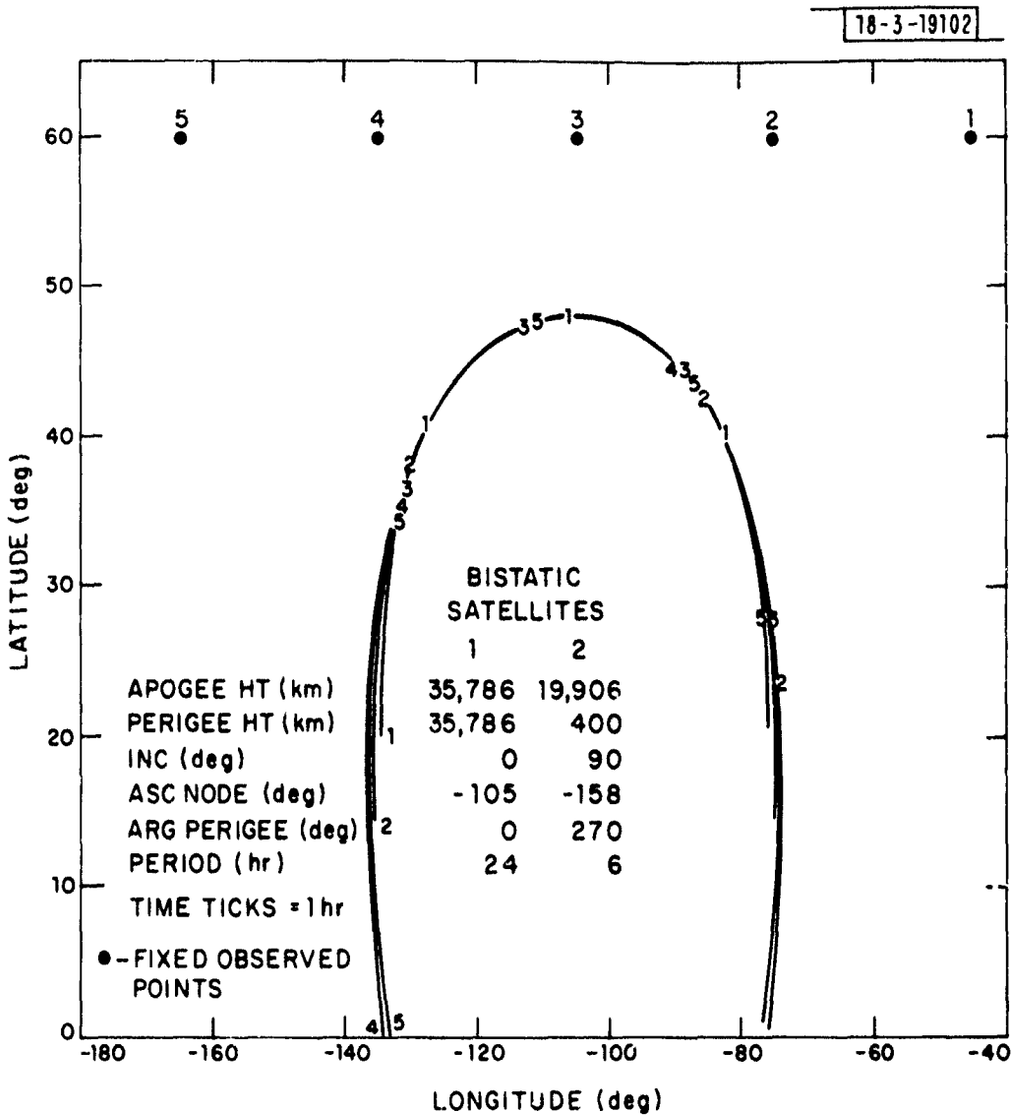


Fig. IV-6. Ground traces of a fictitious satellites with a monostatic radar equivalent to a bistatic radar observing various points.

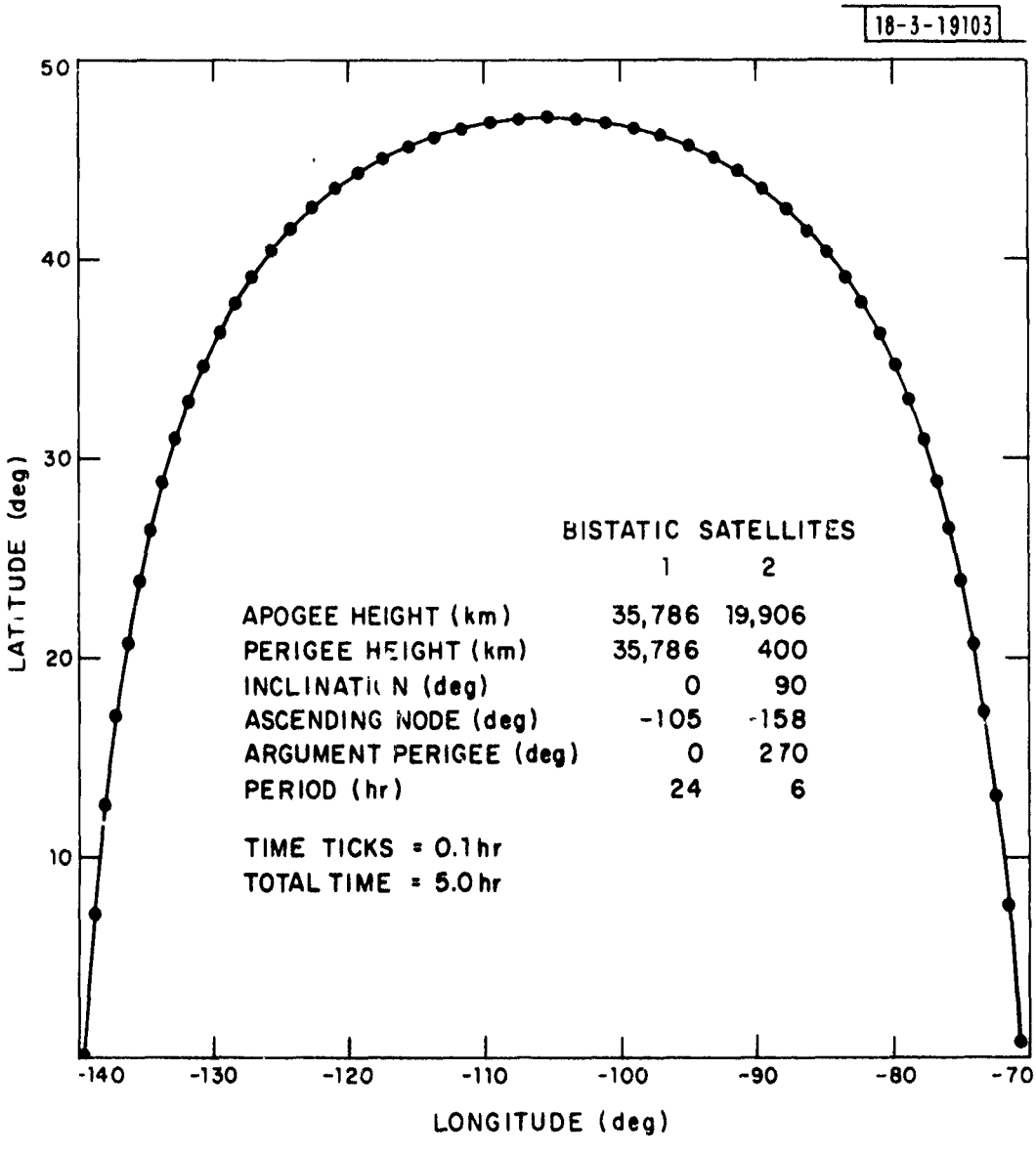


Fig. IV-7. Sequence of points for which clutter can be range gated.

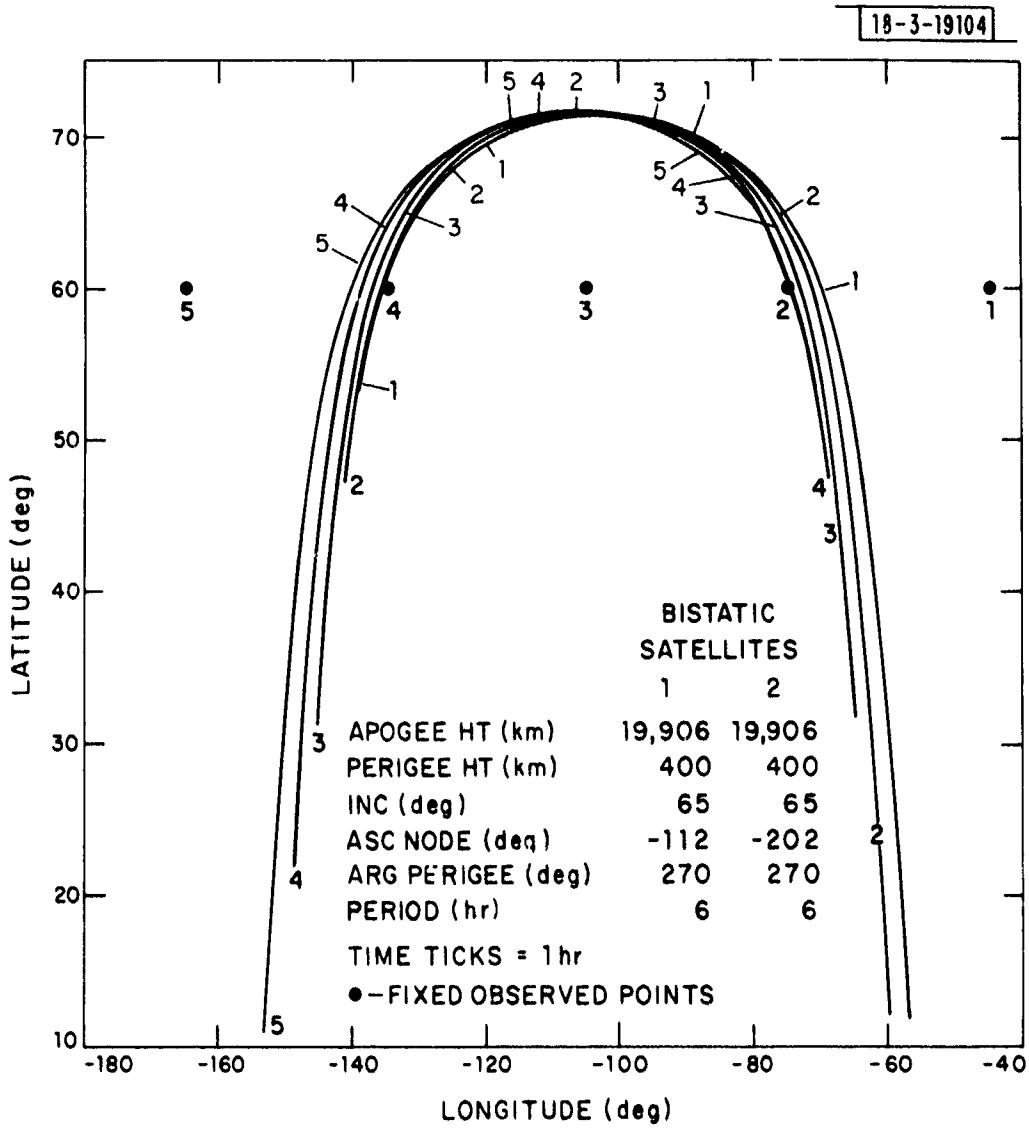


Fig. IV-8. Ground traces of fictitious satellites with a monostatic radar equivalent to a bistatic radar observing various points.

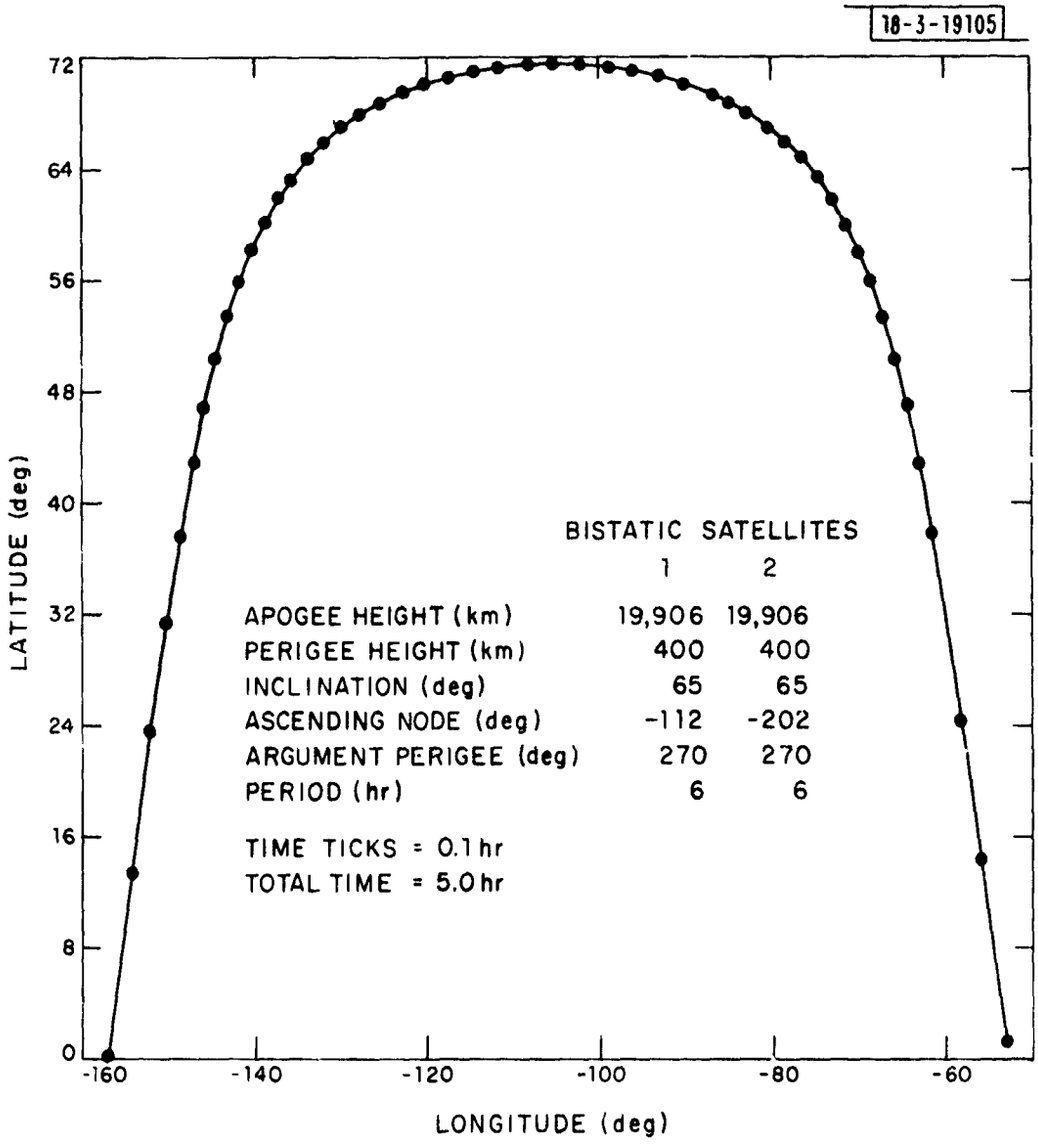


Fig. IV-9. Sequence of points for which clutter can be range gated.

satellites and are not very different from the orbit of a monostatic radar midway between the two satellites (and somewhat higher). As the spacing of the co-orbital satellites is reduced, the virtual radar location converges to the midpoint between the two.

These examples indicate that virtual radar locations can be established at various positions relative to viewed points in the fence and that a high altitude virtual radar can be made to remain "on station" in rather narrow regions during much of the time the points are visible. Lines along which clutter can be range-gated can also be favorably located. The possibility of broadening these lines into a swath for targets at some altitude above the Earth, and for viewing large segments of the line instantaneously should be investigated. A sufficiently wide swath and large instantaneous line segment coverage may permit a reasonable number of satellite radars to scan a fence using range-gating only to eliminate the clutter. (Appendix B addresses this technique for monostatic radars.)

The requirements for beam steering also influence orbit selection. Since precise scanning of large antennas in space does not appear attractive it is expected that the antenna would be stabilized and electronically scanned. To keep the effective aperture large the scan angle from boresight should be kept small (a 60° scan angle from boresight approximately results in a 3 dB aperture loss). The fence scan angle and corresponding aperture

losses can easily be made sufficiently small (less than 0.6 dB) by making the satellite altitudes at least twice the longest dimension of the fence. However, as the satellites move toward the horizon of the fence, the off-boresight angles increase. Consequently, to maintain low aperture loss the satellite altitudes must be increased or the useful viewing time of the fence reduced. An inertially stabilized antenna in a geostationary orbit appears best suited for simple and efficient aperture use.

V. RANGE-DOPPLER MAPS AND WAVEFORM DESIGNS

The satellite-borne bistatic aircraft surveillance radar searches for aircraft against an earth background and therefore must be able to distinguish aircraft from background clutter. The aircraft signal may be within the range and Doppler extent of the clutter or may be separate from it in either range or Doppler or both. Range-Doppler or R-R maps of the clutter and aircraft signals can be made, to show their relationship. The maps can then be used to select suitable clutter rejection techniques. A description of the computation of bistatic range and Doppler for making R-R maps is given in Appendix A.

There is the possibility of range-gating the clutter for certain viewing geometries and aircraft altitudes. A special case of this was discussed in Section IV for the virtual monostatic radar viewing the earth's surface at normal incidence. A discussion of clutter range gating at oblique viewing angles for a monostatic radar is given in Appendix B and illustrates concepts that can be extended to bistatic radars.

The primary technique considered here for separation of aircraft and clutter will be some form of Doppler filtering. The effectiveness of waveforms will depend on the distribution of clutter in Doppler, the location of aircraft in Doppler and signal integration time. The clutter Doppler characteristics are dependent on

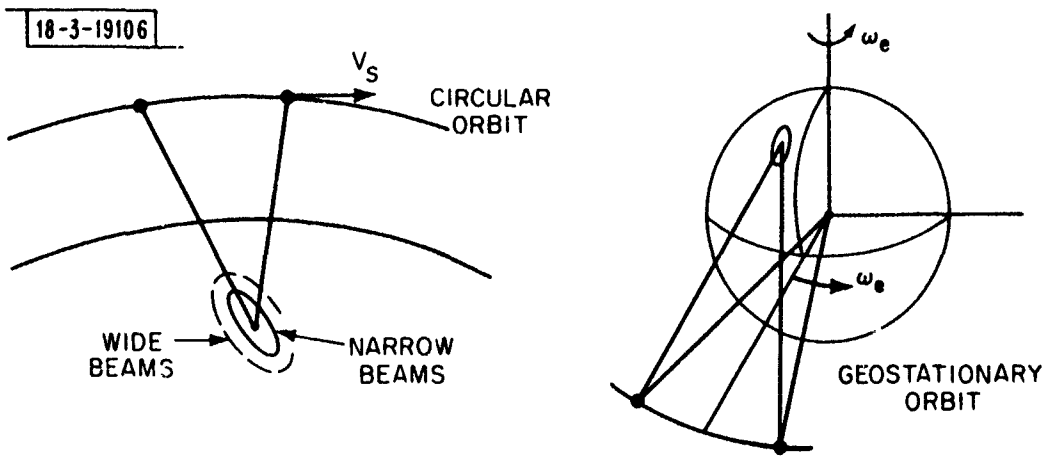
viewing geometry and beam parameters whereas the aircraft Doppler is only geometry dependent.

The waveforms sought must not only provide the needed clutter reduction but must also be consistent with the required search rate for the fence as derived in Section III. That is the illuminated area and integration or dwell time must satisfy the coverage rate requirement

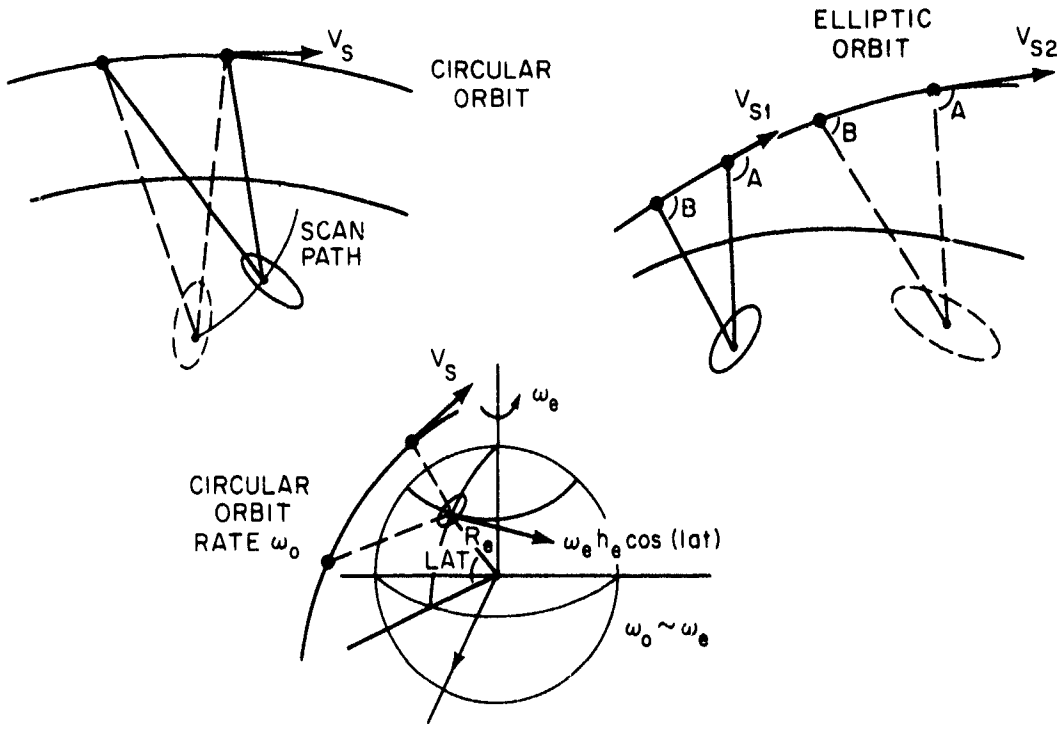
$$\frac{dA}{dt} = \frac{\text{Illuminated area}}{\text{Dwell time}} \geq 2.9\text{x}10^{3}\ \text{km}^2/\text{s}$$

if a single radar is to be able to conduct the search.

Figure V-1 illustrates the geometry for bistatic radars with both fixed and time varying Doppler spread of the clutter. The clutter Doppler distribution of a bistatic radar on low-altitude circular orbits is fixed, dependent only on beam dimensions. As different terrain passes through the field-of-view there will be large changes in clutter cross-section, however, changes in the clutter spectrum are expected to be small compared to the Doppler spread due to satellite motion relative to the earth. The clutter spectrum of a geostationary bistatic radar is fixed, centered at zero Doppler and has zero Doppler spread. Varying Doppler spreads occur when the beams are scanned or when the satellites are on elliptic orbits, and are latitude dependent when the satellites' rates are comparable to that of the earth. Varying clutter



FIXED CLUTTER



VARYING CLUTTER

Fig. V-1. Geometry defining range-doppler clutter spread.

distributions may require a time varying filter to adequately reject the clutter.

5.1 Doppler Resolution Limitations

Three characteristic relations exist between the aircraft and clutter Doppler in a given range cell: 1)aircraft Doppler widely separated from the clutter; 2)aircraft Doppler separated but close to that of the clutter; 3)aircraft Doppler within the clutter Doppler distribution. When the clutter and aircraft are separated in Doppler the Doppler resolution of the waveform and filter need not be great since a highly precise determination of the velocity of the target is not necessary. However, low sidelobes are essential. If the target and clutter are closely spaced in Doppler the waveform and clutter filter must also have sharp skirts. The coherent integration time will limit both the Doppler resolution and filter skirt sharpness.

When the aircraft and clutter Doppler overlap then Doppler resolution can increase the S/C, but only by the ratio of the total clutter Doppler spread to the Doppler spread of the aircraft. For a monostatic radar viewing a bomber with a characteristic dimension of 30 m, the RMS Doppler error due to scintillation is estimated[5] to be

$$\Delta f_s \sim 2.72 \left(\frac{2\pi\bar{\varepsilon}}{\lambda}\right) \frac{\dot{\bar{\eta}}}{360} = 0.56/\lambda \text{ Hz}$$

where $\bar{\varepsilon}$ is the RMS angle noise (in linear units) $\sim 0.3\ L = 9$ m

$\dot{\bar{\eta}}$ is the RMS angular velocity $\sim 1.3^{o}/s$

λ is the wavelength, m

L is the bomber length ~ 30 m

In terms of Doppler velocity

$$\Delta\dot{R}_s \sim 0.3 \text{ m/s}.$$

For a bistatic system it can be expected that

$$\Delta\dot{R}_{sb} \sim 0.3 \cos \beta/2 \quad \text{m/s}$$

where β is the bistatic angle. The clutter Doppler spread is on the order of

$$\Delta\dot{R}_c \sim v_s\theta \cos \beta/2$$

where v_s is the velocity of the satellites relative to the earth in m/s and θ is the beamwidth in radians.

The S/C improvement by Doppler filtering for this case is then given by

$$\frac{\Delta\dot{R}_c}{\Delta\dot{R}_{sb}} \sim \frac{v_s\theta}{0.3}$$

In order to make this ratio large one wants to make v_s large by using low-altitude satellites and θ large. However, to minimize the total cross-section θ should be as small as possible. For example, if one used a 0.6^{o} beam (0.01 radian) and a 200 km altitude circular orbit satellite (v_s = 7700 m/s) then the Doppler filtering improvement becomes

$$\frac{v_s\theta}{0.3} = \frac{(7700)(0.01)}{0.3} = 257 \text{ or } 24 \text{ dB}$$

A typical improvement needed is 60 dB. Consequently, it appears that aircraft detection is possible only if the aircraft Doppler does not overlap that of the clutter.

5.2 Range Resolution Limitations

The clutter competing with the aircraft is the total clutter within the illuminating beam reduced by the ratio of the bistatic range resolution to the bistatic range extent of the clutter. However, the range cell cannot be made arbitrarily small. If it is smaller than the aircraft dimensions then the aircraft cross-section will decrease in approximately the same ratio as the clutter cross-section and there will be no signal/clutter improvement. If there is signal integration, then the range cell must encompass not only the aircraft but the distance it travels during the integration time. If the integration time is less than about 0.01 s (to assure an

adequately high ground coverage search rate) then for a typical 30 meter length aircraft and 300 m/s velocity the range cell must encompass a distance $\Delta x \lesssim 30 \cos \phi$, where ϕ is the angle between the aircraft velocity and the bistatic direction. (Because of aircraft thickness $\Delta x \gtrsim 5$ m.) The bistatic range resolution corresponding to a length x along the bistatic range direction is

$$\Delta R_B + \Delta x \cos \beta/2 \sim 30 \cos \phi \cos \beta/2$$

where β is the bistatic angle. At large bistatic angles ΔR_B required for a given Δx can become very small for a given Δx so that large bandwidth waveforms would be required. For maximum clutter reduction the range resolution could be made to vary with changes in ϕ and β. However, choosing $\Delta R_B \sim 30$ m is a good estimate for modest values of ϕ and β.

5.3 Bistatic Clutter Cross-Section

The bistatic clutter cross-section, σ_c, for an elemental ground area, dA, is given by

$$\sigma_c = \sigma^o \, dA$$

or

$$\sigma_c = \gamma \cos \phi \, dA$$

where σ^o is the bistatic cross-section density of the illuminated area, γ is the cross-section density of the area projected on the bistatic range and ϕ the bistatic angle of incidence. Both σ^o and γ are functions of the geometry, polarization and terrain.

The bistatic clutter density in the R-$\dot{R}$ plane can be determined for specific bistatic geometries from the Jacobian of the transformation from ground coordinates to R-R coordinates. If J is the Jacobian then the clutter cross-section is

$$\sigma_c = \sigma^o \, dA = \sigma^o \, d \, x \, dy = \sigma^o \, J \, dR \, d\dot{R} \quad *$$

or

$$\sigma_c = \gamma \cos \phi \, dA = \gamma \cos \phi \, J \, dR \, d\dot{R}$$

Since both J and cos ϕ are only geometry dependent they can be combined so that the latter form becomes

$$\sigma_c = \gamma \, J_\phi \, dR \, d\dot{R}$$

J and J_ϕ can be considered relative cross-section densities since

$$J = \frac{\sigma_c}{\sigma^o \, dR \, d\dot{R}}$$

*See Appendix A for a derivation of the Jacobian.

and

$$J_\phi = \frac{\sigma_c}{\gamma \, dR \, dR}$$

The unit of J and J_ϕ is seconds.

Typically σ^o is less than -10 dB[4] for large bistatic angles of incidence (low grazing angles) and $\gamma \lesssim \sigma^o$ since $\cos \phi \lesssim 1$. There may be a strong specular when the normal to the clutter is along the bistatic range direction. Consequently, the clutter from a patch of ground with dimensions comparable to that of an aircraft is

$$\sigma_c = \sigma^o \, dA \sim 10^{-1} \; (30 \times 30) = 90 \; m^2 \sim 20 \text{ dBsm}$$

Clearly an aircraft cannot be separated from the clutter unless either its cross-section is much greater than 20 dBsm or its Doppler is significantly different from that of the clutter. The limitations of Doppler filtering to improve S/C were indicated in Section V-A.

An aircraft cross-section is on the order of 15 dBsm so that the maximum S/C for a stationary aircraft is on the order of only -5dB. The S/C will be much less with practical beamwidths

which contain clutter areas with dimensions large compared to those of the aircraft. Consequently, detecting moving aircraft will be possible only if their Doppler is separated sufficiently from that of the clutter.

5.4 Sample Waveforms from Range-Doppler Maps

Sample waveform designs based on the R-$\dot{R}$ maps of the clutter and aircraft for a few bistatic configurations are now considered. It is noted that resolution and ambiguity for a bistatic and monostatic radar are defined in terms of PRF, bandwidth and integration time in the same way.

5.4.1 Low Altitude Satellites

The first example is for a bistatic radar on a pair of co-orbital low altitude satellites whose orbit plane is assumed adjusted to permit surveillance of suitable portions of the fence. (Several pairs of satellites would be needed for continuous coverage because of the limited horizon of low altitude satellites.)

Figure V-2 illustrates the low altitude bistatic radar for this example. The antenna on each satellite is assumed to have a pencil beam and the two beams are equal. Since satellite S_1 is closest to the view point $x_o y_o$, its beam intersection with the ground will be entirely within that of satellite S_2 and hence will define the illuminated clutter region as indicated in Fig. V-3 The range and Doppler distribution of the clutter within this region

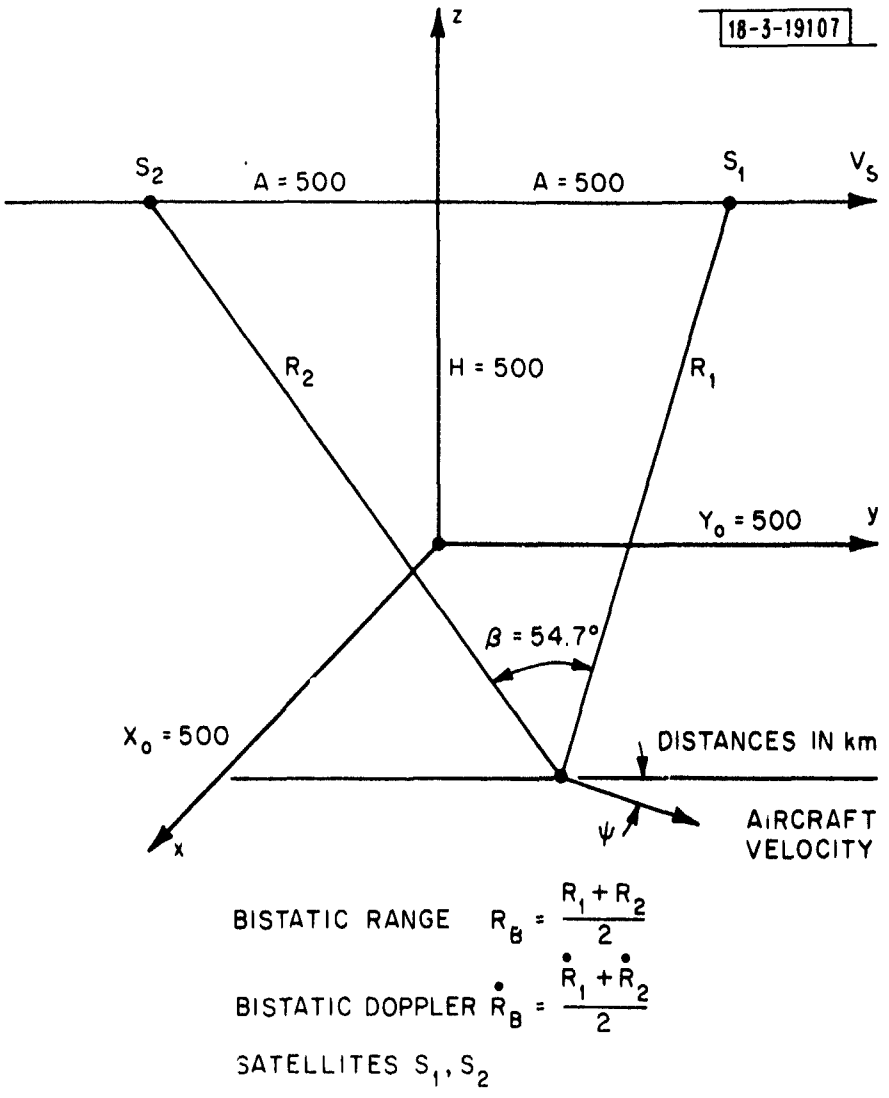


Fig. V-2. Low altitude bistatic radar.

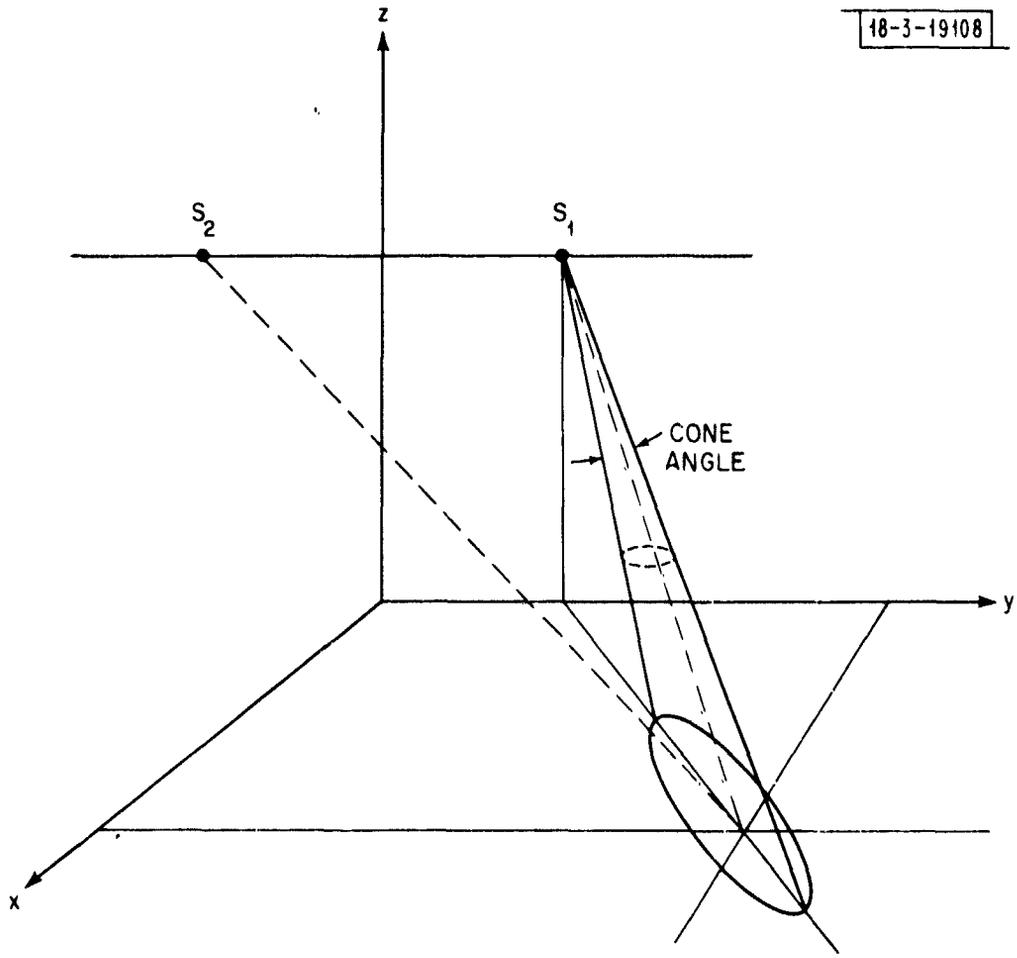


Fig. V-3. Intersection of coinical beam with clutter plane for a bistatic radar (beamwidth exaggerated).

can be determined from the mapping of the clutter boundary onto the R-$\dot{R}$ plane as shown in Fig. V-4 for a beamwidth of 0.5^{o}. The contour shown is assumed to be along the first null of the beam. It is also assumed that the beam sidelobes are sufficiently deep that any clutter contribution through them can be neglected.

Also shown in Fig. V-4 is the R-$\dot{R}$ mapping of 0.3 km/s ($\sim$ Mach .9) aircraft on the beam boresight with headings relative to the satellites' velocity (see Fig. V-2) of between 0 and 360 degrees. Each relative heading corresponds to a particular Doppler along the line indicated in Fig. V-4.

The relative clutter density J_{ϕ} in the R-$\dot{R}$ plane is given in Fig. V-5 for arbitrary points x, y on the earth. For the given viewing geometry with x = y = 500 km, J_{ϕ} = 160 seconds. J_{ϕ} is approximately constant within illuminated regions a few tens of kilometers in extent as indicated by the 5^{o} beam intersection in Fig. V-5. For large illuminated regions J_{ϕ} will vary over the illuminated region, so it would be appropriate to determine J_{ϕ} separately for each range slice or group of range slices. In this case, with a 0.5^{o} beam, it is not necessary to do this and J_{ϕ} can be assumed constant within the beam.

If a resolution cell is fully occupied by clutter then selecting the viewing geometry to minimize J_{ϕ} minimizes the clutter competing with an aircraft in that cell, but may be futile for practical S/C ratios as indicated in Section V-1. On the other

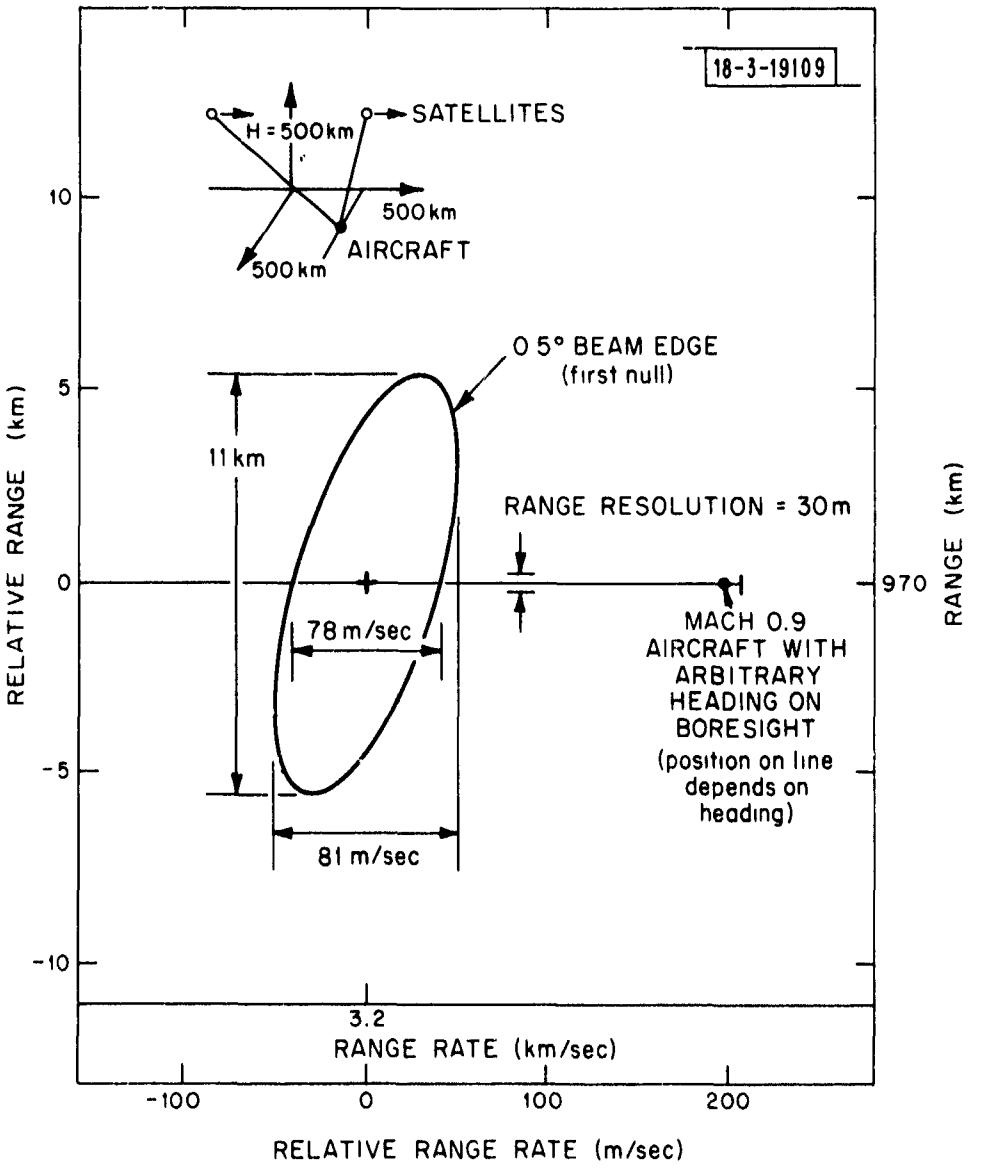


Fig. V-4. Clutter and aircraft mapped onto the range-doppler plane for low altitude satellites.

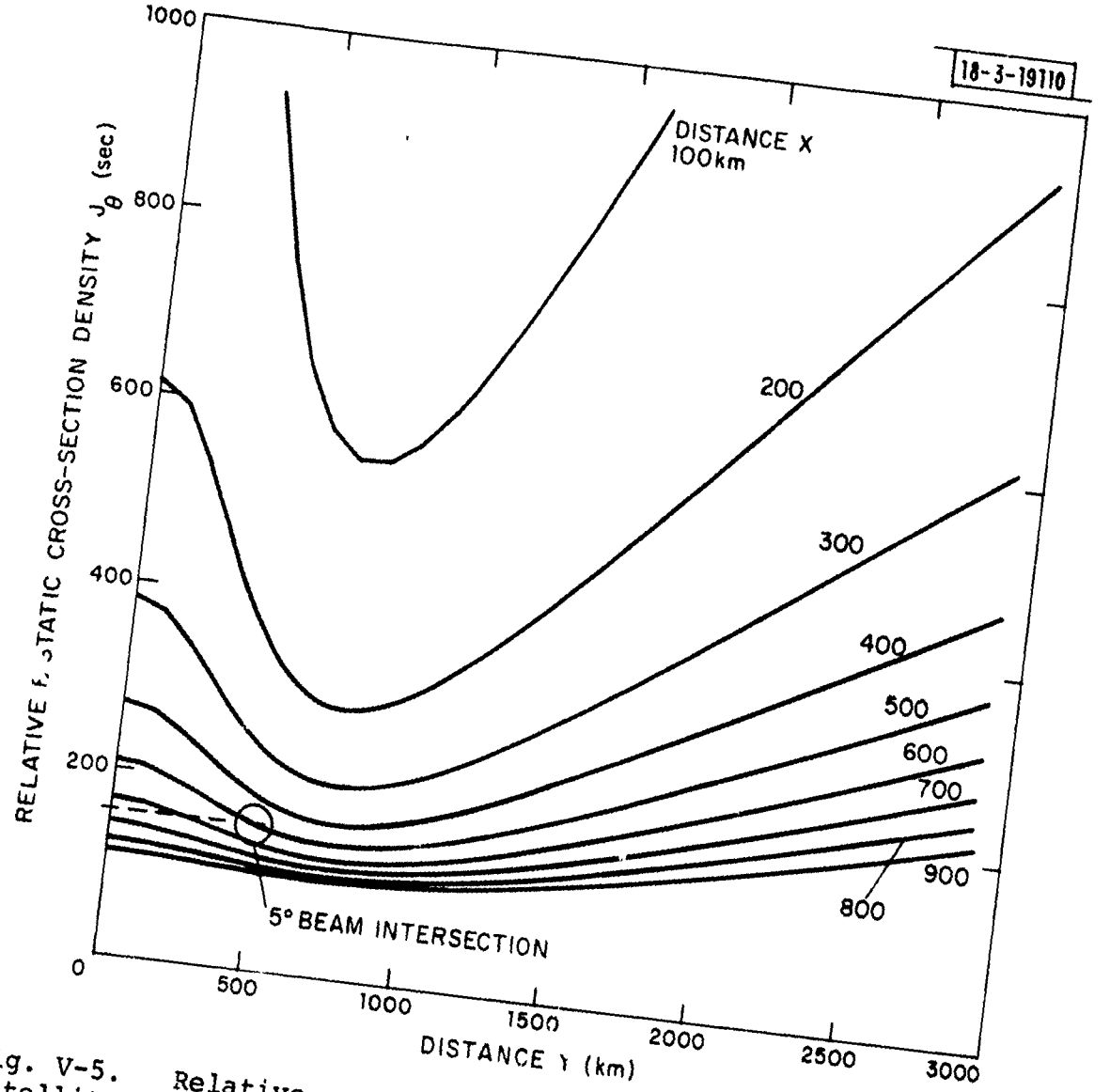


Fig. V-5. Relative cross-section density for low altitude satellite example.

hand, recalling that $\sigma_c = J_\phi dRdR$, we note that with a fixed range resolution dR and a fixed beam size with its corresponding fixed total clutter within the beam (except for geometry dependence of γ), selecting J_ϕ large results in the clutter being concentrated in a narrow Doppler band. A limiting case is when J_ϕ becomes infinite corresponding to a zero clutter Doppler and clutter Doppler spread. When the selected geometry also results in the aircraft and clutter being separated in Doppler, then the narrow clutter Doppler band can facilitate clutter filtering and target detection.

For determination of waveform parameters a 0.5^o beam is assumed. The characteristics of the clutter in the beam are summarized in Table V-1.

The range and Doppler ambiguities are related by

$$\frac{R_a}{\lambda}\dot{R}_a = 75$$

$$R_a = \frac{c}{2}T_p \qquad \text{(V-1)}$$

$$\dot{R}_a = \frac{\lambda}{2T_p}$$

where R_a = range ambiguity, KM

$\dot{R}_a$ = Doppler ambiguity, KM/s

λ = wavelength, M

T_p = interpulse period, s

c = velocity of light, 3×10^5 KM/s

TABLE V-1

CLUTTER CHARACTERISTICS FOR
LOW ALTITUDE BISTATIC RADAR EXAMPLE

Doppler spread	$\Delta\dot{R}_s$	=	81 m/s
Range spread	ΔR_s	=	11 km
Illuminated area	A	=	170 km^2
Bistatic incidence angle	ϕ	=	51^o
Jacobian	J	=	250 sec
J cos θ	J_θ	=	160 sec
Total clutter cross-section	σ_T	=	$\gamma\ 10^8\ m^2$
Clutter cross-section in clutter filled R-$\dot{R}$ cell	σ_c	=	$\gamma J_\theta dR d\dot{R} = 160\ \gamma\ dR d\dot{R}\ m^2$

Since the aircraft must be in the beam for detection, it will be within the range interval of the clutter as defined by the beam (for most practical geometries). In order to prevent clutter foldover or ambiguous range measurements and to provide as large an unambiguous Doppler interval as possible, the range ambiguity is set equal to the range extent of the clutter in the beam. The inter-pulse period and the Doppler ambiguity are found from Eq. V-1. The basic waveform parameters are summarized in Table V-2 for γ = 0.03, 0.1 and 0.3 m.

Since the clutter density is approximately constant within the beam, that range cell which has the greatest spread in clutter Doppler will have the greatest clutter cross-section. For the example under consideration this is approximately the range cell though the beam boresight (see Fig. V-4) which has an $\dot{R}$ spread of approximately 78 m/s. The clutter within that range cell is, for a fairly conservative value of γ = 0.1,

$$\Delta\sigma_c = 3.7\ 10^4\ m^2 = 45\ \text{dBsm}.$$

These clutter characteristics are included in Table V-2. Other range cells have smaller Doppler spreads and hence have smaller clutter cross-sections and greater clear areas.

When the clutter Doppler spread is a small fraction of the Doppler ambiguity spacing there is a substantial clear area

TABLE V-2

WAVEFORM AND CLUTTER PARAMETERS
FOR LOW ALTITUDE SATELLITE EXAMPLE

Waveform

Wavelength, λ , m	0.3	0.1	0.03
Range ambiguity, R_A , km	11.0	11.0	11.0
Pulse period, T_p , μs	74	74	74
Doppler ambiguity, $\dot{R}_A$, m/s	2000	680	200
Pulse repetition rate, PRF , KHz	13.5	13.5	13.5
Range resolution, ΔR, m	30	30	30
Pulse length, τ , μs	0.2	0.2	0.2
Doppler spread/Ambiguity spacing, %	4	12	39
Clear area %	96	88	61

Clutter

$\gamma \sim 0.1$

Total Clutter	$\sigma_c \sim 10^7$ m^2	= 70.4 dBsm
Max. Doppler velocity spread in range cell	$\Delta\dot{R}_{SC}$	= 78 m/s
Max. clutter in range cell	$\Delta\sigma_c$	= 3.7×10^4 m^2 = 46 dBsm

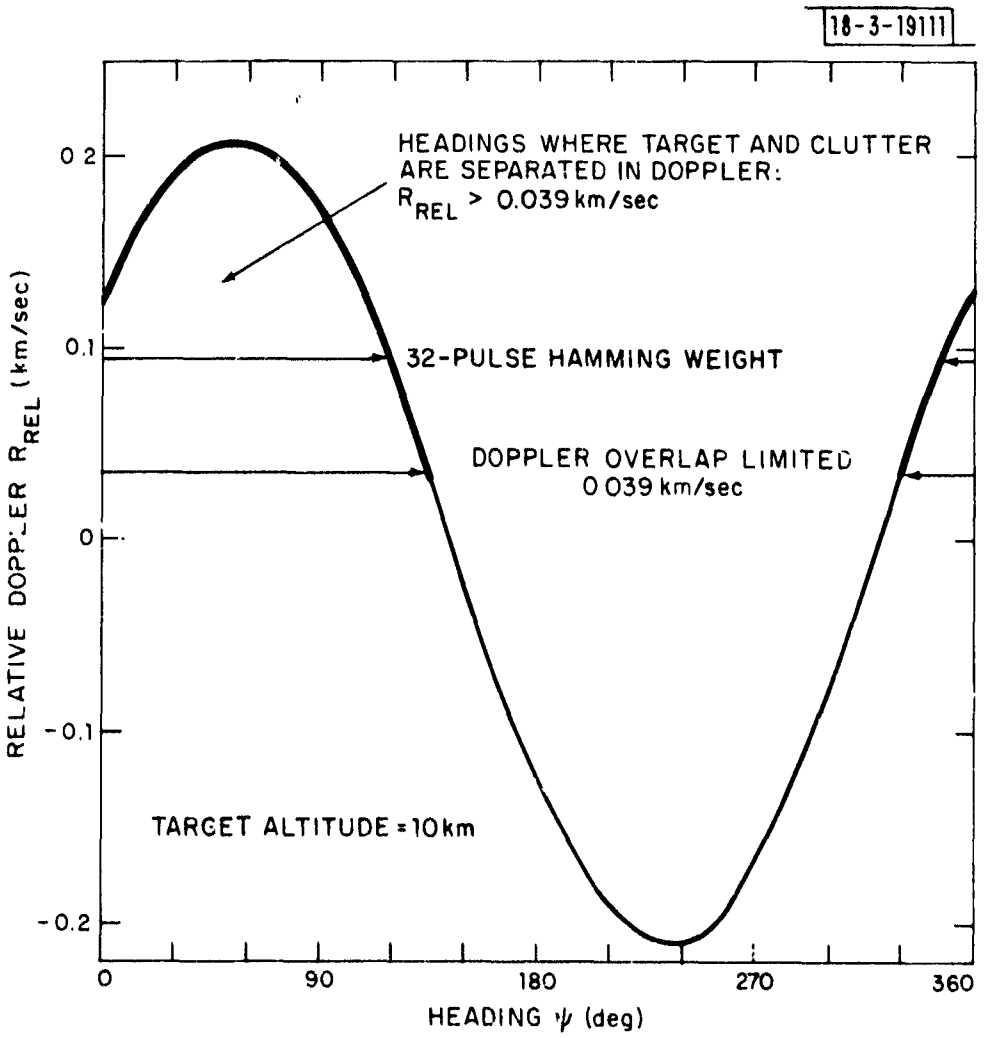


Fig. V-6. Target-clutter relative doppler for low altitude satellite example.

in the R-$\dot{R}$ plane free of clutter. This fraction and the corresponding fraction of clear area are also included in Table V-2 as percentages. A longer wavelength results in a greater percentage of clear area, however, a correspondingly larger aperture is then required to keep the beamwidth constant.

Only the example with $\gamma = 0.1$ is subsequently considered. For the aircraft to be separate from the clutter in the central range cell, the target $\dot{R}$ must differ from that of the clutter by at least half of the clutter $\dot{R}$ spread, or 39 m/s. Figure V-6 shows the difference in $\dot{R}$ between an aircraft on the beam boresight and the co-located clutter as a function of the relative aircraft heading (See Fig. V-2). The maximum relative $\dot{R}$ is 210 m/s, well within the Doppler ambiguities. It is evident that the relative $\dot{R}$ will exceed 39 m/s for relative headings from -30° to 135° or for about 90% of all relative headings of interest (i.e., aircraft with only positive $\dot{R}$ or by symmetry with only negative $\dot{R}$). (Relative headings 180° from these also satisfy the Doppler separation constraint but in this example they would represent aircraft traveling away from the U. S. and hence pose no threat.) In either case the magnitudes of the relative $\dot{R}$'s are the same. For aircraft at other locations in this range cell the relative Doppler would be little different because the dimensions of the beam intersection with the earth are small compared to the ranges to the satellites. A reduction in the allowable range of relative headings due to

waveform weighting will be discussed below. The orientation of the satellite orbit relative to potential aircraft compass headings should be selected, if possible, so that the aircraft will always be separate from the clutter in Doppler.

The relation of the clutter, aircraft and waveform ambiguities for an aircraft on the beam boresight with maximum relative Doppler is summarized in Fig. V-7.

To obtain a 15 dB signal/clutter ratio in this example, 45 dB of clutter rejection is required. In order to obtain the necessary Doppler sidelobes some form of waveform weighting is required. However, since the beam limits the range extent of the clutter and the PRF is selected to prevent clutter foldover in range, only the waveform response at zero relative range need be considered. (See Fig. V-7). One-way Hamming weighting can provide -42 dB sidelobes with only 1.34 dB of mismatch loss. Figure V-8 shows a cut along the Doppler axis of the ambiguity function of a 32 pulse one way Hamming weighted burst. Except for the first four sidelobes they are all below the desired 45 dB. The clutter is spread over 1560 Hz which corresponds approximately to the width of the region containing the four sidelobes exceeding -45 dB. The worst effect resulting from clutter located near the target or ambiguity as indicated in Fig. V-7 would be to reduce the S/C by less than about 3 B. On this basis the sidelobes can reject the clutter when it is between 1 and 12.5 KHz (52 and 630 m/s). Since

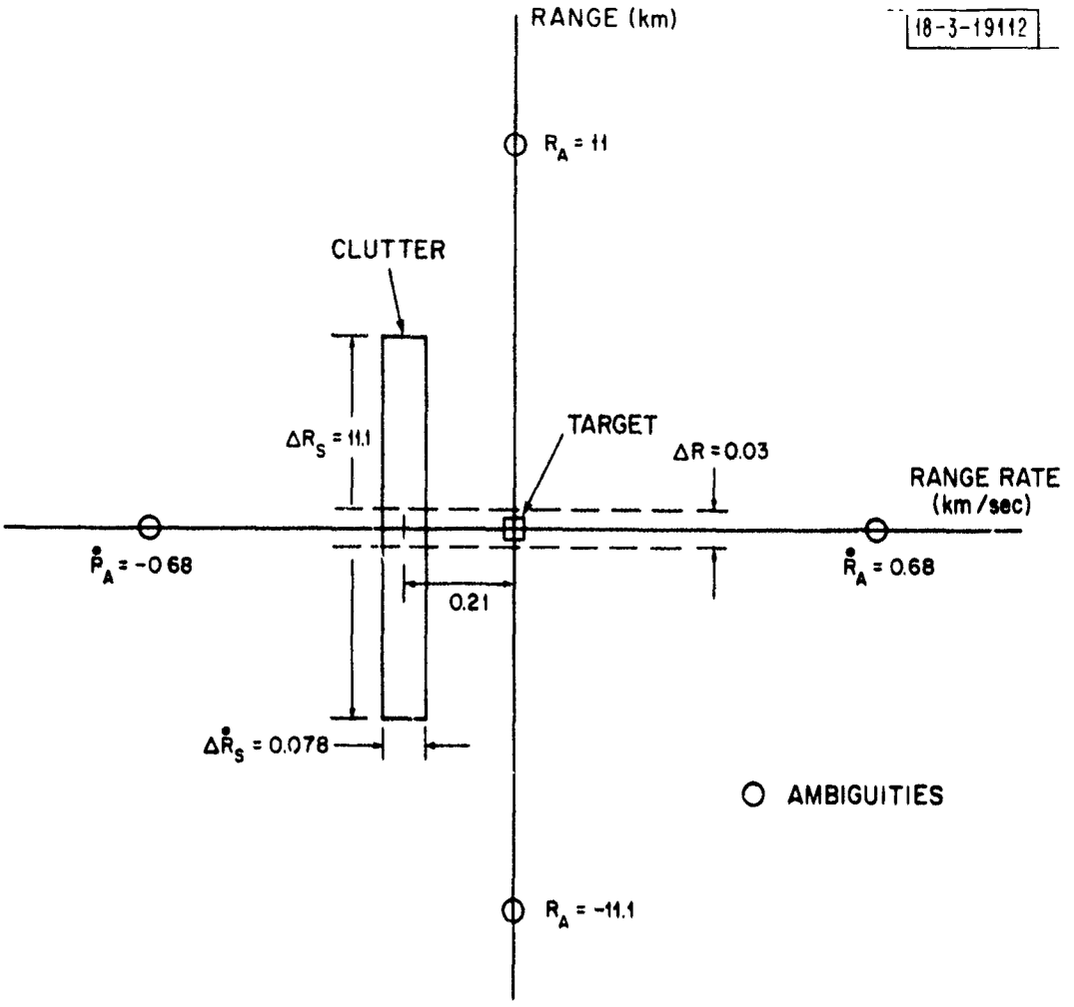


Fig. V-7. Ambiguity locations for low altitude satellite example.

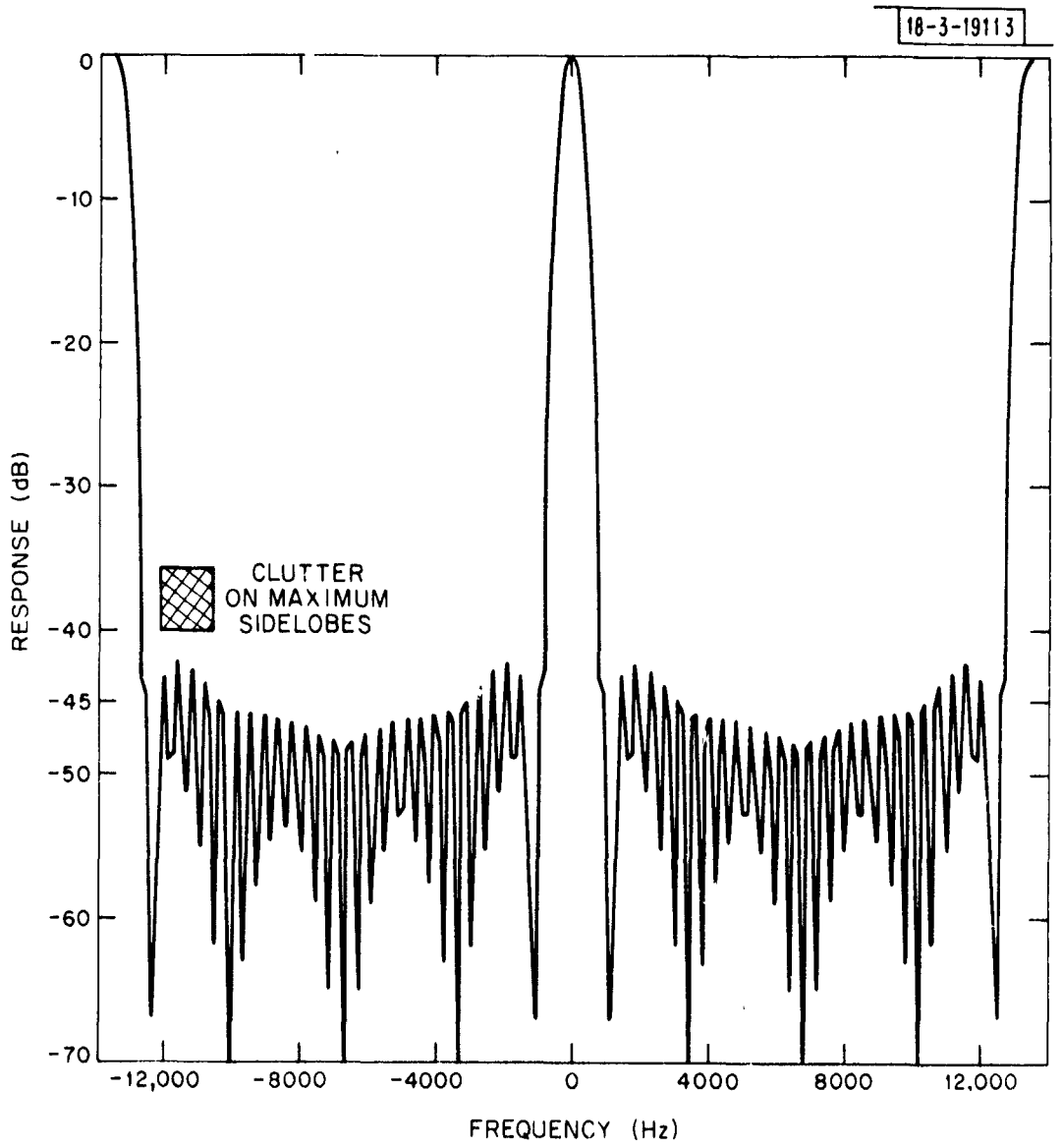


Fig. V-8. Ambiguity function on doppler axis for 32 pulse one way hamming weighting and the waveform of Table 1.

the clutter Doppler spread is 78 m/s an aircraft clutter separation greater than 52 + 78/2 = 91 m/s will assure adequate clutter suppression. From Fig. V-6 it is seen that a relative Doppler separation of 91 m/s corresponds to target headings between -11^{o} and 117^{o}, or about 70% of the possible headings of interest.

The requirement that the peak sidelobes of the ambiguity function be below -45 dB is conservative since the clutter Doppler spread also includes sidelobe nulls. The integrated response more accurately characterizes the response of the waveform to clutter. Figure V-9 gives the integrated response of the above waveform for various locations of the center of the clutter Doppler spread. When the clutter is at zero frequency the integrated clutter is nearly 10 dB below that if the ambiguity response were unity throughout the region occupied by the clutter. The net effect is that the integrated response is significantly less than that indicated by the sidelobes on the Doppler axis. Since the integrated response is less than -50 dB between ambiguities, there will be a 5 dB margin of clutter rejection with this waveform.

The duty cycle of the waveform can be increased (for higher average power) without altering the ambiguity response on the Doppler axis by using an FM pulse with a 5 MHz bandwidth, the same bandwidth as the original unmodulated 0.2 μs pulse.

The choice of 32 pulse Hamming weighting requires an integration time of 32 ÷ PRF - 2.4 ms. The Doppler resolution is

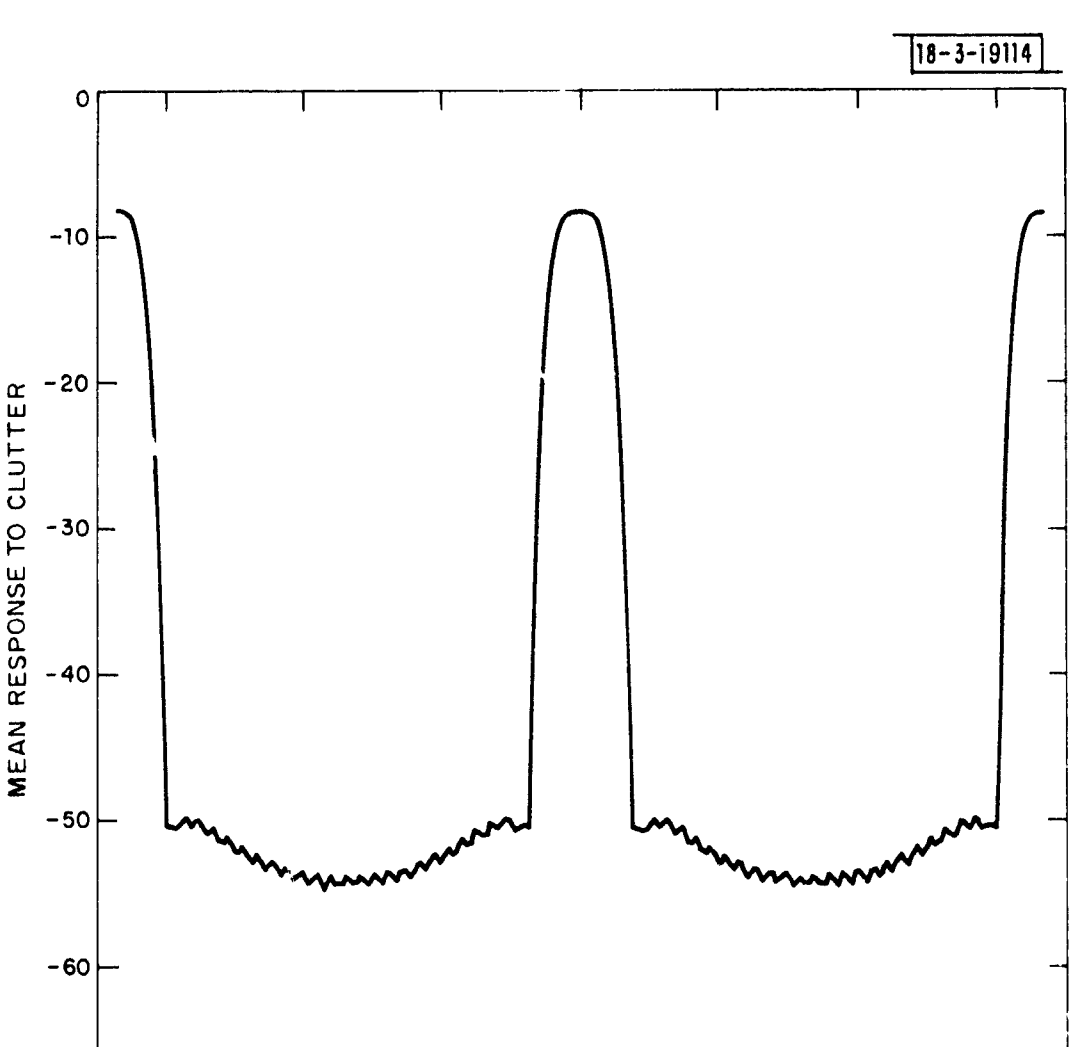


Fig. V-9. Integrated ambiguity function response to clutter for hamming weights.

20 m/s and the corresponding coverage rate is

$$\left(\frac{dA}{dt}\right) = \frac{170 \text{ km}^2}{2.4 \text{ ms}} = 7 \times 10^4 \text{ km}^2/\text{s}$$

which exceeds the 2.9×10^3 km^2/s rate required to search the entire fence in one hour (Section III). Several tradeoffs are possible to reduce the coverage rate to the minimum that is necessary and thereby use the minimum power-aperture as indicated in Fig. III-1.

5.4.2 High Altitude Satellites

A second example of the application of $\dot{R}$-$\dot{R}$ maps to waveform design is for the bistatic radar with the satellites' angular rates at apogee equal to that of the earth. The coverage by this radar was given in Fig. IV-3. Since the satellites' rates at apogee match that of the earth, the clutter Doppler is zero as with a geostationary satellite. The principal differences between this satellite configuration and that of a geostationary one are that the bistatic geometry is significantly different providing different bistatic aspect angles and that the 12 hour period satellites are not on station continuously. Also as a result of the satellites' motions the clutter is not zero at all times.

$\dot{R}$-$\dot{R}$ clutter maps of the surveillance fence shown in Fig. V-10 with corresponding $\dot{R}$-$\dot{R}$ maps of aircraft at various compass headings within the fence are presented in Figs. A-4 to A-11 of

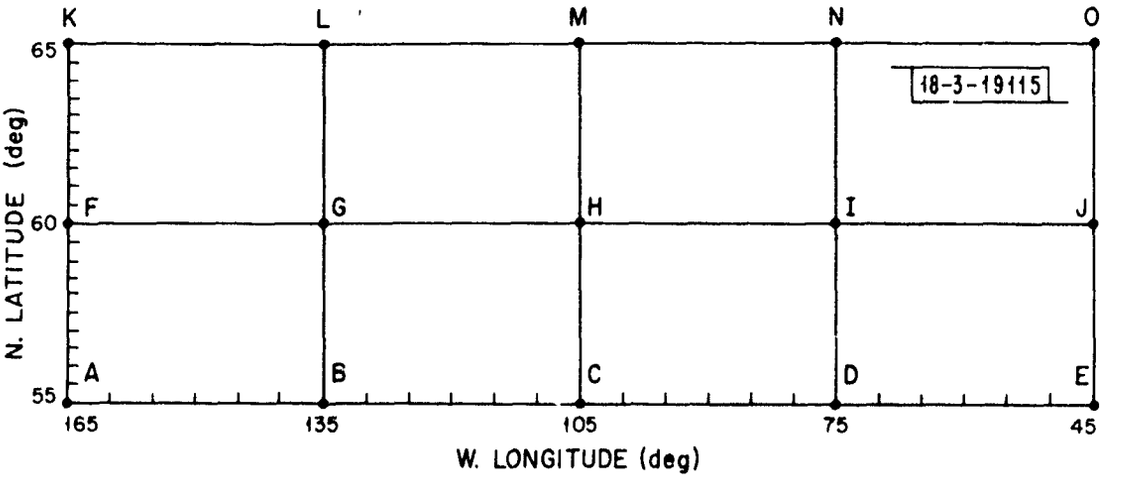


Fig. V-10. Surveillance fence with grid of points mapped onto the R-$\dot{R}$ plane.

Appendix A. The surveillance fence is divided into a grid 5° longitude by 1° latitude and each grid point mapped into the $R-\dot{R}$ plane to characterize the clutter. Aircraft at each grid point with an altitude of 10 km and moving horizontally at 0.3 km/s on compass headings of 135, 180 and 225 degrees are also mapped into the $R-\dot{R}$ plane. These headings bound those associated with the representative routes described in Section I. The Doppler spread of the clutter or the aircraft, over the extent of the fence, is small (<15 m/s) so that their relation in the $R-\dot{R}$ plane is approximately that of the line segments shown in Fig. V-11. For Fig. V-11 the satellites are at apogee and 1 and 3 hours past apogee. The clutter and aircraft are seen to be widely separated in Doppler (>70 m/s) for periods of at least 6 hours (3 hours before and 3 hours after apogee).

The intersection of a 0.1° beam and the earth's surface is mapped in Fig. V-12 for point I of the fence for 1 hour and 3 hours after apogee. (See Fig. V-10). At apogee the satellite rates match the earth rate so that the clutter Doppler is zero and its spread is zero. The Doppler spread across the beam and hence the clutter Doppler spread in a range cell is seen to be very small (<0.6 m/s) for this example. The total clutter cross-section and cross-section in a bistatic range cell can be found from maps like this and the clutter density. (However, the actual clutter Doppler spread may be on the order of a few meters per second due to motion

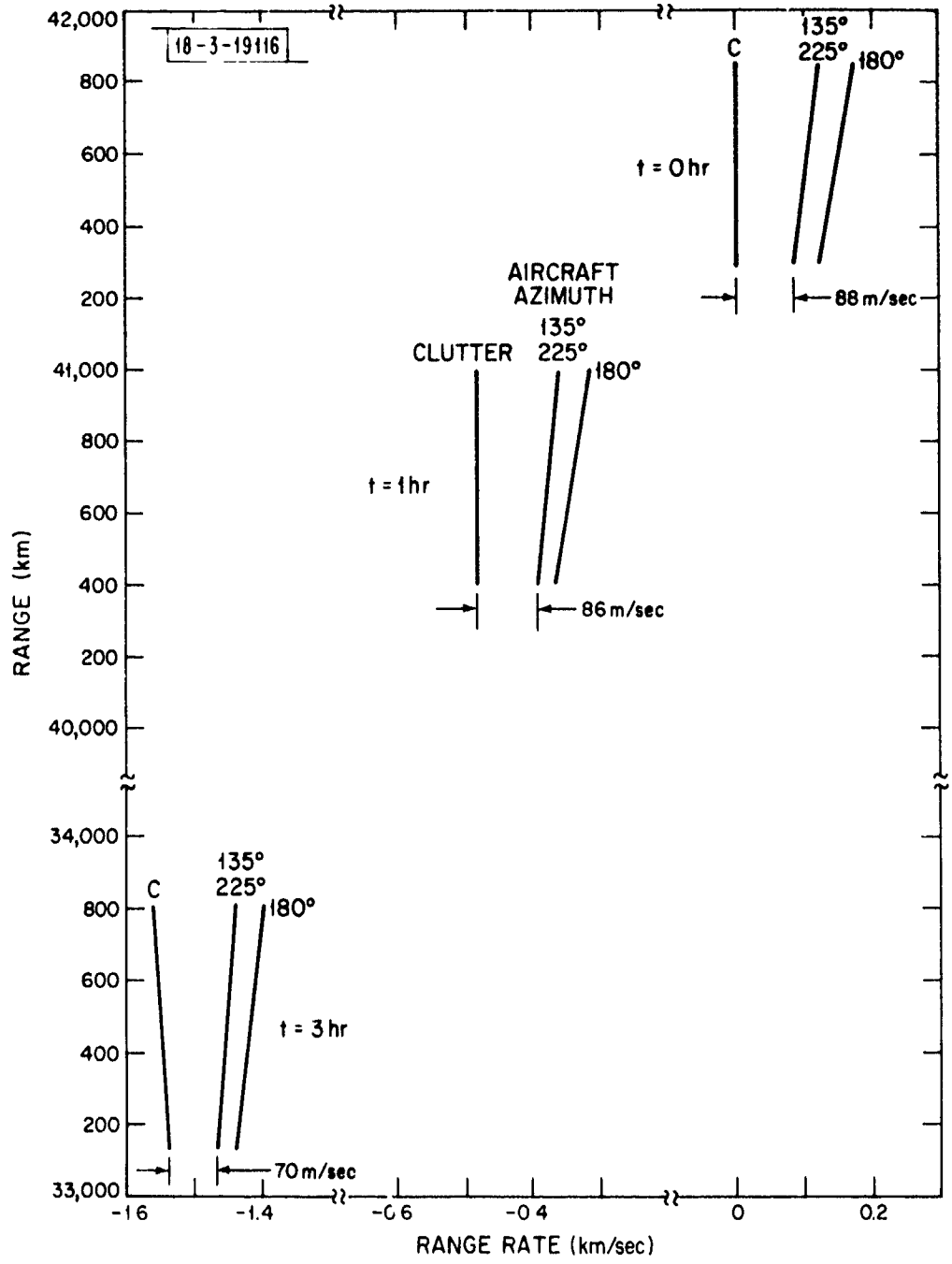


Fig. V-11. Clutter and aircraft within the surveillance fence.

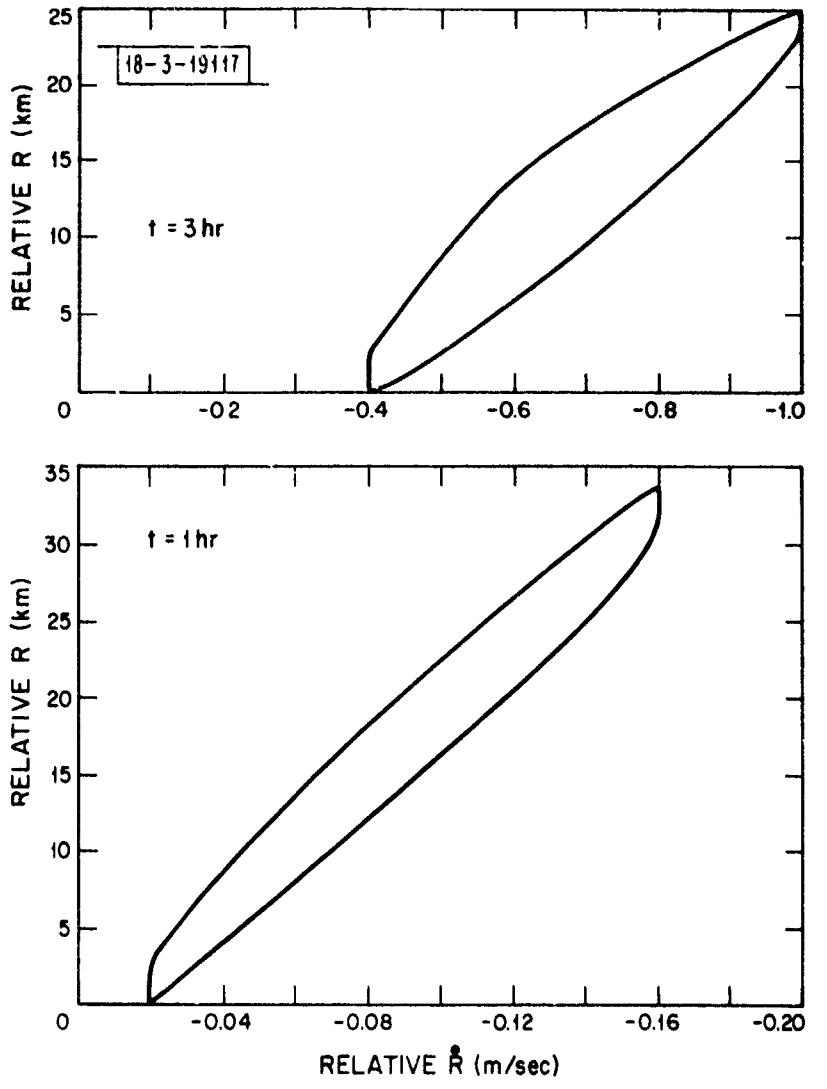


Fig. V-12. R-$\dot{R}$ map of clutter on beam edge.

of individual scatterers comprising the clutter. The rms clutter velocity for a monostatic radar is typically $\bar{v}_{cm} < 4$ m/s[6] so that for a bistatic system it can be expected to be in the order of $\bar{v}_{cb} \lesssim 4 \cos \beta/2$ m/s where β is the bistatic angle.) The bistatic range extent of the clutter is used to determine the waveform period as was done with the low-altitude satellite example.

The variation of the clutter density over the fence is illustrated in Figs. A-12 and A-13 of Appendix A for this example. The clutter density and clutter cross-section in a range slice for the beam boresighted on point I are tabulated in Table V-3 which summarizes the clutter characteristics and possible waveform parameters. Possible techniques for obtaining large clutter rejection are discussed in Section VI. Although the clutter distribution (Fig. V-11) varies with time, the clutter range extent, which determines the waveform characteristics, does not vary greatly throughout the fence nor with time so that a single waveform could be applicable independent of time. However, both the range and Doppler location of the filters would need to be shifted as a function of time.

The maximum dwell time in each beam position, and hence the maximum number of pulses N that can be integrated consistent with the required coverage rate is

$$N \leq \frac{\text{illumination area}}{\text{coverage rate}} \text{ PRF}$$

and is included in Table V-3. N is very large and will not limit attainment of the required clutter filter characteristics.

The aircraft cross-section is dependent on the bistatic viewing geometry and requires four angles for its description. These four angles are the bistatic angle, the bistatic pitch, the bistatic aspect and the bistatic roll which are illustrated in Appendix A, Figs. A-2 and A-3. The variations of these angles over the various aircraft locations at the $5^{\circ} \times 1^{\circ}$ grid points within the surveillance fence are tabulated in Table V-4. Three aircraft headings at each grid point are considered: 135° (south-east), 180° (due south) and 225° (south-west). The average, maximum, minimum and spread (difference between the maximum and minimum) of the four angles is given for the satellites at apogee (T = 0 HR) and three hours later (T = 3 HR).

Table V-4 indicates, for this example, that although the bistatic angle for the viewing of aircraft anywhere within the surveillance region is nearly constant (and not very large), the bistatic pitch, aspect and roll have significant variations. Thus, it is expected that the aircraft cross-section would vary significantly depending on its location and heading and the time of observation or locations of the satellites. Aircraft maneuvers away from the straight and level flight would result in further variations in the bistatic viewing angles. The effect on aircraft bistatic viewing angles of the bistatic radar on satellites on other

TABLE V-3

WAVEFORM AND CLUTTER PARAMETERS FOR
HIGH ALTITUDE SATELLITES

Time from apogee - hr	0	1	3
CLUTTER			
$\dot{R}$ extent, m/s	~0	0.14	0.6
Range extent, km	35	34	25
$\dot{R}$-R Clutter density, dbs	∞	66	58
$\dot{R}$ spread, m/s[(a)]	~0	0.03	0.2
Clutter σ, dbsm[(a)]	56	56	56
Clutter rejection[(b)]	56	56	56
Bistatic angle, deg	60	60	80
WAVEFORM[(c)]			
Period, μs	230		
prf, Hz	4400		
$\dot{R}$ ambiguity, m/s	215		
Max. no. integrated pulses[(d)]	5700		

(a) In 30 m range slice

(b) Required for 15 db S/C on 15 dbsm target

(c) Range ambiguity equal to clutter extent; λ = 0.1 m

(d) From maximum dwell time consistent with ground coverage rate

TABLE V-4

SUMMARY OF BISTATIC AIRCRAFT VIEWING ANGLES*

Time After Apogee	T = 0 HR				T = 3 HR			
	Heading = 135°							
Angles, Deg.	Average	Spread	Max	Min	Average	Spread	Max	Min
Bistatic Angle	58	1	59	58	78	2	79	77
" Pitch	39	80	70	-10	39	77	69	-9
" Aspect	195	111	250	139	205	112	261	149
" Roll	74	148	125	-23	73	149	126	-24
	Heading = 180°							
Bistatic Angle	58	1	59	58	78	2	78	77
" Pitch	0	98	-49	49	1	96	49	-47
" Aspect	160	31	178	148	174	30	189	159
" Roll	90	97	139	41	89	100	138	38
	Heading = 225°							
Bistatic Angle	58	1	59	58	78	2	79	77
" Pitch	-39	80	10	-70	-38	80	11	-69
" Aspect	195	111	250	139	203	107	256	149
" Roll	129	148	203	55	126	146	199	53

*For the satellite orbits of the high altitude example of Section V-5.3 and Figure IV-3. See also Appendix A, Figures A-2 and A-3.

orbits needs investigation. However, it is expected that if a large fence is to be surveyed, then the changes in the aircraft bistatic viewing angles will also be large. It is also expected that the variation of bistatic angle for lower altitude satellites would be greater than for the example presented. It is also noted that bistatic measurements of aircraft cross-section require combinations of four different angles which involves an extensive number of observations. For example, if only five different values of the four bistatic angles were selected (which is very unlikely to be adequate) then 5^4 or 625 separate measurements are required.

The sample waveform designs of this section have served to illustrate some of the characteristics and applications of bistatic $\dot{R}$-$\dot{R}$ maps of clutter and aircraft and of clutter density in the $\dot{R}$-$\dot{R}$ plane. They demonstrate the possibility of selecting relatively simple waveforms that could provide aircraft detection consistent with the clutter filtering. The possible need for tracking the center of the filters in both range and Doppler was illustrated. For both the low and high-altitude satellite examples the target and clutter were separated so that detection is possible provided Doppler filters have sufficiently low sidelobes for the assumed bistatic cross-sections. There is a need for wideband waveforms at large bistatic angles if there is to be maximum clutter rejection. Based on these two examples, it is not expected that waveforms will be a limiting factor in the design of satellite-borne bistatic radar for detection of aircraft. Clutter filters are considered in the next section.

VI. FILTER DESIGN

6.1 Waveform Weighting

Waveform weighting is employed to reduce range and Doppler sidelobes to levels sufficiently low that clutter can be rejected. An application of Hamming weighting is given in Section V. An example of viewing the earth from 40,000 km that resulted in a clutter cross-section of ~60 dBsm and -60 dB sidelobe level is given in Section III. Since the need of sidelobe levels below that attainable with Hamming weighting may arise, other weightings will be briefly considered here.

Weighting results in a signal/noise ratio loss when compared to an unweighted waveform. Since the signal is coherently integrated, the signal energy is proportional to the square of the sum of weights and the noncoherent noise energy is proportional to the sum of the squares of the weights. Therefore, the S/N for a weighted waveform (on receive only) is proportional to

$$(S/N)_w \sim \frac{\left(\sum_{n=1}^{N} W(n)\right)^2}{\sum_{n=1}^{N} W^2(n)}$$

where W(n) are the weights and N the number of pulses. The S/N for the unweighted waveform, W(n) = 1, is proportional to the number of pulses N, so that the S/N losses due to one-way weighting are

$$\text{Loss}_1 = \frac{\left(\sum_{n=1}^{N} W(n)\right)^2}{N \sum_{n=1}^{N} W^2(n)}$$

For unequal weighting on both transmit and receive the loss is

$$\text{Loss}_2 = \frac{\left(\sum_{n=1}^{N} \left(W_r(n)\ W_t\ (n)\right)\right)^2}{N \sum_{n=1}^{N} \left(W_r(n)\ W_t(n)\right)^2}$$

This loss will be determined when considering various weightings.

6.1.1 Hamming Weighting

Hamming weighting on receive only results in -42 dB sidelobes. The sidelobe level is insensitive to the number of pulses over which the weighting is made as long as the number of

pulses provides an adequate approximation to the integral of the Hamming weighting function. Figure V-8 shows the response for weighting over 32 pulses. The S/N loss is only 1.34 dB.

Lower sidelobes result with weighting on both transmit and receive. Figure VI-1 is the Doppler axis cut of the ambiguity function for two-way Hamming weighting over 32 pulses. The sidelobe levels are about 20 dB lower than for one-way weighting and the loss is only 2.6 dB.

6.1.2 Weights from Digital Filter Design

It is possible to design digital finite impulse response filters with very low sidelobes.[7] Using such a filter to process the received waveform can be expected to result in substantial clutter reduction capability. Using a computer program[8] for the design of optimal finite impulse response (FIR) linear phase filters, some filter responses have been calculated. One example is given in Fig. VI-2. The filter specifications and resulting weights are given in Table VI-1. The depth of the sidelobes is a function of filter length (the number of pulse weighted), and the widths of the pass, stop and transition bands. A wide transition band tends to result in smaller sidelobes but will also tend to reduce the clear area between ambiguities. As indicated in Section V a small clear region restricts the aircraft headings for which the clutter can be rejected.

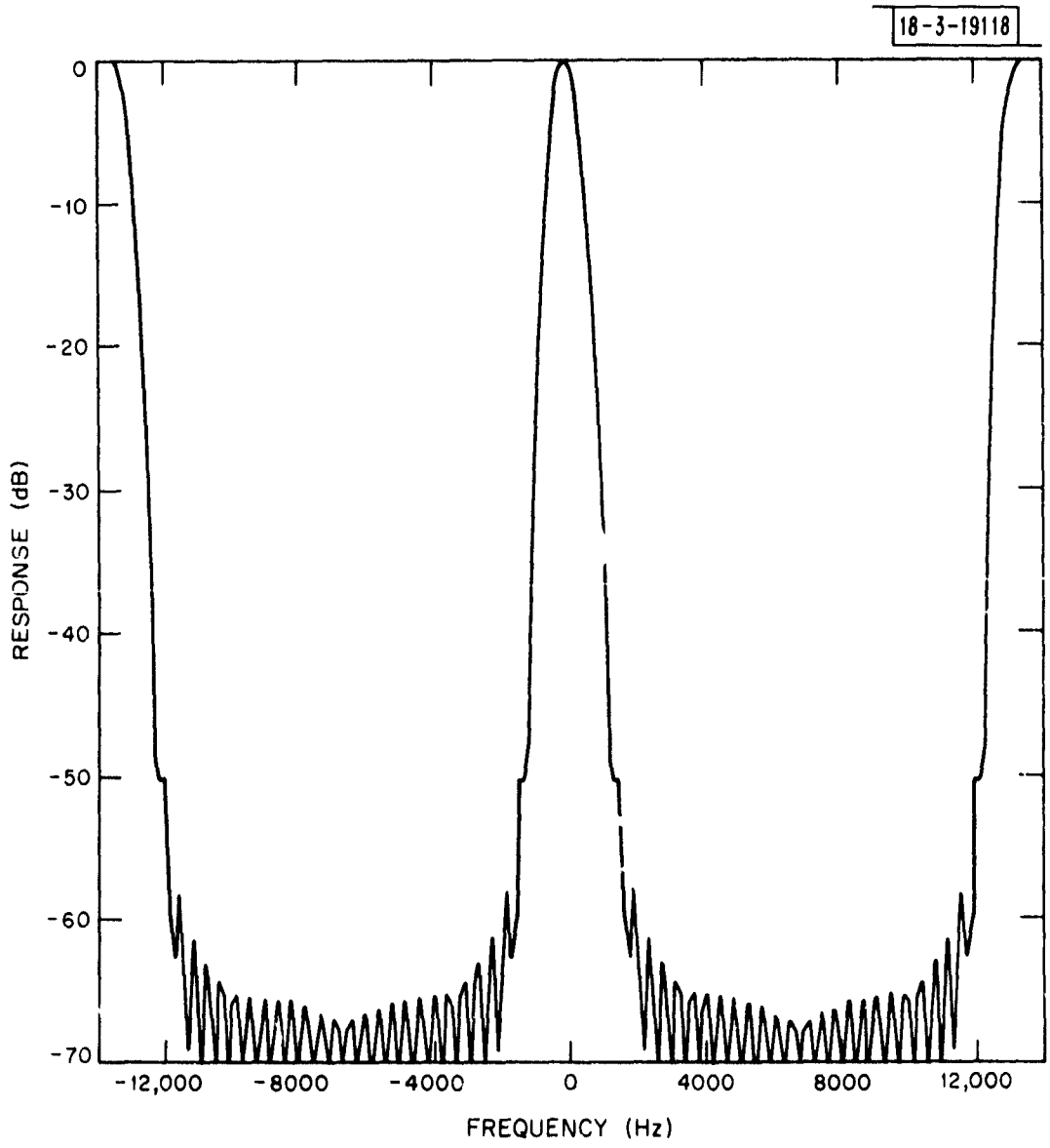


Fig. VI-1. Ambiguity function on doppler axis for 32 pulse two-way hamming weighting.

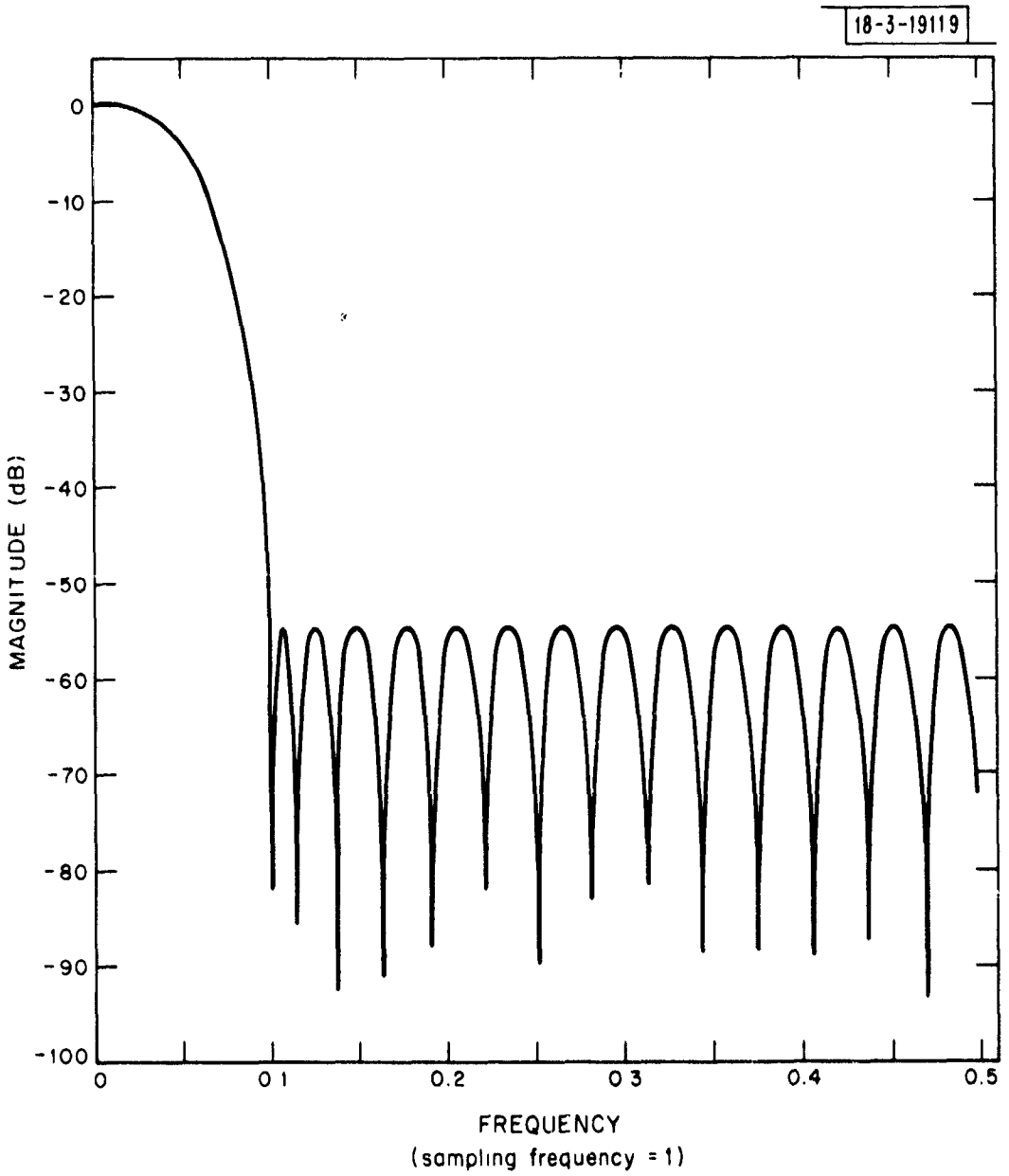


Fig. VI-2. Response of digital finite response filter defined in Table VI-1.

TABLE VI-1

PULSE WEIGHTING DERIVED FROM DIGITAL FILTER DESIGN:
-55db Sidelobes

FINITE IMPULSE RESPONSE (FIR)
LINEAR PHASE DIGITAL FILTER DESIGN
REMEZ EXCHANGE ALGORITHM

BANDPASS FILTER

FILTER LENGTH = 32

***** IMPULSE RESPONSE *****

H(1) = -0.21792529E-02 = H(32)
H(2) = -0.33740327E-02 = H(31)
H(3) = -0.51930882E-02 = H(30)
H(4) = -0.67545921E-02 = H(29)
H(5) = -0.73748156E-02 = H(28)
H(6) = -0.62420666E-02 = H(27)
H(7) = -0.25451574E-02 = H(26)
H(8) = 0.43474101E-02 = H(25)
H(9) = 0.14719278E-01 = H(24)
H(10) = 0.28370515E-01 = H(23)
H(11) = 0.44553712E-01 = H(22)
H(12) = 0.62006533E-01 = H(21)
H(13) = 0.79088032E-01 = H(20)
H(14) = 0.93998909E-01 = H(19)
H(15) = 0.10505038E+00 = H(18)
H(16) = 0.11093324E+00 = H(17)

	BAND 1	BAND 2
LOWER BAND EDGE	0.0	0.100000024
UPPER BAND EDGE	0.020000000	0.500000000
DESIRED VALUE	1.00000000	0.0
WEIGHTING	1.00000000	10.0000000
DEVIATION	0.018813349	0.001881335
DEVIATION IN DB	0.161890686	-54.5106659

The ambiguity response along the Doppler axis for a receiver using this filter is shown in Fig. VI-3. Its sidelobe response (-55 dB) is significantly lower than that for Hamming weighting but at the expense of 4.5 dB S/N loss. This loss is due in part to the fact that negative weights are used to obtain the low sidelobes.

The integrated response of this ambiguity function to the clutter distribution associated with the low altitude satellite example of Section V is shown in Fig. VI-4. The clutter rejection for this distribution of clutter is ~ 60 dB.

Another example of an FIR filter design and associated ambiguity function is given in Table VI-2 and Fig. VI-5. The sidelobes are less than -70 dB but the S/N loss is 7 dB.

6.2 Implementation Considerations

The sample filter designs discussed above indicate that substantial sidelobe reduction and hence clutter rejection is possible but only with significant S/N loss. However, there are several important considerations with regard to the implementation of these designs. The filter design should be optimized for the specific application both with regard to integrated clutter response and S/N loss. Digital signal processing logic needs to be formulated to efficiently provide the desired filtering and target range and Doppler. The stability and accuracy requirements of receiver

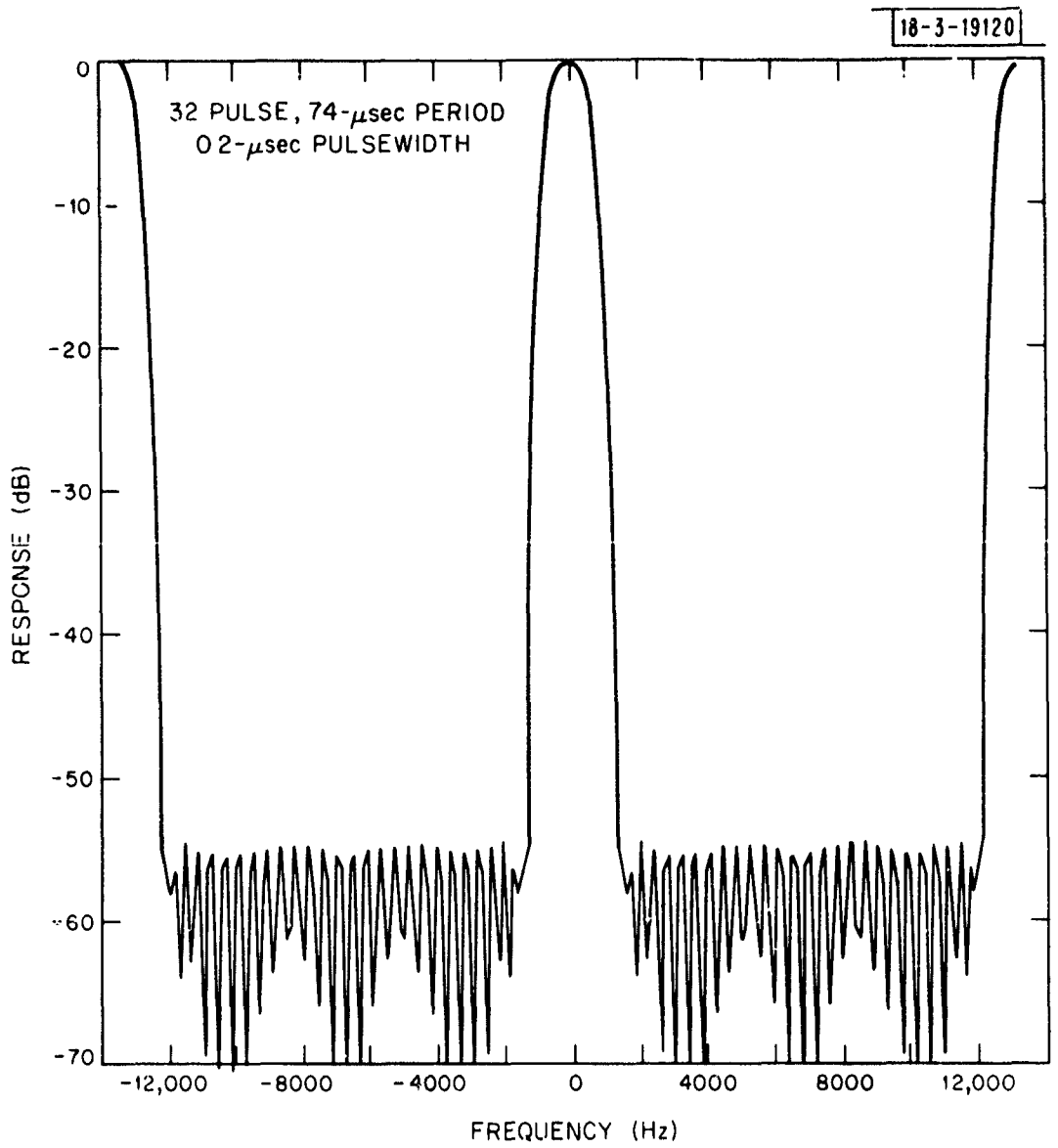


Fig. VI-3. Ambiguity function on doppler axis for weighting of Table VI-1.

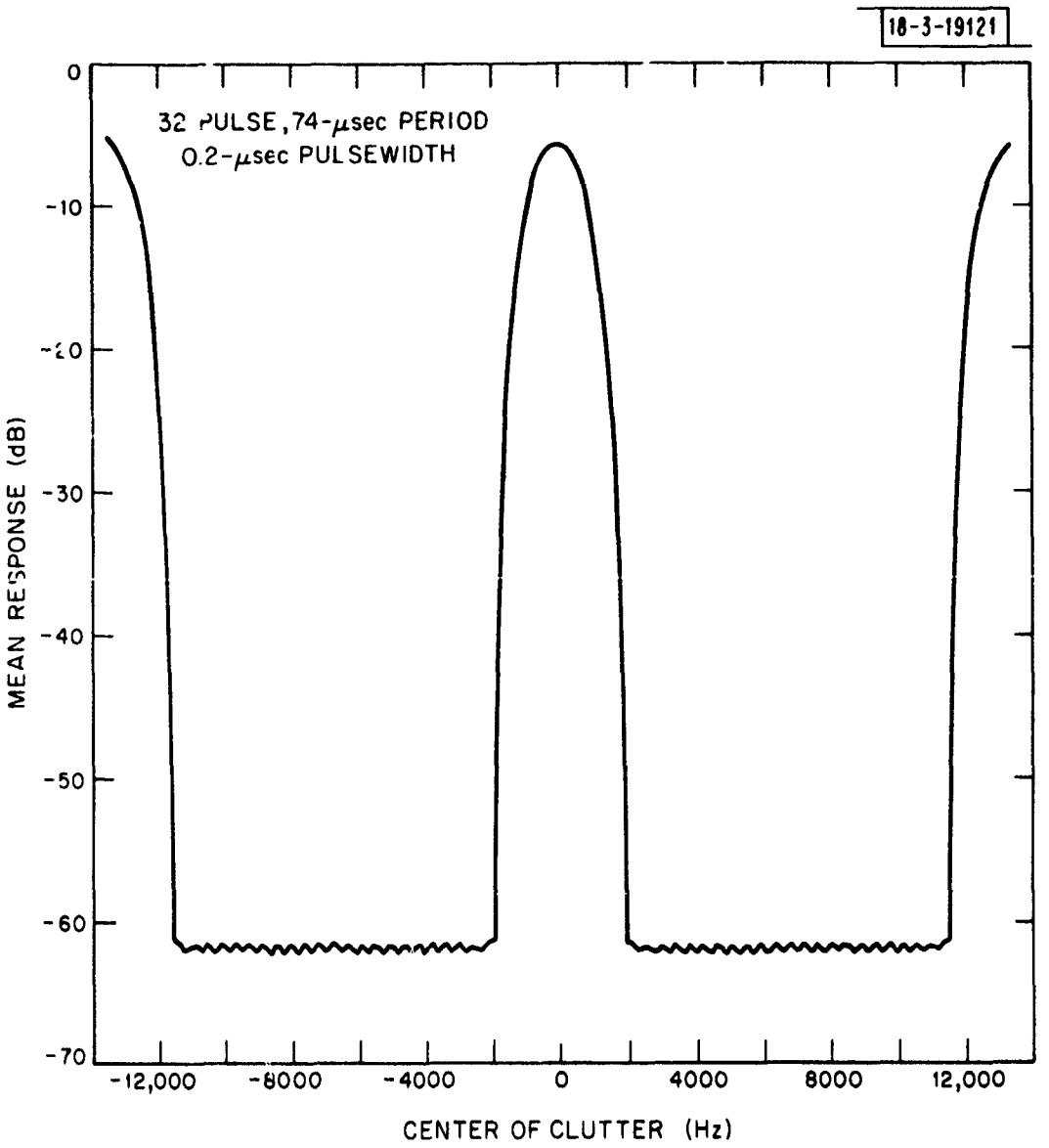


Fig. VI-4. Integrated ambiguity function response to clutter for weighting of Table VI-1.

TABLE VI-2

PULSE WEIGHTING DERIVED FROM DIGITAL FILTER DESIGN:
-70db Sidelobes

FINITE IMPULSE RESPONSE (FIR)
LINEAR PHASE DIGITAL FILTER DESIGN
REMEZ EXCHANGE ALGORITHM

BANDPASS FILTER

FILTER LENGTH = 32

***** IMPULSE RESPONSE *****

H(1) =	0.60465327E-03	= H(32)
H(2) =	0.14172327E-02	= H(31)
H(3) =	0.22057937E-02	= H(30)
H(4) =	0.20479802E-02	= H(29)
H(5) =	-0.16512611E-03	= H(28)
H(6) =	-0.51321425E-02	= H(27)
H(7) =	-0.12332562E-01	= H(26)
H(8) =	-0.19445047E-01	= H(25)
H(9) =	-0.22437945E-01	= H(24)
H(10) =	-0.16578048E-01	= H(23)
H(11) =	0.18148581E-02	= H(22)
H(12) =	0.33475608E-01	= H(21)
H(13) =	0.75001478E-01	= H(20)
H(14) =	0.11904991E+00	= H(19)
H(15) =	0.15610170E+00	= H(18)
H(16) =	0.17729408E+00	= H(17)

	BAND 1	BAND 2
LOWER BAND EDGE	0.0	0.149999976
UPPER BAND EDGE	0.050000001	0.500000000
DESIRED VALUE	1.00000000	0.0
WEIGHTING	1.00000000	50.0000000
DEVIATION	0.014156718	0.000283134
DEVIATION IN DB	0.122098148	-70.9601593

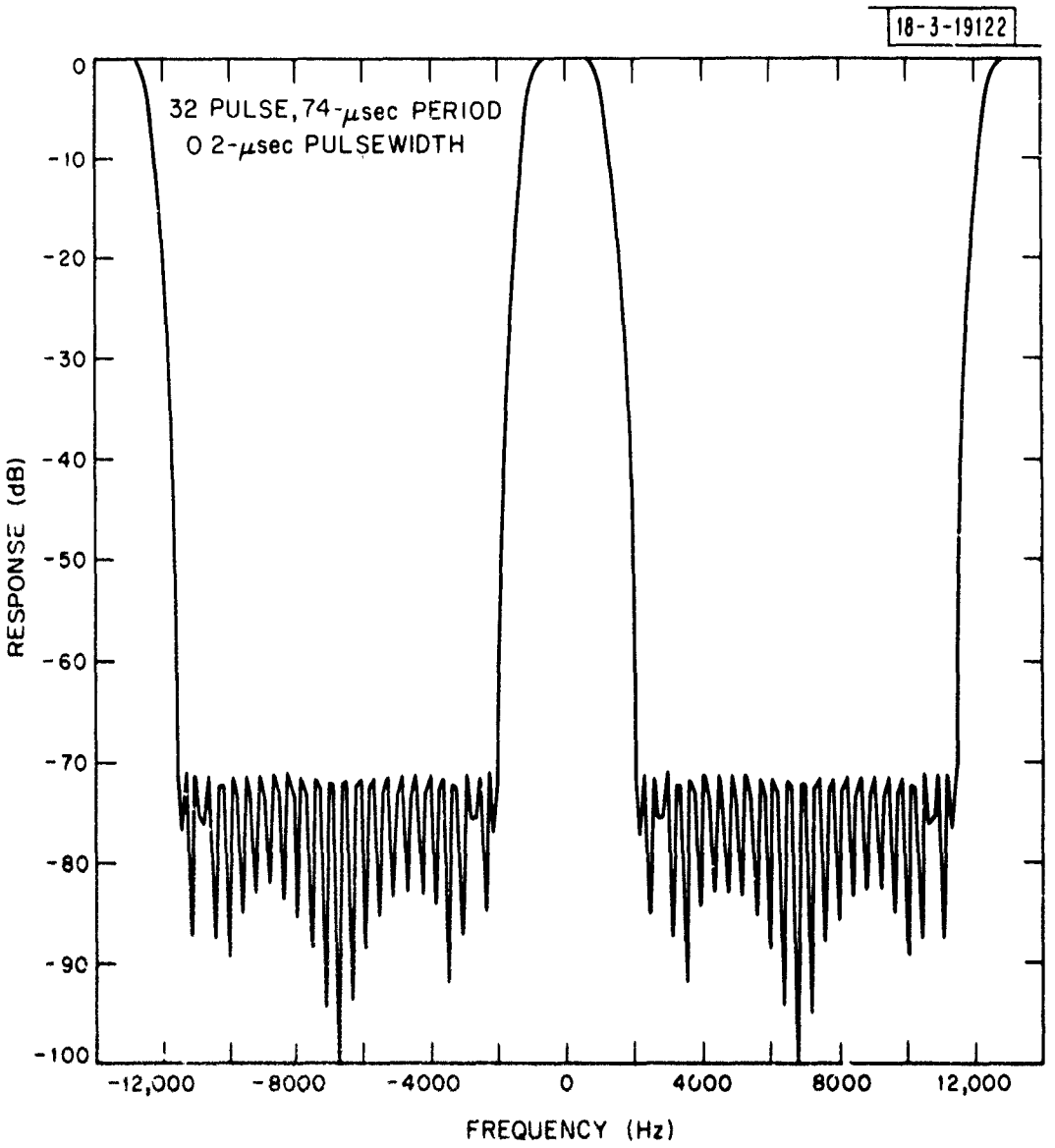


Fig. VI-5. Ambiguity function on doppler axis for weighting of Table VI-2.

hardware preceding the digital processing may be high. These requirements need to be defined and needed hardware developments identified. The possibility of accurately controlled transmitter weighting should not be overlooked. The transmit modules proposed for constructing large planar arrays may accommodate accurate level setting. The high output solid state devices used in these modules contain many parallel sections and the switching of these may be one way to permit accurate, level setting.

VII. SUMMARY AND RECOMMENDATIONS

Satellite-borne bistatic radars can be placed in orbits so that flying aircraft and ground clutter do not overlap in Doppler. Simple waveforms can then be designed which permit detection of the aircraft using Doppler filtering techniques. Mappings of aircraft targets and ground clutter onto the bistatic range-Doppler plane form the basis of waveform design. A Doppler filter capable of the order of 60 dB of clutter rejection is required. Weighting of the waveform and filter to achieve this degree of clutter rejection may result in a loss of several dB in signal-to-noise ratio. Stringent stability and accuracy requirements are imposed on the radar signal system to permit such filters to be used. Weighting on transmit, using level setting in transmit array modules, may be useful as an aid to obtaining required clutter rejection.

Whether the ratio of aircraft cross-section to clutter cross-section is larger for bistatic geometry than for monostatic would have to be determined by measurements. For geometries with large bistatic angles, the bistatic radar must have a significantly larger bandwidth than the monostatic system for the same ground resolution. For maximum clutter reduction the bandwidth should change with viewing geometry changes.

The coverage characteristics of bistatic radars on satellites in representative orbits are described. For some orbits

the bistatic coverage is unique in that it cannot be duplicated by a satellite-borne monostatic radar. For example, portions of a coverage of a bistatic radar can be made equivalent to a monostatic radar fixed in inertial space. The possibility of bistatic range gating of clutter is discussed.

The variation of bistatic viewing angles of an aircraft crossing various portions of a fence may be large so that large variations in cross-section are expected. A complete description of the bistatic cross-section of an aircraft would require extensive measurements.

The principal system requirements of a North American surveillance fence for the detection of bombers are identified for a space-borne bistatic surveillance and tracking radar. Power-aperture products consistent with a 60 meter diameter aperture and 1 kw average power are needed for a geostationary bistatic system.

APPENDIX A

Bistatic $R-\dot{R}$ Maps

In this appendix the derivations of bistatic $R-\dot{R}$ maps and related bistatic parameters are outlined. Both the receiver and transmitter of the bistatic radar are assumed to be on satellites which are on elliptic precessing Keplerian orbits. The bistatic radar observes clutter arising from the surface of a rotating spherical earth. Target aircraft moving above the earth's surface may have horizontal and vertical velocity components relative to the earth and travel at arbitrary headings or along great circle routes. The transmitter and receiver beams may be modeled to have conical or elliptical shapes and two or four monopulse feeds. A highly flexible computer program has been written incorporating these features to obtain bistatic $R-\dot{R}$ maps and other relevant parameters for evaluating bistatic systems.

A.1 Bistatic Range and Range Gradient

Figure A-1 illustrates a satellite-borne bistatic radar observing a point P and defines various vectors in an inertial coordinate system. The vectors needed are:

$\vec{S1}$ - satellite 1 position vector

$\vec{S2}$ - satellite 2 position vector

$\dot{\vec{S1}}$ - satellite 1 velocity vector

$\dot{\vec{S2}}$ - satellite 2 velocity vector

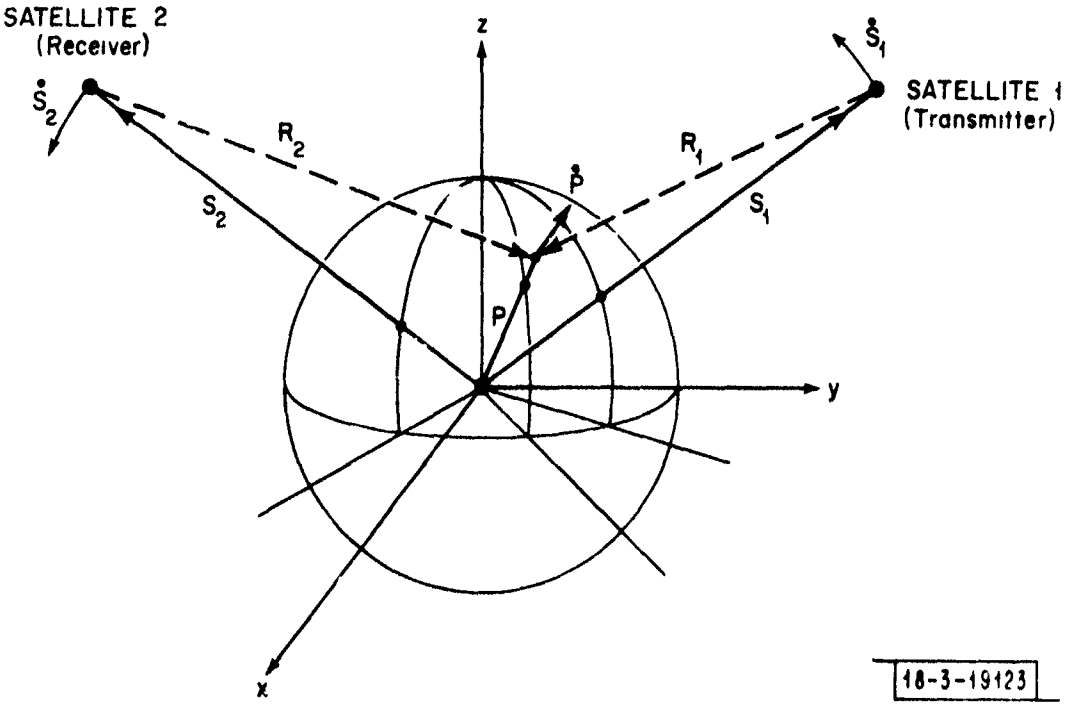


Fig. A-1. Geometry for satellite-borne bistatic radar.

P - observed point position vector

$\dot{P}$ - observed point velocity vector

R1=P-S1 - range vector from S1 to P

R2=P-S2 - range vector from S2 to P

U1=unit vector R1/ $|R1|$

U2=unit vector R2/ $|R2|$

$\underline{i}$, $\underline{j}$, $\underline{k}$ - unit vectors along inertial coordinate axis

The bistatic range is defined as

$$R_B = \frac{|R_1| + |R_2|}{2} = \frac{|P-S1| + |P-S2|}{2}$$

This reduces to the monostatic range when the transmitter and receiver, i.e., the two satellites, are coincident. Consequently this derivation can also be applied to monostatic radars.

The bistatic range gradient or range direction is

$$\nabla R_B = \nabla \left\{ \frac{\sqrt{(P-S1) \cdot (P-S1)} + \sqrt{(P-S2) \cdot (P-S2)}}{2} \right.$$

For any arbitrary point

$$P = \begin{vmatrix} x \\ y \\ z \end{vmatrix}$$

$$\frac{\partial P}{\partial x} = \underline{i}, \quad \frac{\partial P}{\partial y} = \underline{j}, \text{ and } \frac{\partial P}{\partial z} = \underline{k}$$

so that the gradient becomes

$$\nabla R_B = \frac{1}{2}\left[\frac{(P-S1)\cdot \underline{i}}{|R1|}\right] + \left[\frac{(P-S2)\cdot \underline{i}}{|R2|}\right]\underline{i}$$

$$+ \frac{1}{2}\left[\frac{(P-S1)\cdot \underline{j}}{|R1|}\right] + \left[\frac{(P-S2)\cdot \underline{j}}{|R2|}\right]\underline{j}$$

$$+ \frac{1}{2}\left[\frac{(P-S1)\cdot \underline{k}}{|R1|}\right] + \left[\frac{(P-S2)\cdot \underline{k}}{|R2|}\right]\underline{k}$$

Simplifying and combining obtain

$$\nabla R_B = \frac{1}{2}\left[U1_x\underline{i} + U1_y\underline{j} + U1_z\underline{k} + U2_x\underline{i} + U2_y\underline{j} + U2_z\underline{k}\right]$$

$$= \frac{1}{2}\left[U1 + U2\right]$$

Thus the bistatic range direction is along the bisector of the lines-of-sight R1, R2 to the observed points. Normalizing the range gradient gives the unit vector UB along the bistatic range direction,

$$UB = \frac{U1 + U2}{|U1 + U2|}$$

$$= \frac{U1 + U2}{[2(1 + U1 \cdot U2)]^{1/2}}$$

Defining the angle between the line-of-sight vectors as the bistatic angle β, UB becomes

$$UB = \frac{U1 + U2}{2 \cos \beta/2}$$

Bistatic Range Rate and Range Rate Gradient

The bistatic range rate or Doppler is dR_B/dt or

$$\dot{R}_B = \frac{1}{2} \left[(\dot{P} - \dot{S1}) \cdot U1 + (\dot{P} - \dot{S2}) \cdot U2\right] .$$

The bistatic Doppler gradient is

$$\nabla \dot{R}_B = \nabla \left[\frac{(\dot{P}-\dot{S1}) \cdot U1 + (\dot{P}-\dot{S2}) \cdot U2}{2}\right]$$

$$= \frac{1}{2} \left[\frac{\partial \dot{P}}{\partial x} \cdot U1 + \frac{\partial \dot{P}}{\partial x} \cdot U2 + (\dot{P}-\dot{S1}) \cdot \frac{dU1}{\partial x} + (\dot{P}-\dot{S2}) \cdot \frac{dU2}{\partial x}\right] \underline{i}$$

$$+ \frac{1}{2} \left[\frac{\partial \dot{P}}{\partial y} \cdot U1 + \frac{\partial \dot{P}}{\partial y} \cdot U2 + (\dot{P}-\dot{S1}) \cdot \frac{dU1}{\partial y} + (\dot{P}-\dot{S2}) \cdot \frac{dU2}{\partial y}\right] \underline{j}$$

$$+ \frac{1}{2} \left[\frac{\partial \dot{P}}{\partial z} \cdot U1 + \frac{\partial \dot{P}}{\partial z} \cdot U2 + (\dot{P}-\dot{S1}) \cdot \frac{dU1}{\partial z} + (\dot{P}-\dot{S2}) \cdot \frac{dU2}{\partial z}\right] \underline{k}$$

From the definitions of U1 and U2, obtain

$$\frac{\partial U1}{\partial x} = \frac{1}{|R1|}\left[\frac{\partial P}{\partial x} - U1\ (U1 \cdot \frac{\partial P}{\partial x})\right] .$$

Similar terms are obtained for $\frac{\partial U1}{\partial y}$, $\frac{\partial U1}{\partial z}$ and for the partials of U2. For an arbitrary point P rotating with the earth

$$P = \begin{vmatrix} x \\ y \\ z \end{vmatrix}$$

and

$$\dot{P} = \omega_e \begin{vmatrix} -y \\ x \\ 0 \end{vmatrix}$$

where ω_e is the earth rate. The partials of P were given earlier. The partial of $\dot{P}$ is

$$\frac{\partial \dot{P}}{\partial x} = \omega_e \underline{j} \ ; \ \frac{\partial \dot{P}}{\partial y} = -\omega_e \underline{i} \ ; \ \frac{\partial \dot{P}}{\partial z} = 0 .$$

Substitution into the appropriate terms above completes the determination of $\nabla \dot{R}_B$ at any observed point.

A.2 Bistatic Angles

The cross-section of an object generally depends on the viewing geometry. For a bistatic radar there are three parameters required to describe the cross-section of an axi-symmetric body and four parameters for a body with symmetry in each of two orthogonal planes as is approximated by an aircraft. (A horizontally flying aircraft has a horizontal and vertical plane of symmetry.) The intersection of these symmetry planes defines the body axis. Figure A-2 defines the bistatic angle, bistatic aspect and bistatic pitch of an axi-symmetric body. For a body like an aircraft the fourth parameter is the bistatic roll. The bistatic roll is the angle between the bistatic pitch plane and the normal to the "horizontal" symmetry plane of the body. It is positive in the sense of a right hand screw along the body axis. Figure A-3 illustrates the bistatic roll angle.

The bistatic angles describing the viewing geometry of areas (such as portions of the earth surface) can be found by treating the surface as an axi-symmetric body where the surface normal corresponds to the body axis.

A.3 Clutter Density in the $\dot{R}$-$\dot{R}$ Plane

The mapping of points on the earth's surface onto the $\dot{R}$-$\dot{R}$ plane has been described above. However, clutter cross-section is area dependent so that the clutter density in the $\dot{R}$-$\dot{R}$ plane must

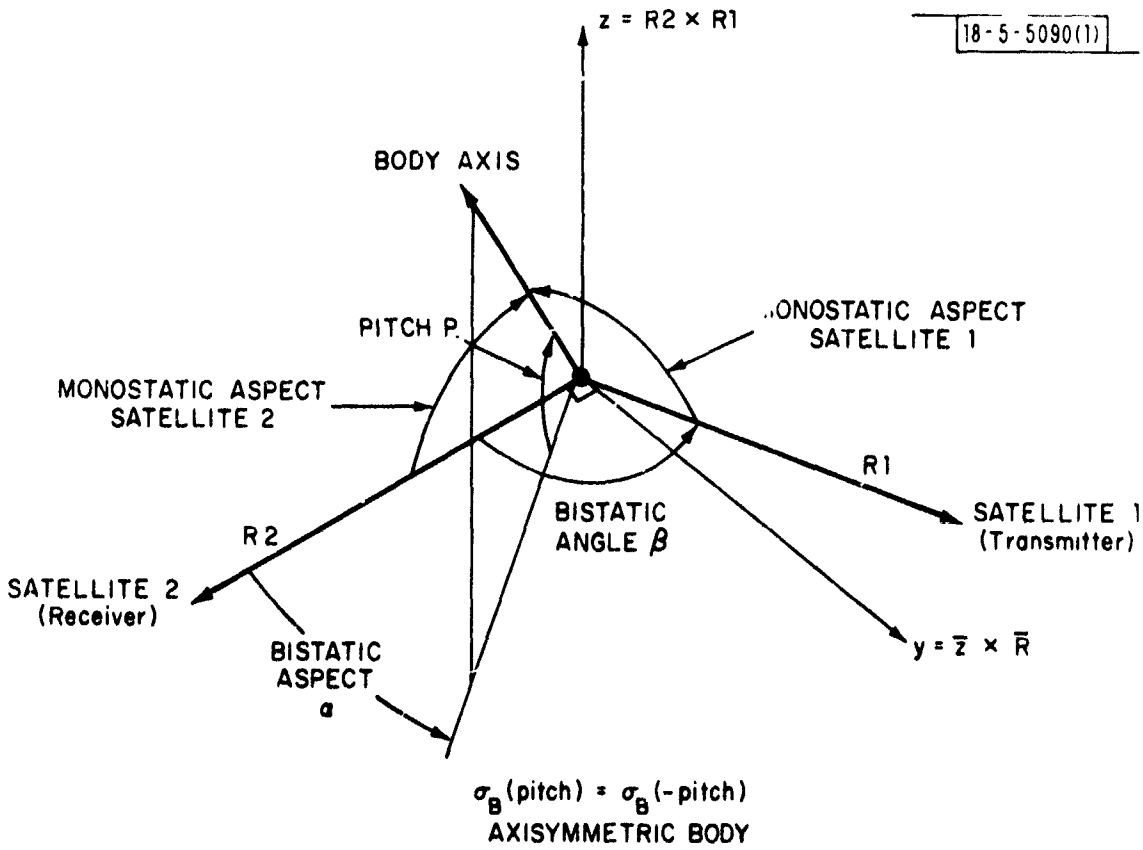


Fig. A-2. Angles for determining bistatic cross section.

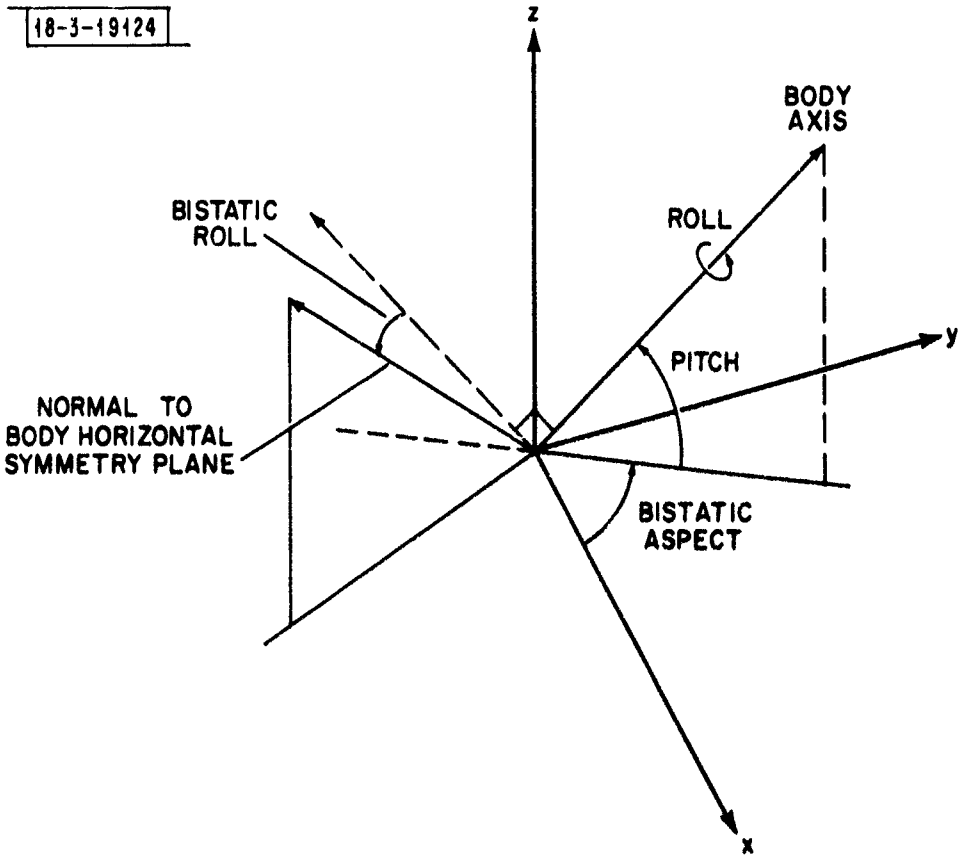


Fig. A-3. Bistatic roll angle.

be obtained by scaling elemental areas. This scaling is determined by the Jacobian of the transformation into the R-$\dot{R}$ plane.

The clutter cross-section is an elemental area given by

$$d\sigma = \sigma^{o}_{B} dA$$

where σ^{o}_{B} is the bistatic cross-section density and dA the elemental area tangent to the earth's surface. Expressed in terms of an elemental area in the R-$\dot{R}$ plane it is

$$d\sigma = \sigma^{o}_{B} J dR d\dot{R}$$

where, for example, dR and $d\dot{R}$ may be approximated by the range and Doppler resolution of the radar. J is the Jacobian of the transformation of dA to dR $d\dot{R}$. Therefore, the bistatic clutter density in the R-$\dot{R}$ plane becomes

$$\sigma^{o}_{BR\dot{R}} = \frac{d\sigma}{dR\, d\dot{R}} = J\, \sigma^{o}_{B} .$$

The Jacobian J is determined below from two factors: the Jacobian of the transformation from x,y to latitude, longitude coordinates; and the Jacobian of the transformation from latitude, longitude to R-$\dot{R}$ coordinates. The first Jacobian is usually found by simpler more direct means, but the more general method is used here to

illustrate that method with a familiar case and for consistency with the determination of the second factor.

The area dA can be expressed as

$$dA = dxdy$$

where x and y are related to the latitude (lat) and longitude (long) of the area dA, and the earth radius R_e according to

$$x = R_e \, lat$$

$$y = R_e \cos (lat) \, long \, .$$

The Jacobian of this transformation is

$$J_{xyLL} = DET \begin{vmatrix} \frac{\partial x}{\partial lat} & \frac{\partial x}{\partial long} \\ \frac{\partial y}{\partial lat} & \frac{\partial y}{\partial long} \end{vmatrix} \equiv \frac{\partial (x,y)}{\partial (lat,long)}$$

where DET indicates "determinant of", so that

$$J_{xyLL} = R_e^{\,2} \cos (lat)$$

and

$$dxdy = J_{xyLL}\, dlat\, dlong \quad .$$

Therefore in the lat, long coordinates

$$dA = R_e^2 \cos(lat)\, dlat\, dlong \ ,$$

the familiar result.

The mapping of clutter onto the R-$\dot{R}$ plane depends on the position and velocity of the mapped point, both of which are determined by the latitude and longitude of the point. All other parameters of the transformation are independent of latitude and longitude. The transformation can be represented by

$$R = R(lat, long)$$

$$\dot{R} = \dot{R}(lat, long)$$

where the subscript B, denoting a bistatic system, is dropped for compactness of notation. The Jacobian of this transformation is

$$J_{R\dot{R}LL} = \frac{\partial(R, \dot{R})}{\partial(lat, long)}$$

and relates dlat dlong and $dR\ \dot{dR}$ according to

$$dR\dot{dR} = \frac{1}{J_{R\dot{R}LL}}\ dlat\ dlong = J_{LL\dot{R}R}\ dlat\ dlong\ .$$

The Jacobian

$$J_{\dot{R}RLL} = DET \begin{vmatrix} \frac{\partial R}{\partial lat} & \frac{\partial R}{\partial long} \\ \frac{\partial \dot{R}}{\partial lat} & \frac{\partial \dot{R}}{\partial long} \end{vmatrix}$$

is evaluated below.

Partials of R are found from

$$\frac{\partial R}{\partial lat} = \frac{1}{2}\left[\frac{\partial |R1|}{\partial\ lat} + \frac{\partial |R2|}{\partial\ lat}\right]\ ,\quad \frac{\partial R}{\partial long} = \frac{1}{2}\left[\frac{\partial |R1|}{\partial long} \quad \frac{\partial |R2|}{\partial long}\right]$$

$$\frac{\partial |R1|}{\partial\ lat} = U1 \cdot \frac{\partial R1}{\partial lat}\ ,\qquad \frac{\partial |R2|}{\partial lat} = U2 \cdot \frac{\partial R2}{\partial lat}$$

$$\frac{\partial |R1|}{\partial long} = U1 \cdot \frac{\partial R1}{\partial long}\ ,\qquad \frac{\partial |R2|}{\partial long} = U2 \cdot \frac{\partial R2}{\partial long}\ .$$

$$\frac{\partial R1}{\partial lat} = \frac{\partial R2}{\partial lat} = \frac{\partial P}{\partial lat} = R_e \begin{vmatrix} -\sin lat \cos (long + \omega_e t) \\ -\sin lat \sin (long + \omega_e t) \\ \cos lat \end{vmatrix}$$

$$\frac{\partial R1}{\partial long} = \frac{\partial R2}{\partial long} = \frac{\partial P}{\partial long} = R_e \begin{vmatrix} -\cos lat \sin (long + \omega_e t) \\ \cos lat \cos (long + \omega_e t) \\ 0 \end{vmatrix}$$

where t is the time.

The partials of $\dot{R}$ are found from

$$\frac{\partial \dot{R}}{\partial lat} = \frac{1}{2}\left[(\dot{P}-\dot{S}1)\cdot\frac{\partial U1}{\partial lat} + \frac{\partial \dot{P}}{\partial lat}\cdot U1 + (\dot{P}-\dot{S}2)\cdot\frac{\partial U2}{\partial lat} + \frac{\partial \dot{P}}{\partial lat}\cdot U2\right]$$

$$\frac{\partial \dot{R}}{\partial long} = \frac{1}{2}\left[(\dot{P}-\dot{S}1)\cdot\frac{\partial U1}{\partial long} + \frac{\partial \dot{P}}{\partial long}\cdot U1 + (\dot{P}-\dot{S}2)\cdot\frac{\partial U2}{\partial long} + \frac{\partial \dot{P}}{\partial long}\cdot U2\right]$$

$$\frac{\partial U1}{\partial lat} = \frac{|R1|\frac{\partial R1}{\partial lat} - R1\frac{\partial |R1|}{\partial lat}}{|R1|^2}, \quad \frac{\partial U2}{\partial lat} = \frac{|R2|\frac{\partial R2}{\partial lat} - R2\frac{\partial R2}{\partial lat}}{|R2|}$$

$$\frac{\partial U1}{\partial long} = \frac{|R1|\frac{\partial R1}{\partial long} - R1\frac{\partial |R1|}{\partial long}}{|R1|^2}, \quad \frac{\partial U2}{\partial long} = \frac{|R2|\frac{\partial R2}{\partial long} - R2\frac{\partial R2}{\partial long}}{|R2|}$$

where the partials of $|R1|$, $|R2|$, R1 and R2 are given above.

Partials of $\dot{P}$ are found from

$$\dot{P} = \omega_e R_e \cos lat \begin{vmatrix} -\sin (long + \omega_e t) \\ \cos (long + \omega_e t) \\ 0 \end{vmatrix}$$

$$\frac{\partial \dot{P}}{\partial lat} = -\omega_e R_e \sin lat \begin{vmatrix} -\sin (long + \omega_e t) \\ \cos (long + \omega_e t) \\ 0 \end{vmatrix}$$

$$\frac{\partial \dot{P}}{\partial long} = -\omega_e R_e \cos lat \begin{vmatrix} \cos (long + \omega_e t) \\ \sin (long + \omega_e t) \\ 0 \end{vmatrix}$$

The substitution of the partials determined above into $J_{\dot{R}RLL}$ completes its determination. Combining $J_{\dot{R}RLL}$ with J_{xyLL} determines J and the clutter density in the R-$\dot{R}$ plane, thus

$$J = J_{xyLL}/J_{\dot{R}RLL} = J_{xyLL}\, J_{LL\dot{R}R}$$

so that

$$\sigma^o{}_{B\dot{R}R} = \sigma^o\, J_{xyLL}\, J_{LL\dot{R}R}$$

and the relative density is

$$\sigma'_R = \frac{\sigma^o{}_{B\dot{R}R}}{\sigma^o} = J_{xyLL}\, J_{LL\dot{R}R}$$

An alternative relative R-$\dot{R}$ density results when the cross-section density γ_B relative to a projected area is used

rather than σ^o_B. Thus

$$\sigma^o_B = \gamma_B \cos \phi$$

where ϕ is the angle of incidence of the bistatic range vector. The relative bistatic density in the R-$\dot{R}$ plane is then

$$\sigma_R = \frac{\sigma^o_{BR\dot{R}}}{\gamma_B} = \cos \phi \, J_{xyLL} \, J_{LL\dot{R}\dot{R}}$$

and differs from that initially derived by only the $\cos \phi$. This last form is used in this report. Notice that the dimension of σ_r is seconds.

A.4 Example Mappings onto the R-$\dot{R}$ Plane

To illustrate various R-$\dot{R}$ maps the bistatic radar on the high altitude satellites example in Section V is used. These satellites are on elliptic, 12 hour orbits such that their angular rate at apogee matches that of the earth. The clutter maps are obtained by mapping a 5^o longitude by 1^o latitude grid of points on the surveillance fence (Fig. V-10) into the R-$\dot{R}$ plane for the satellites 1 and 3 hours past apogee. Aircraft at each grid point with an altitude of 10 km and moving horizontally at 0.3 km/s on a heading of 180 degrees are also mapped into the R-$\dot{R}$ plane. Because clutter or aircraft at different portions of the fence

may have the samr range and Doppler as clutter or aircraft in other portions, there is folding of the maps in the R-R plane. To simplify the presentation of the R-R maps they have been divided into two sections (A and B) in which there is little or no folding. The clutter maps are given in Figs. A-4, 6, 8 and 10 and the corresponding aircraft maps in Figs. A-5, 7, 9 and 11. Nine points on the surveillance fence have been labeled as indicated in Fig. V-10 to provide reference locations on the $\dot{R}$-$\dot{R}$ maps.

Figures A-12 and 13 show the bistatic relative cross-section density at the grid points of the fence when the satellites are 1 hour past apogee. The regions of large cross-section density indicate regions where the Doppler spread within the beam will be small. For small beams where the clutter density is constant within the beam, the clutter cross-section in a clutter filled $\dot{R}$-$\dot{R}$ cell or within the entire beam can be directly found from the density plots and the resolution cell or beam $\dot{R}$-$\dot{R}$ map.

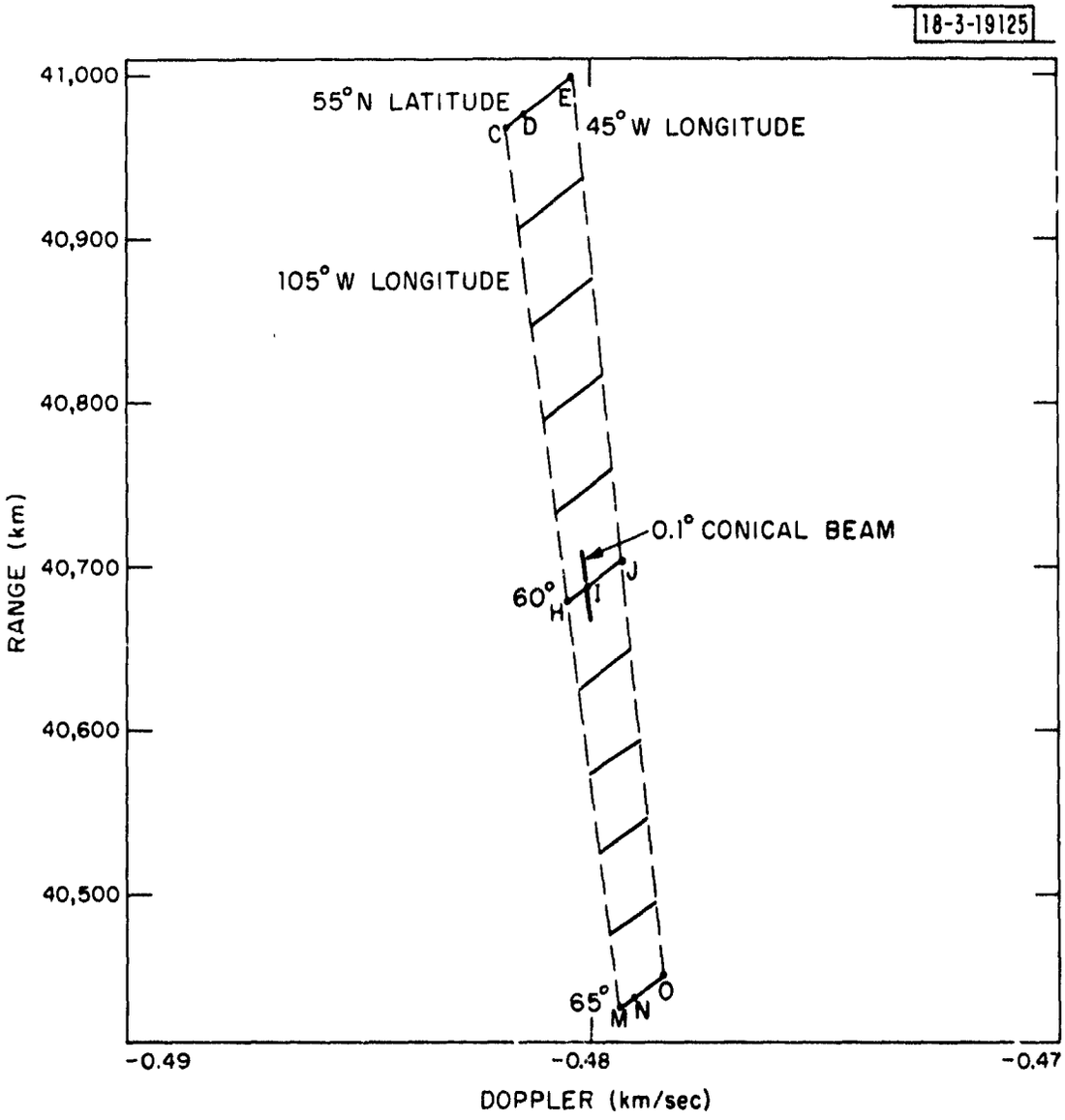


Fig. A-4. Clutter map of portion "A" of surveillance fence: t = 1 hr.

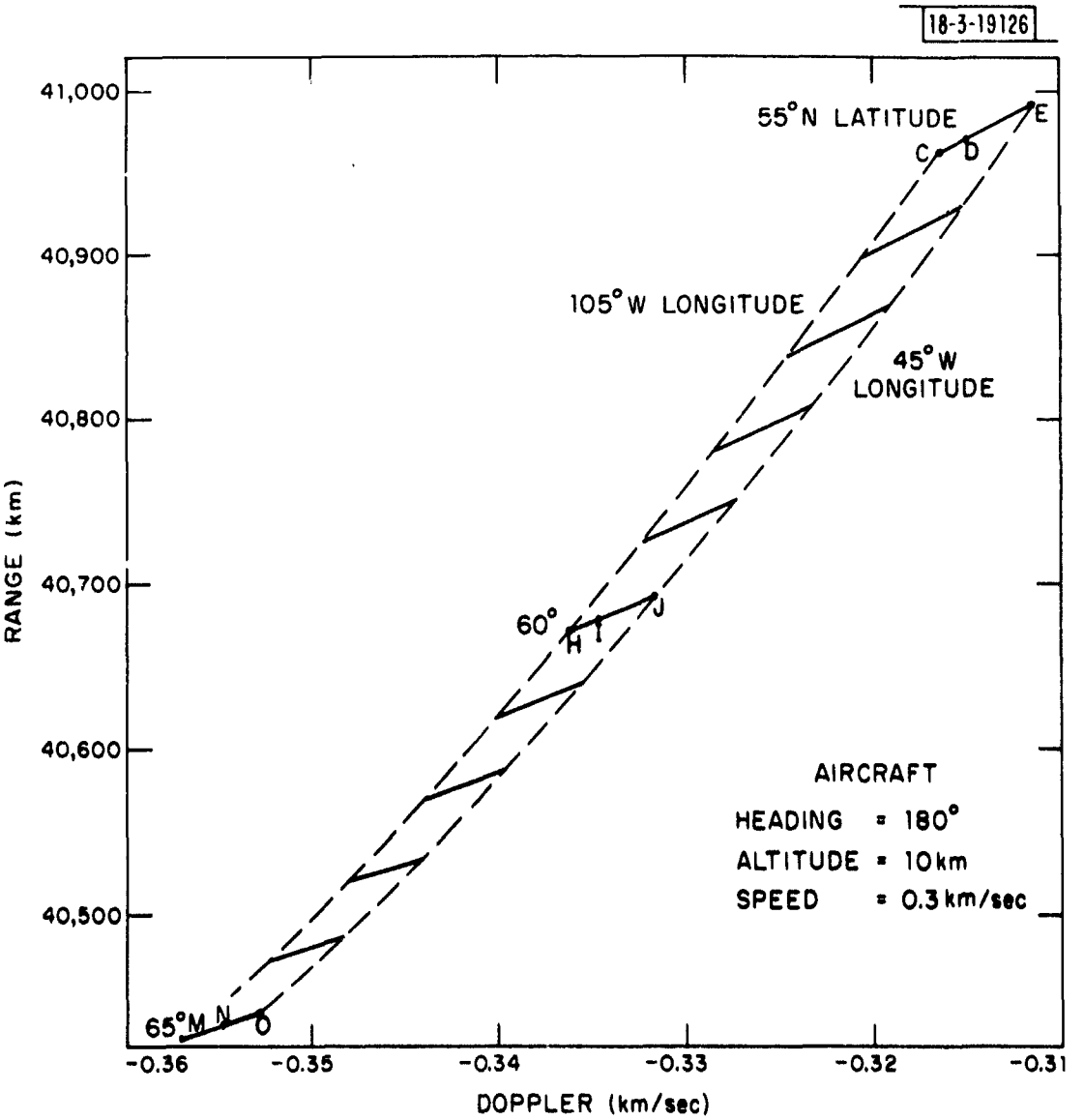


Fig. A-5. Aircraft in portion "A" of surveillance fence: t = 1 hr.

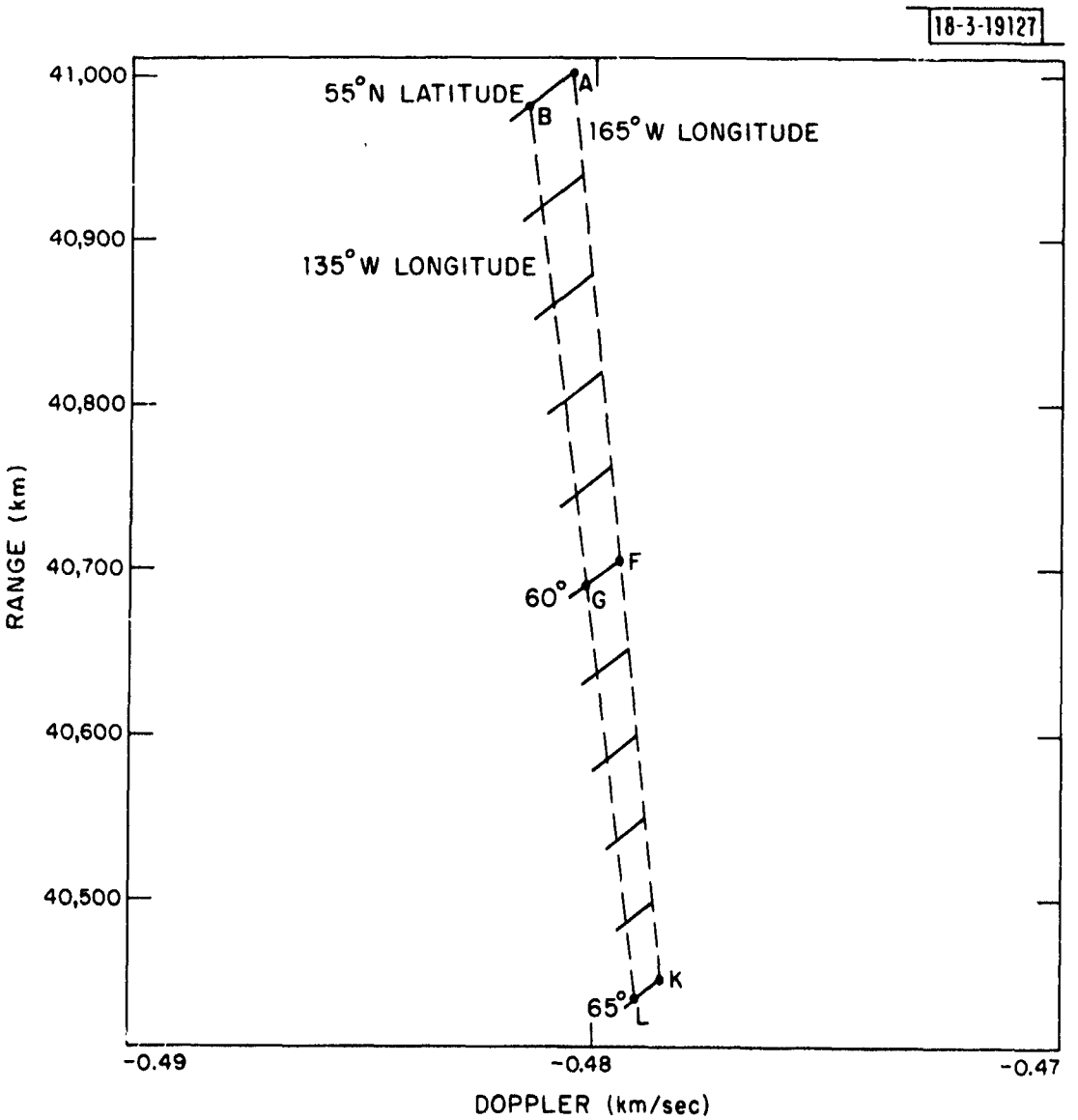


Fig. A-6. Clutter map of portion "B" of surveillance fence: t = 1 hr.

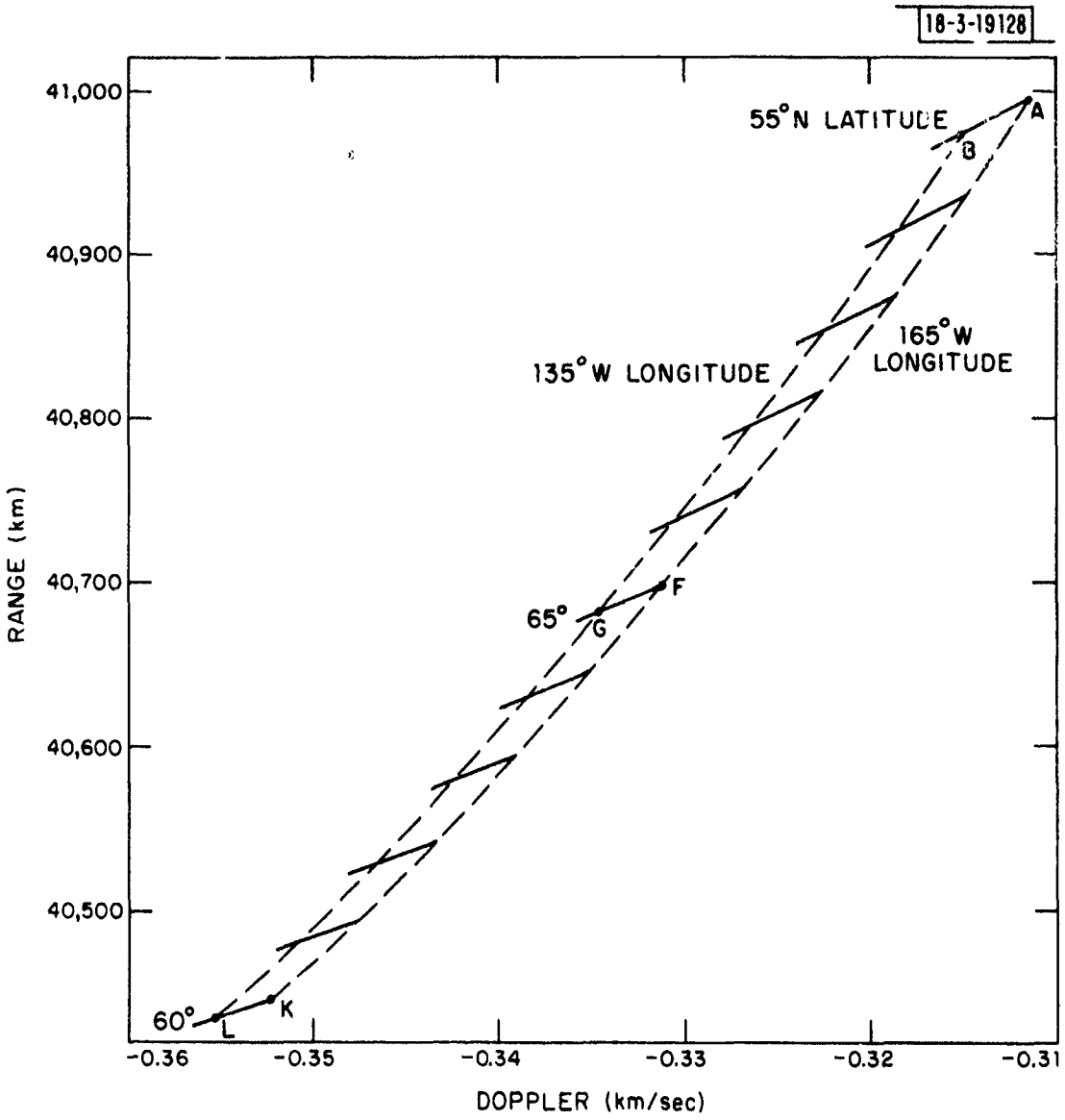


Fig. A-7. Aircraft in portion "B" of surveillance fence: t = 1 hr.

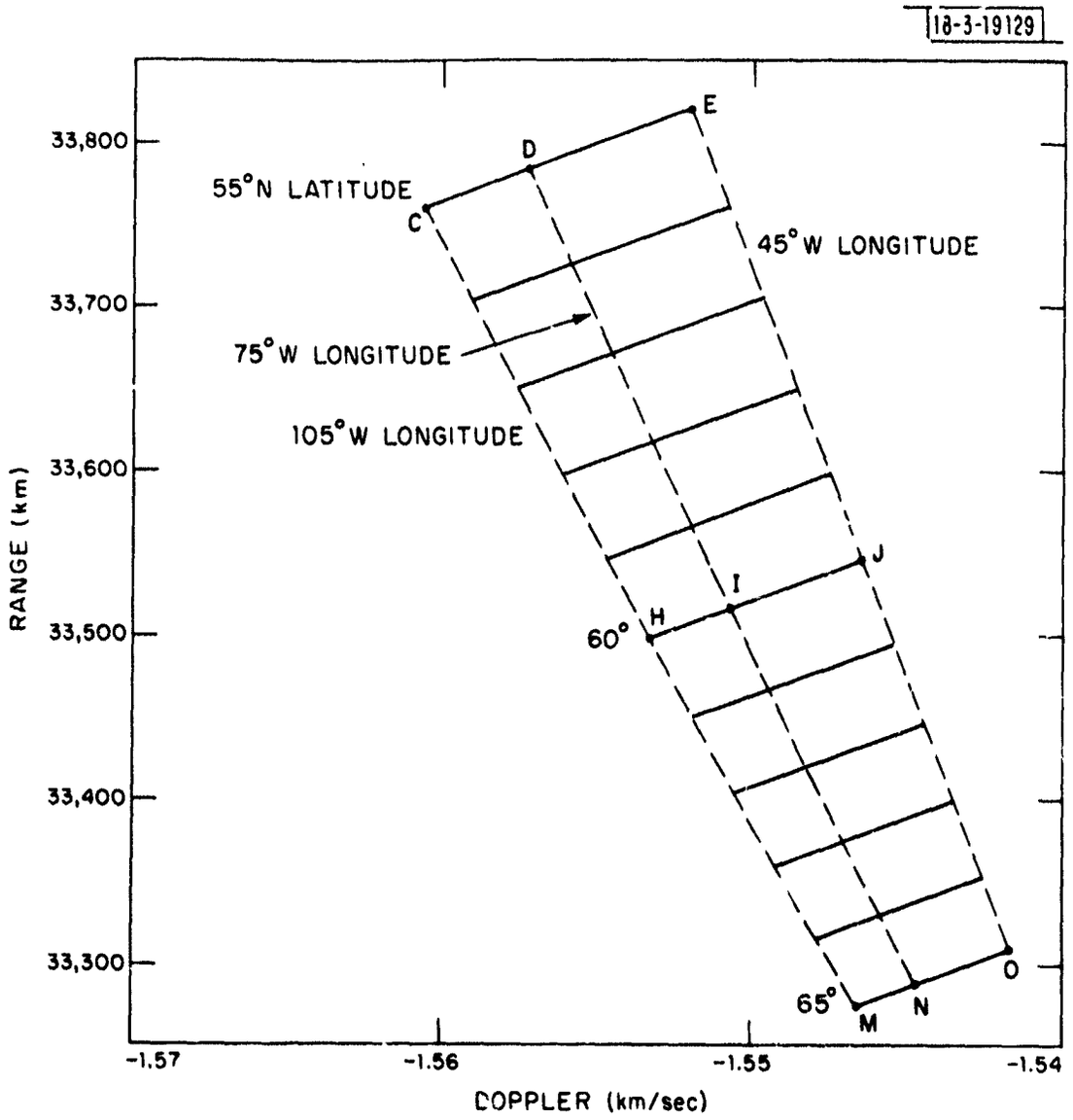


Fig. A-8. Clutter map of portion "A" of surveillance fence: t = 3 hr.

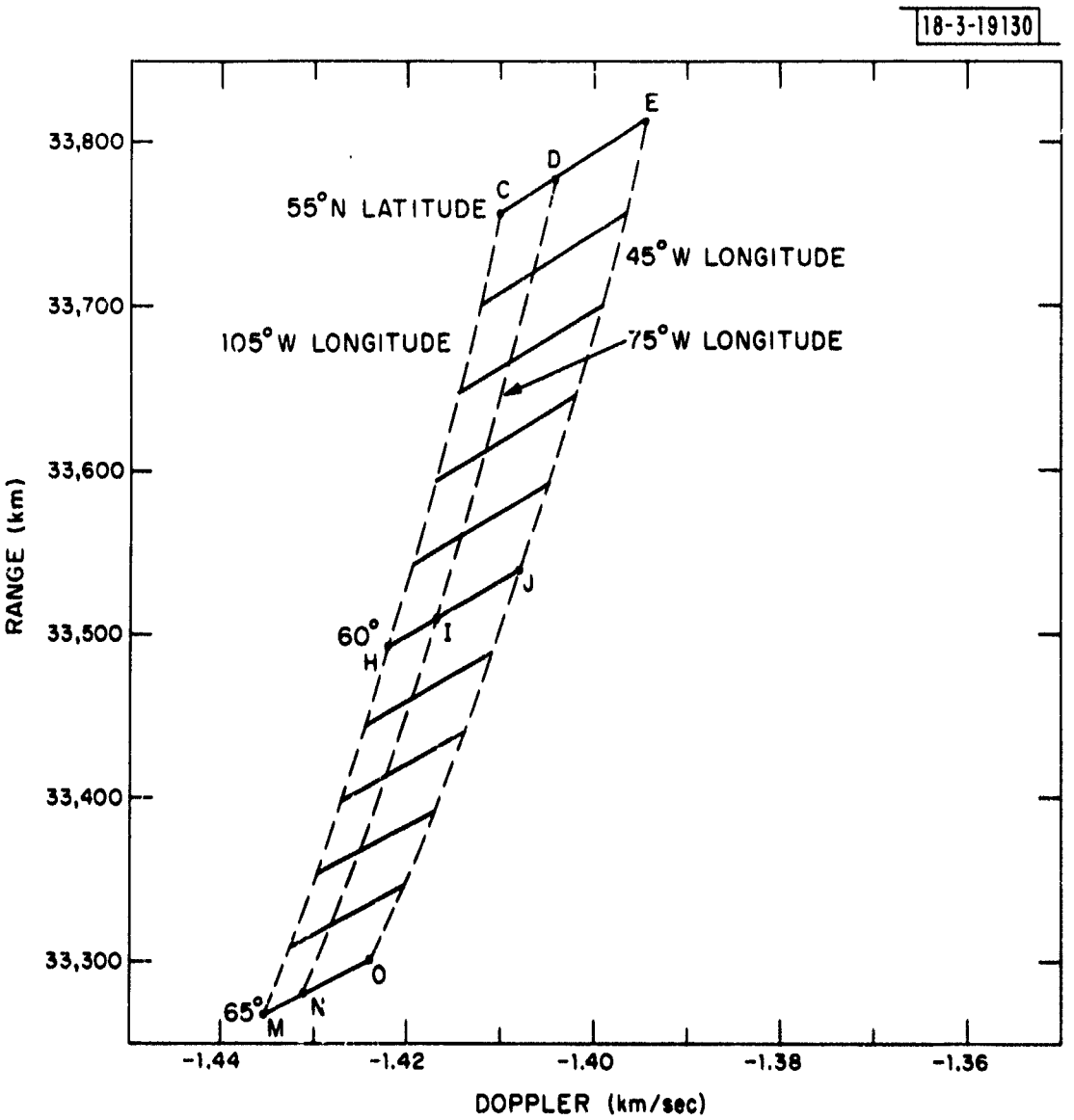


Fig. A-9. Aircraft in portion "A" of surveillance fence: t = 3 hr.

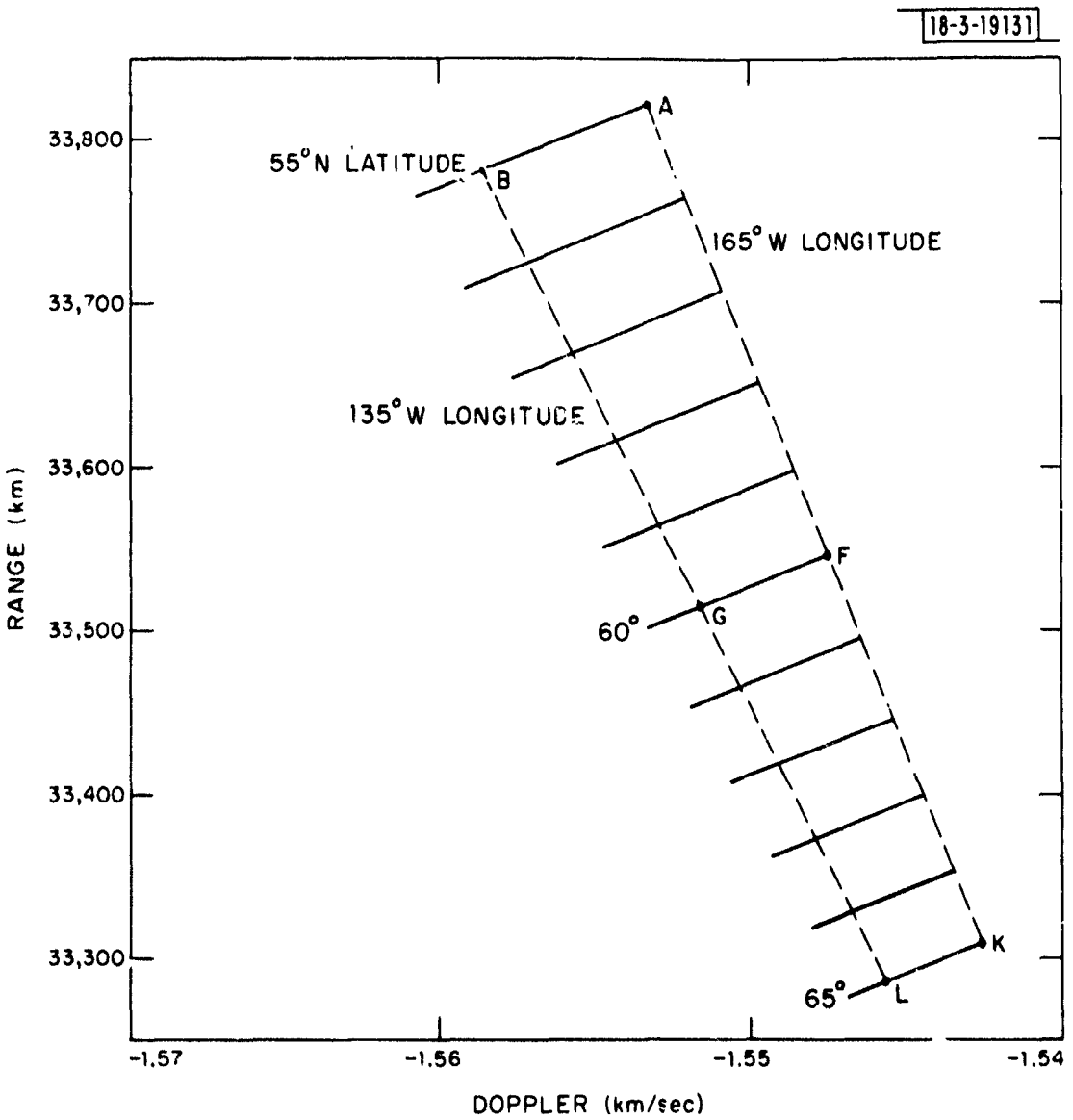


Fig. A-10. Clutter map of portion "B" of surveillance fence: t = 3 hr.

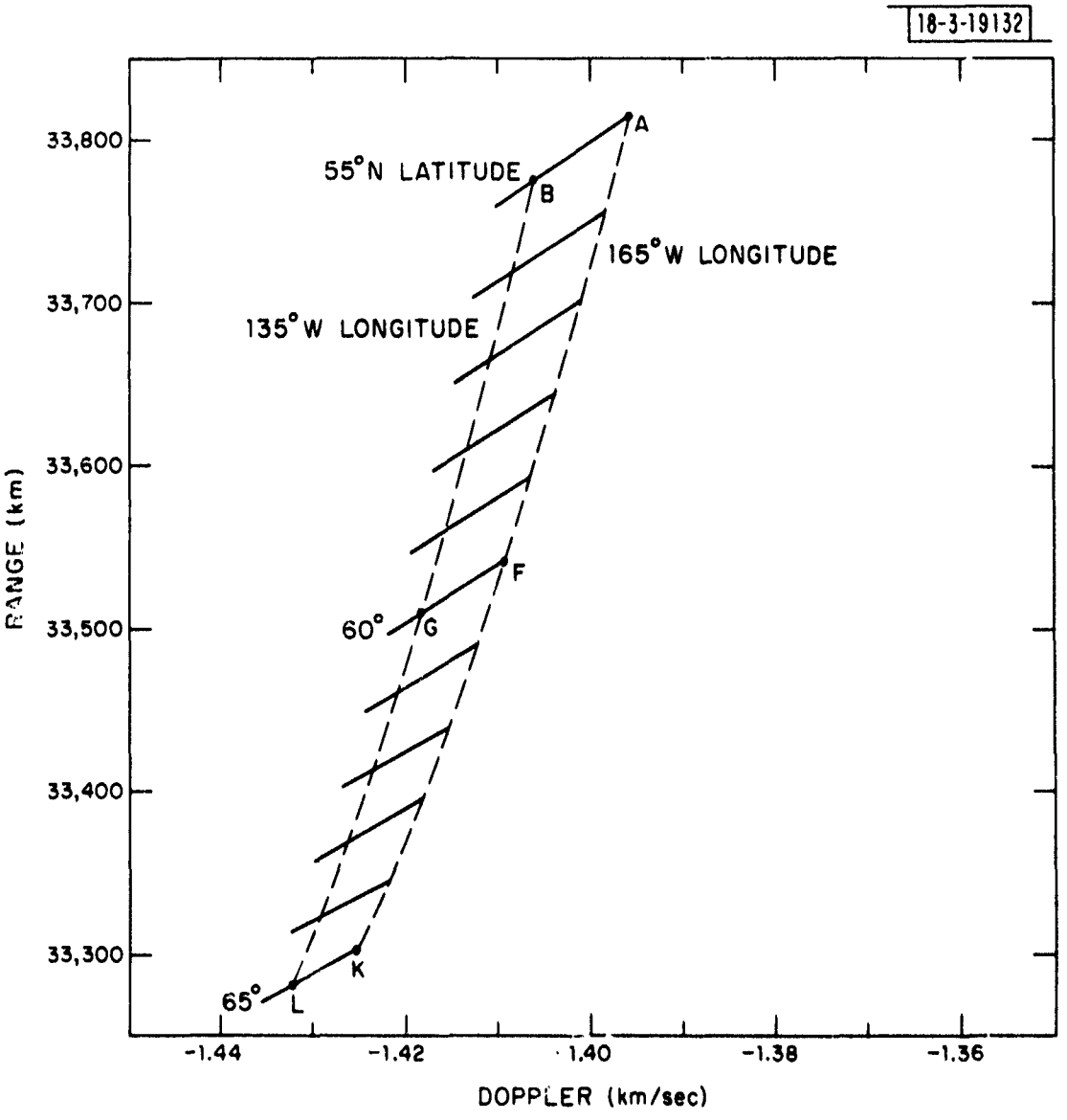


Fig. A-11. Aircraft in portion "B" of surveillance fence: t = 3 hr.

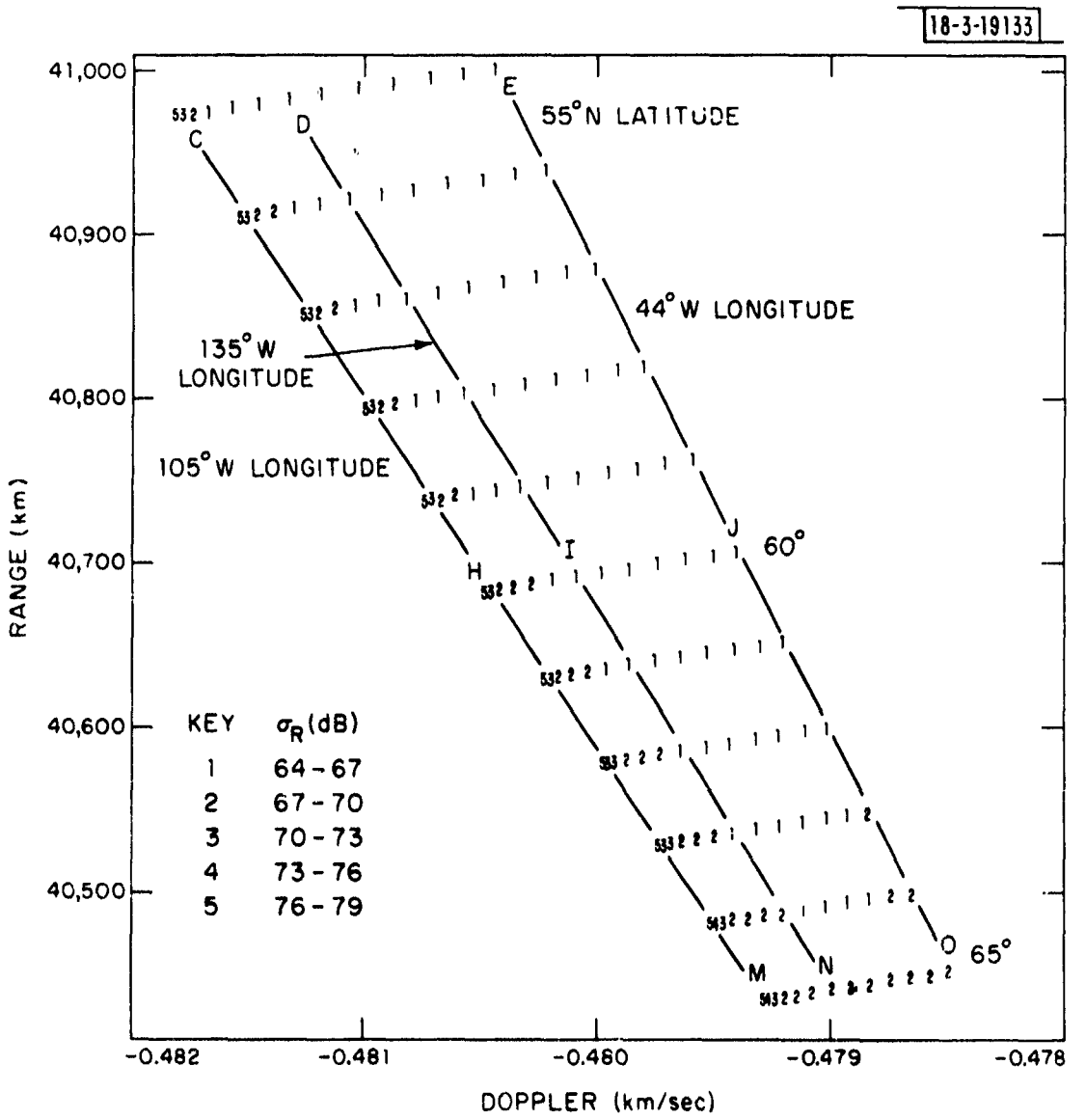


Fig. A-12. Clutter density for portion "A" of surveillance fence: t = 1 hr.

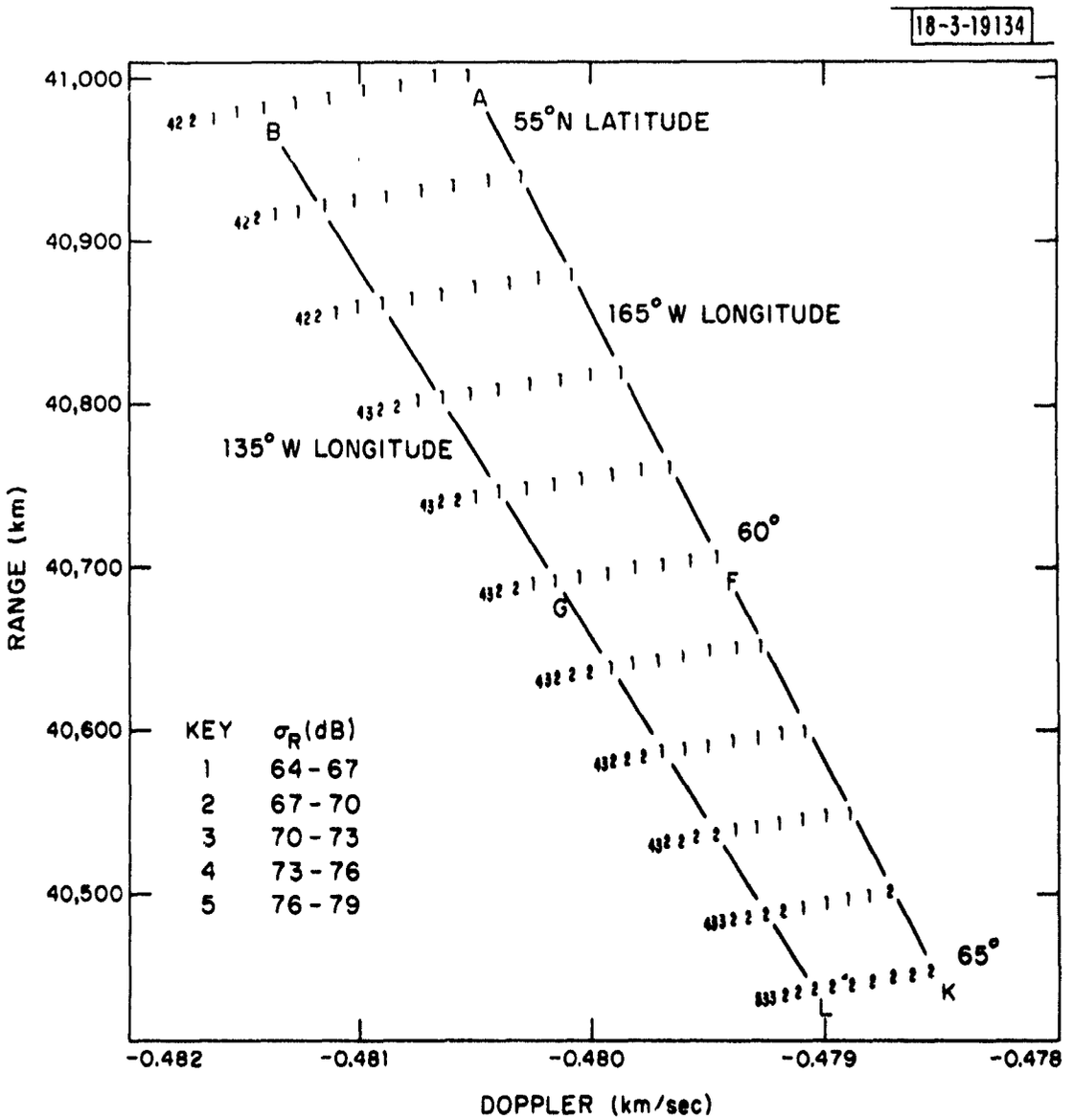


Fig. A-13. Clutter density for portion "B" of surveillance fence: t = 1 hr.

APPENDIX B

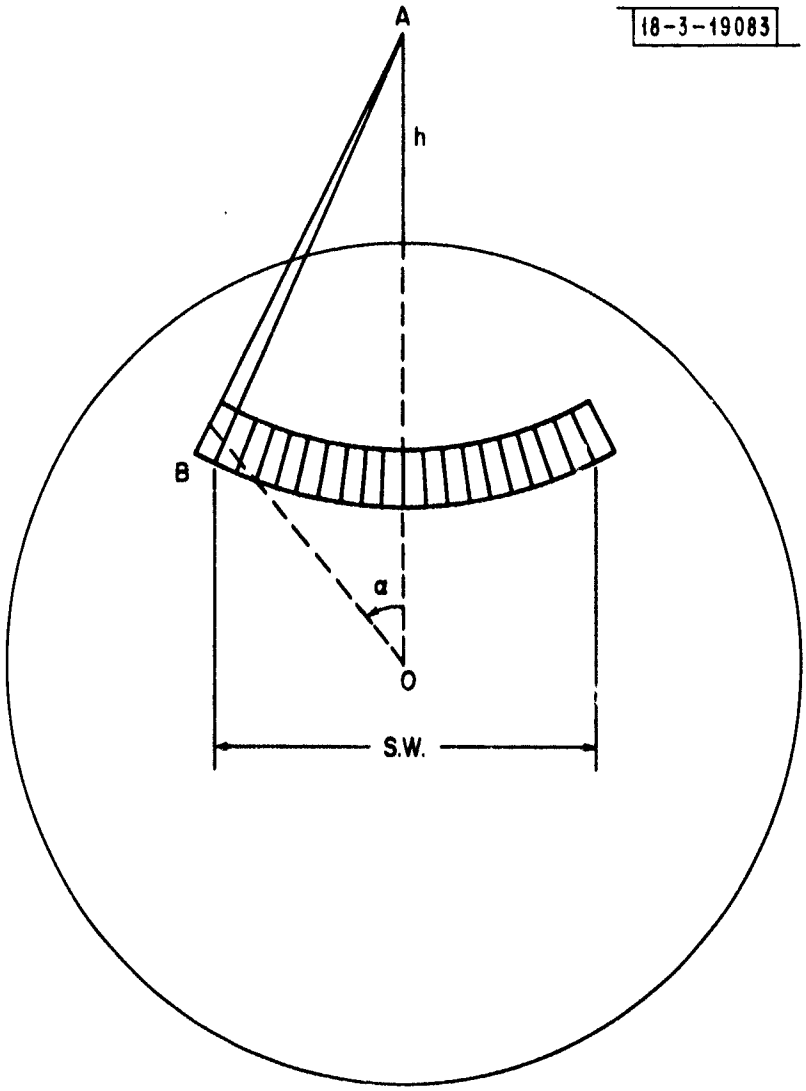
Range Gating Ground Clutter in a Monostatic Satellite-Borne Radar

In this appendix we investigate a well known technique for eliminating ground clutter in the main lobe of a space-borne radar viewing targets against the background of the earth. The technique is to utilize range separation between the target and the clutter in the beam. The range separation between ground clutter and target is investigated as a function of antenna beam-width, sensor scan angle, depression angle, satellite altitude, target altitude and ground swath coverage.

B.1 Geometry

The sensor is carried in a satellite in some orbit and is allowed to scan either side of the orbital plane. The scan pattern lies on a surface of a cone whose axis goes through the center of the earth and the satellite. This geometry gives a constant range to the ground clutter for a specific half cone angle. The geometry is shown in Fig. B-1. The velocity vector of the satellite is normal to the plane of Fig. B-1.

The target will be at some altitude which is different than the altitude of the satellite. Figure B-2 shows the plane AOB and defines the terminology of various angles referred to in this note. All angles are measured to the center of the antenna beamwidth.



h = SATELLITE ALTITUDE

S.W. = SWATH WIDTH (on surface of the earth)

O = CENTER OF THE EARTH

α = EARTH CENTRAL ANGLE

Fig. B-1. Satellite viewing geometry.

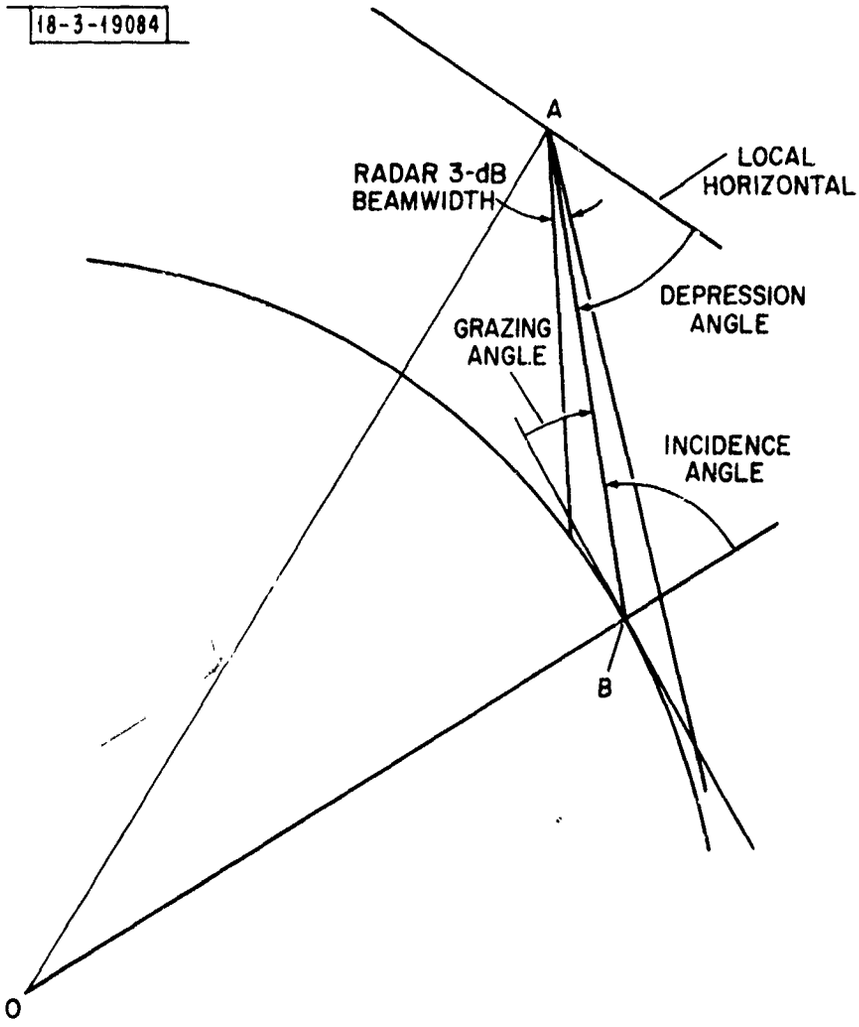


Fig. B-2. Definition of angles.

The ground clutter returns will be spread over a range interval defined by the intersection of the antenna beamwidth and the earth. Figure B-3 is an amplitude versus time display (A-scope) showing the problem analyzed.

The target return may or may not fall within the ground clutter return. Its position is a function of antenna beamwidth, depression angle, satellite altitude, and target altitude. Clearly, if the target is on the ground it will be imbedded in the clutter and other techniques must be used to separate the target and the clutter. However, when the target is above the surface of the earth, there is a combination of the above mentioned parameters which result in the target being at a range closer than the minimum range of the clutter.

B.2 Mathematical Development

Figure B-4 defines the terminology in the AOB plane shown in Fig. B-1. The two quantities that must be solved for are the maximum target range, $R_{t_{max}}$, and the minimum range to the ground clutter. These two occur at opposite edges of the antenna beam. The minimum range to the clutter is given by AC. From the law of sines for triangle AOC

$$R_{t_{min}} = R_e \left(\frac{\sin \alpha_1}{\sin \gamma_1} \right) \tag{1}$$

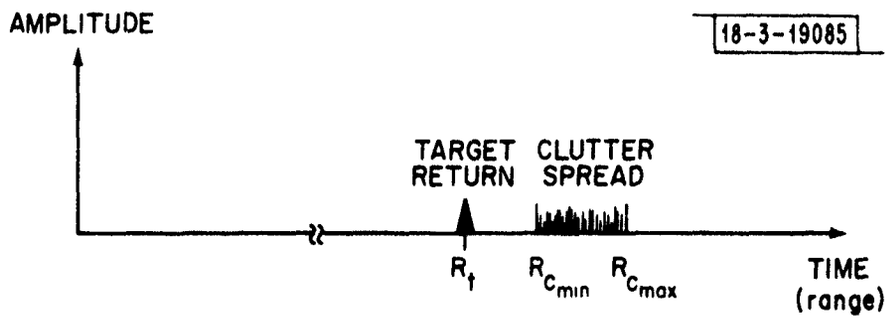


Fig. B-3. A-scope display.

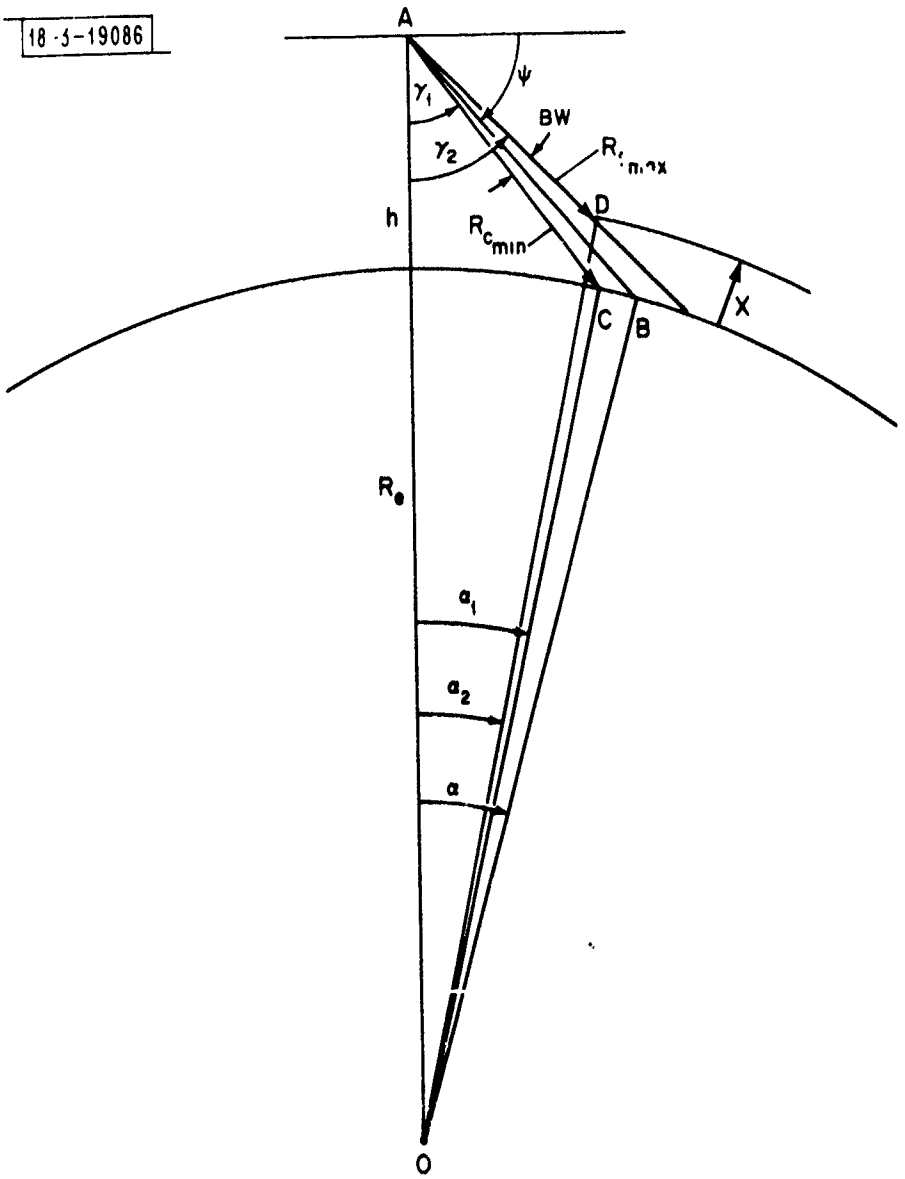


Fig. B-4. Terminclogy in AOB plane.

where

$\gamma_1 = \pi/2 - (\psi + BW/2)$

ψ = depression angle

BW = 3 dB radar beamwidth

α_1 = earth central angle

$$\alpha_1 = \pi - \sin^{-1}\left[\left(\frac{R_e + h}{R_e}\right)\sin\gamma_1\right] - \gamma_1 \qquad (2)$$

In a similar manner the maximum range to the target is given by

$$R_{t_{max}} = R_e\left(\frac{\sin\alpha_2}{\sin\gamma_2}\right) \qquad (3)$$

where

$\gamma_2 = \pi/2 - (\psi - BW/2)$

$$\alpha_2 = \pi - \sin^{-1}\left[\left(\frac{R_e + h}{R_e + x}\right)\sin\gamma_2\right] - \gamma_2 \qquad (4)$$

The range separation between clutter and target is given by

$$\Delta R = R_{c_{min}} - R_{t_{max}} \tag{5}$$

$$\Delta R = R_e \left[\frac{\sin \alpha_1}{\sin \gamma_1} - \frac{\sin \alpha_2}{\sin \gamma_2} \right] \tag{6}$$

Positive solutions of equation 6 indicate when the target is at a range less than the clutter and range gating can be used to eliminate the clutter. Negative solutions of equation 6 indicate regions where Doppler filtering must be employed to separate the target from the clutter. Equation 6 has been evaluated as a function of the four variables; satellite altitude, target altitude, depression angle and 3 dB antenna beamwidth. The results are presented in the next section.

A satellite-borne search system, to be cost effective, should cover as large a portion of the earth's surface as possible, otherwise the system will require a large number of satellites. The ground swath width in this system depends on the satellite altitude, depression angle and scan angle. Consider the plane defined by the intersection of the cone scan pattern and the earth as shown in Fig. B-5 for which the following definitions apply.

$\overset{\frown}{EF}$ is a great circle arc whose length is $2R_e\alpha$

α is the earth central angle defined in Fig. B-1

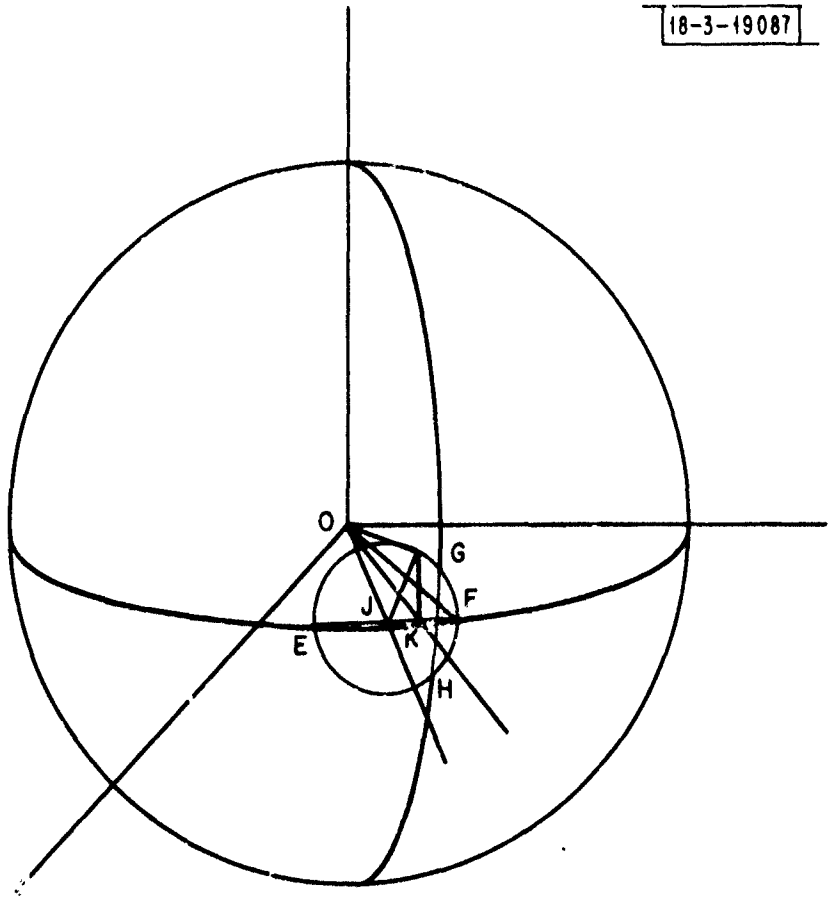


Fig. B-5. Intersection of cone scan and the earth.

$\overset{\frown}{GH}$ is a great circle arc whose length is the desired ground swath width

$\angle KJG = \delta$ the required half scan angle

Given the above, the components of triangle KJG can be determined to be

$$\overline{KG} = R_e \sin\left(\frac{SW}{2R_e}\right) \tag{7}$$

$$\overline{JG} = R_e \sin \alpha \tag{8}$$

The required half scan angle, δ , to achieve a particular swath width can be determined from

$$\delta = \sin^{-1}\left[\frac{\sin\left(\frac{SW}{2R_e}\right)}{\sin \alpha}\right] . \tag{9}$$

Equation 9 is used in the next section to determine the swath width limits.

B.3 Discussion of Results

In this section the results of the analysis are presented in graphical form. The range separation between target and clutter is plotted as a function of depression angle. Satellite altitude,

3 dB radar beamwidth and target altitude are parameterized.

Figures B-6 through B-8 show the range separation versus depression angle for a target at 10 km altitude and beamwidths of 0.1, 0.2 and 0.3 degree respectively. Satellite altitude is parameterized on each curve from 1000 to 6000 km. There are two limits shown on each curve. These are the earth's limb which occurs at small depression angles and an arbitrary 1000 nautical mile swath width limit. Operation on the dashed portion of the curves is possible at smaller swath widths.

Figures B-9 and B-11 show similar results for targets at 8 km altitude and Figs. B-12 through B-14 show the results for targets at 6 km altitude.

These figures indicate that range gating may be used for a large range of satellite altitudes against targets at altitudes to 6 km and below. As the 3 dB radar beamwidth is increased, the region where this technique is applicable diminishes. For example, at satellite altitudes above 1000 km and a 3 dB radar beamwidth of 0.3 degree. targets below 6 km altitude will be at ranges comparable with the ground clutter if a 1000 n.mi. wide ground swath must be covered.

B.4 Summary

An analysis has been performed to show the feasibility of using range gating as a technique to eliminate main lobe ground

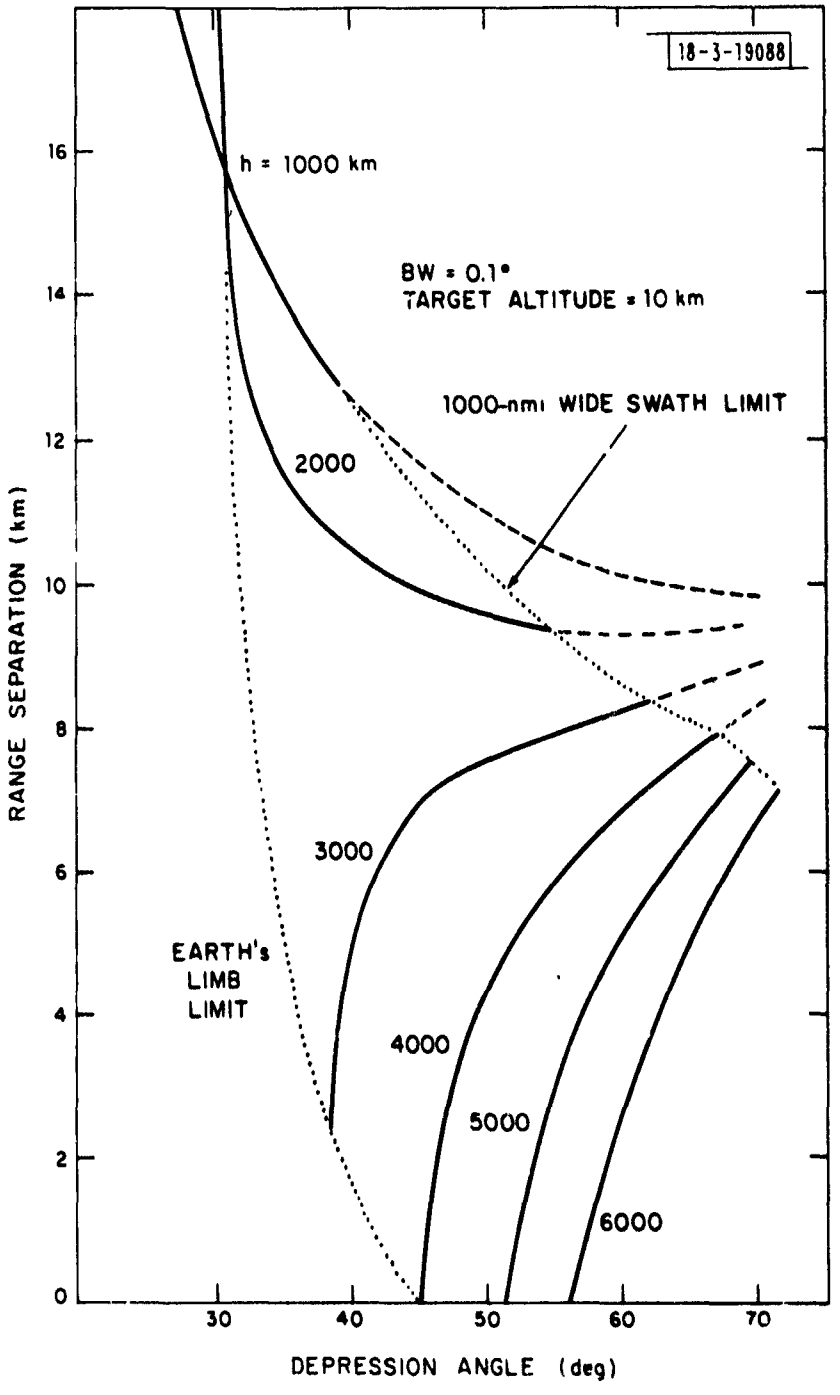


Fig. B-6. Range separation vs. depression angle.

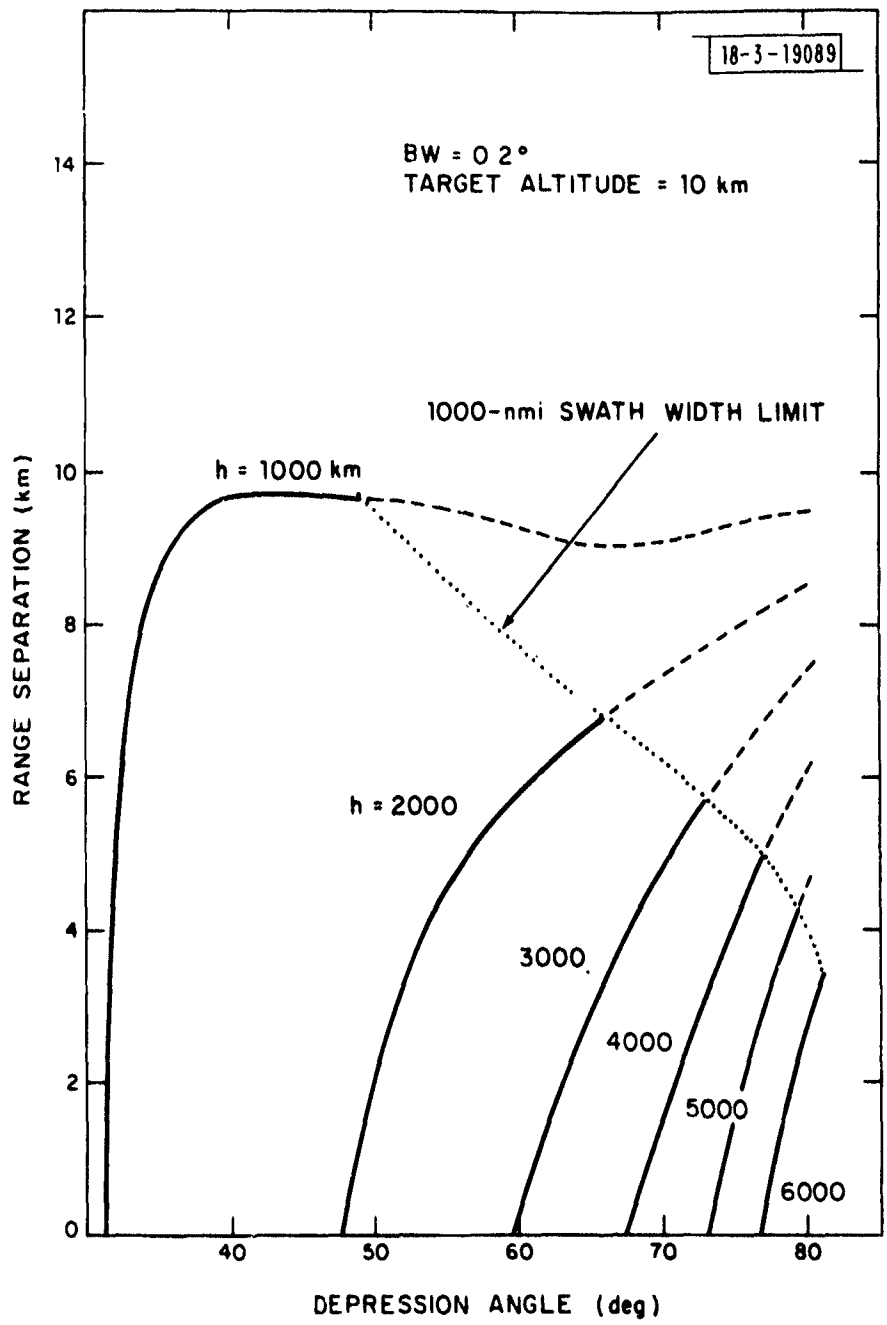


Fig. B-7. Range separation vs. depression angle.

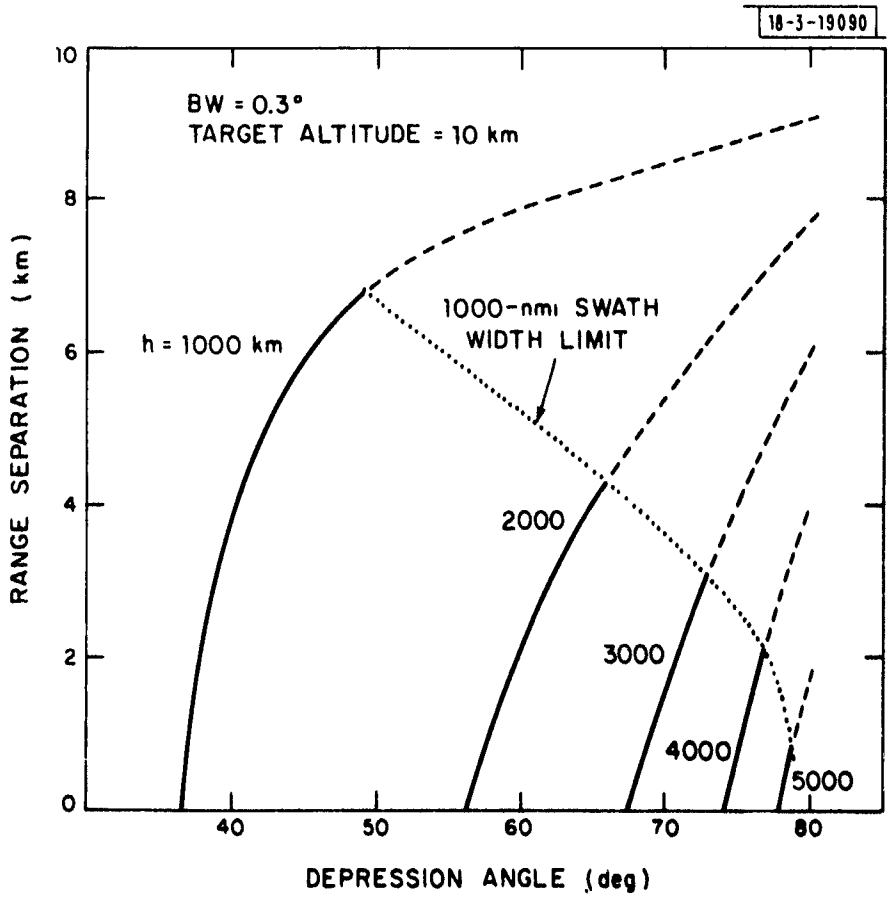


Fig. B-8. Range separation vs. depression angle.

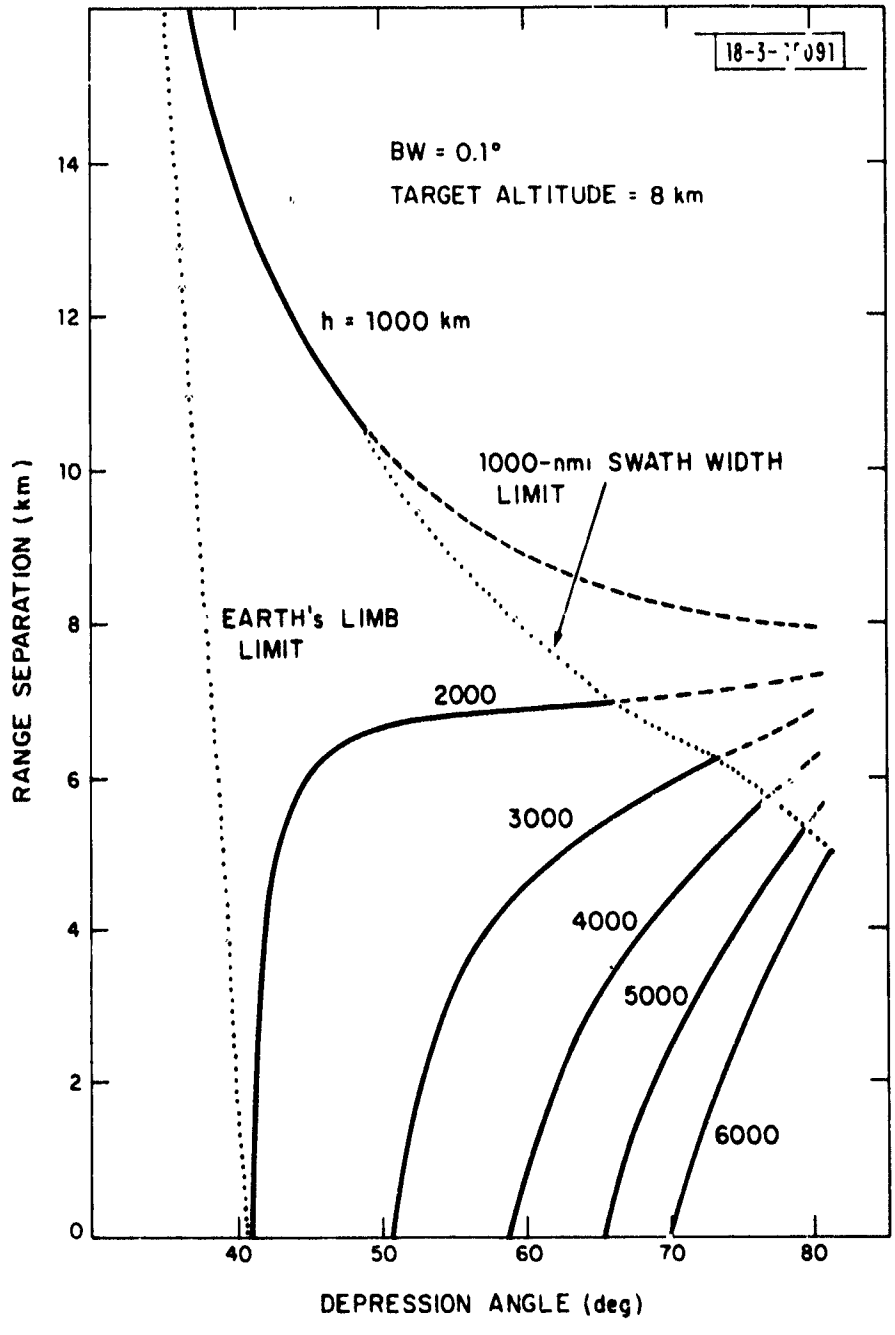


Fig. B-9. Range separation vs. depression angle.

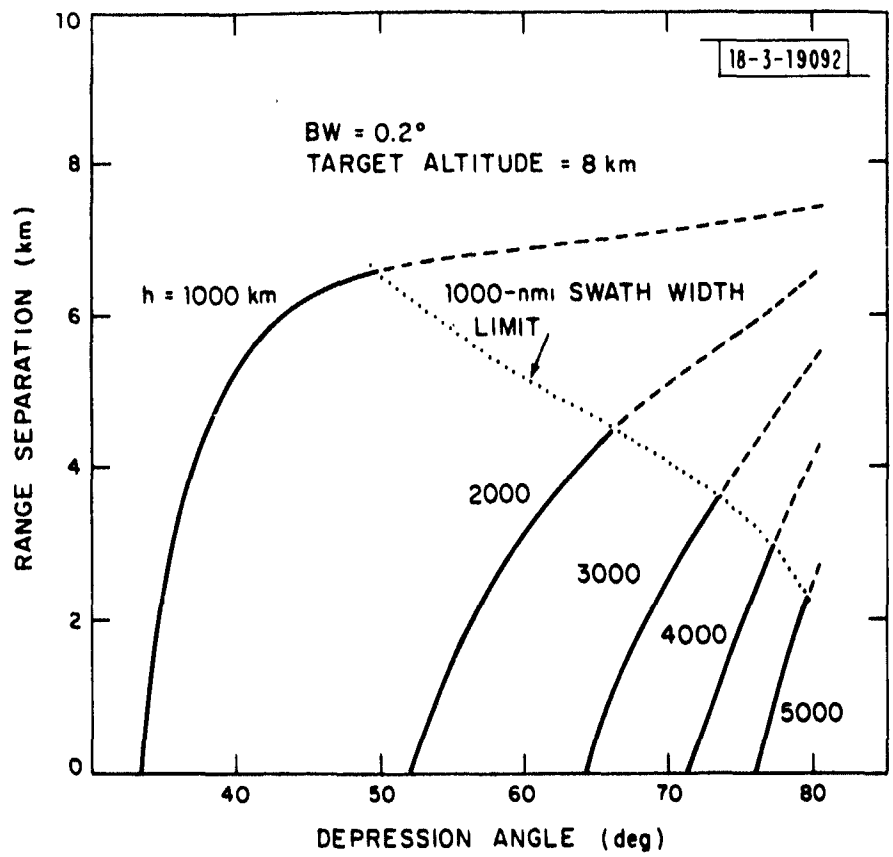


Fig. B-10. Range separation vs. depression angle.

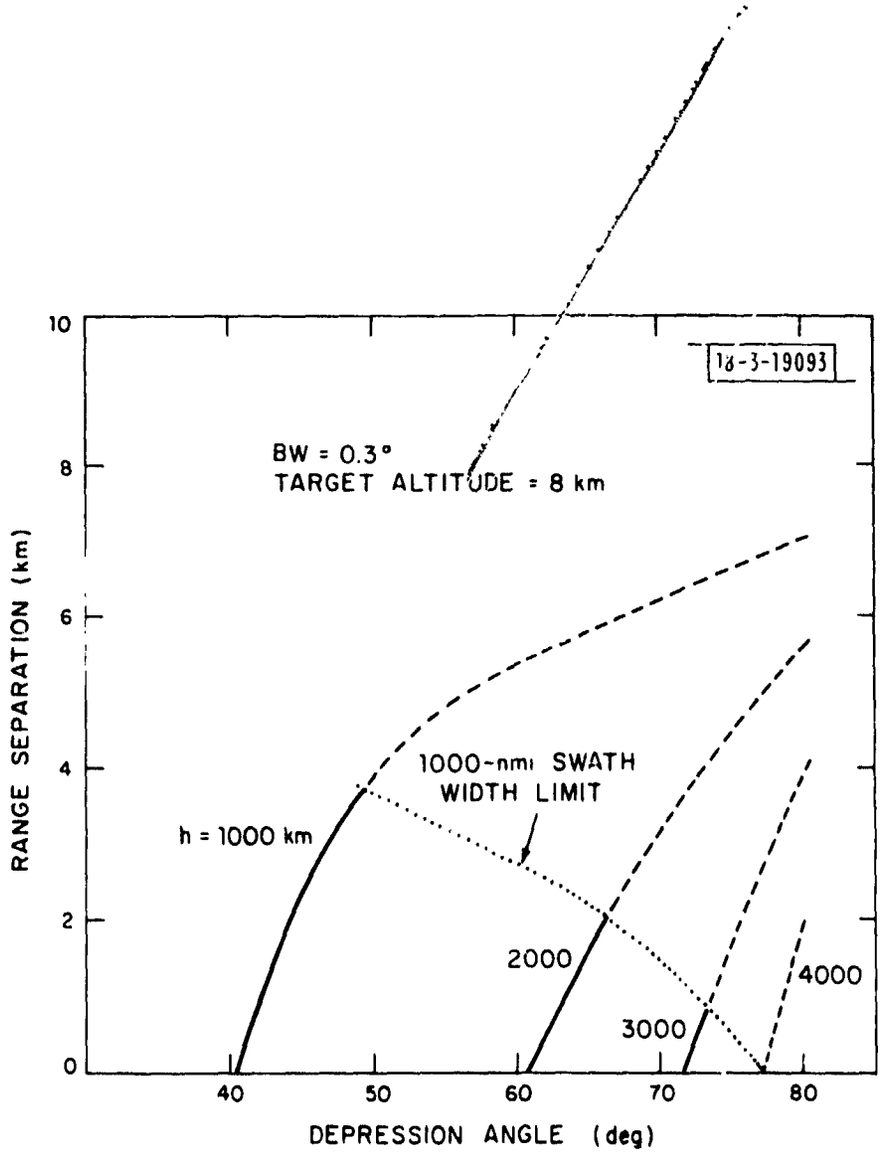


Fig. B-11. Range separation vs. depression angle.

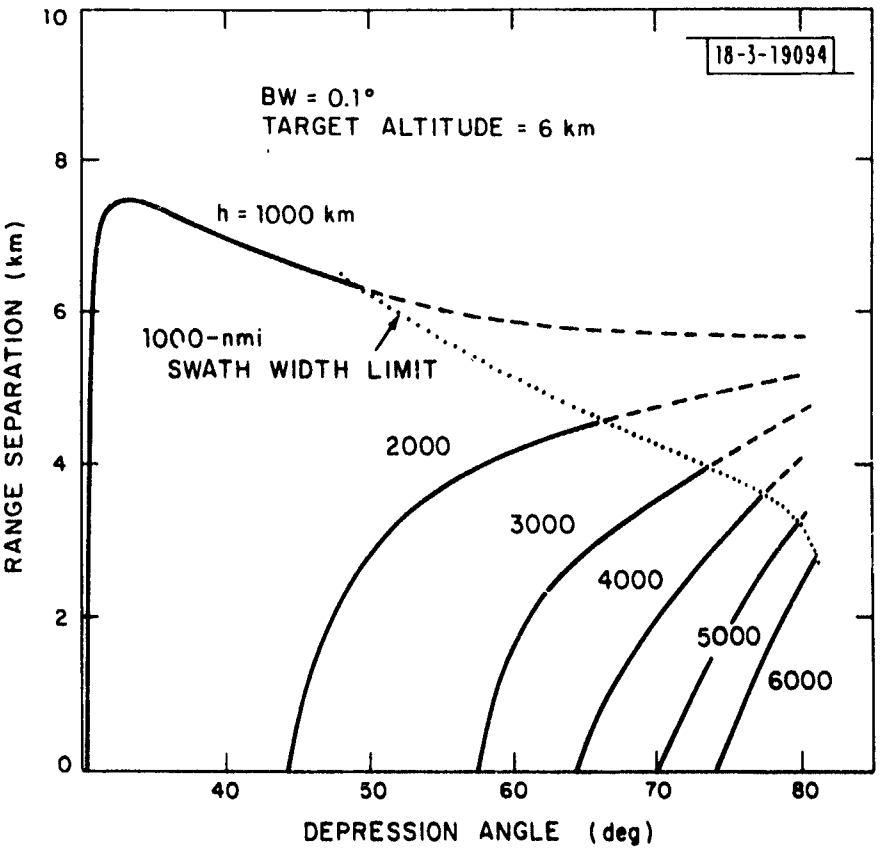


Fig. B-12. Range separation vs. depression angle.

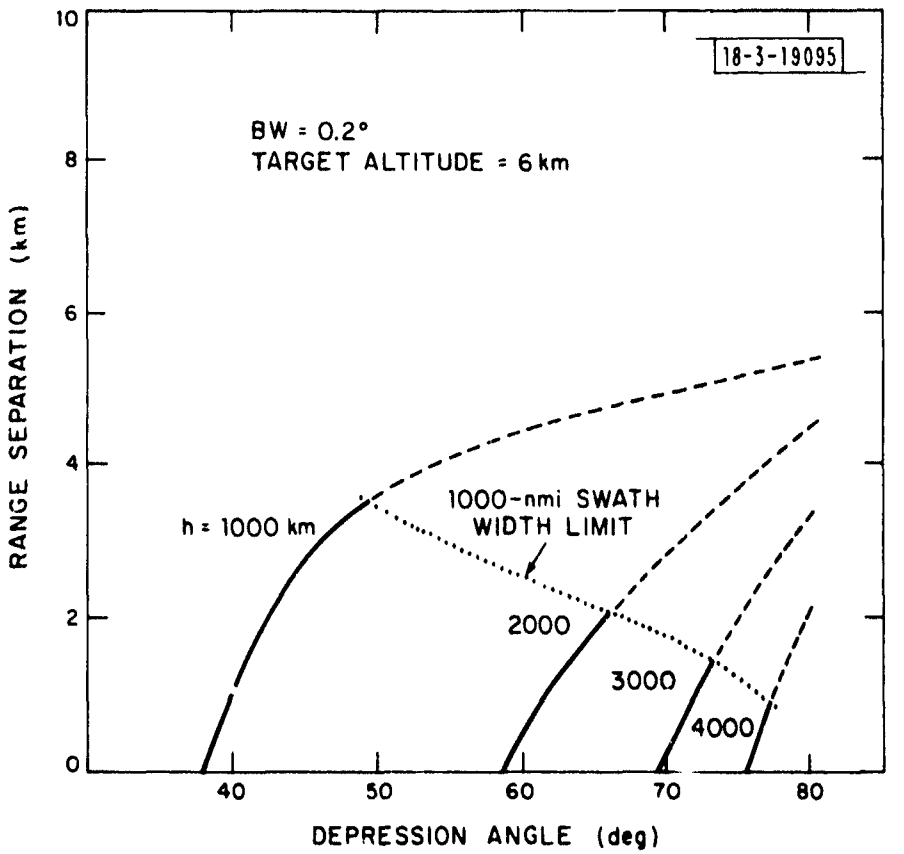


Fig. B-13. Range separation vs. depression angle.

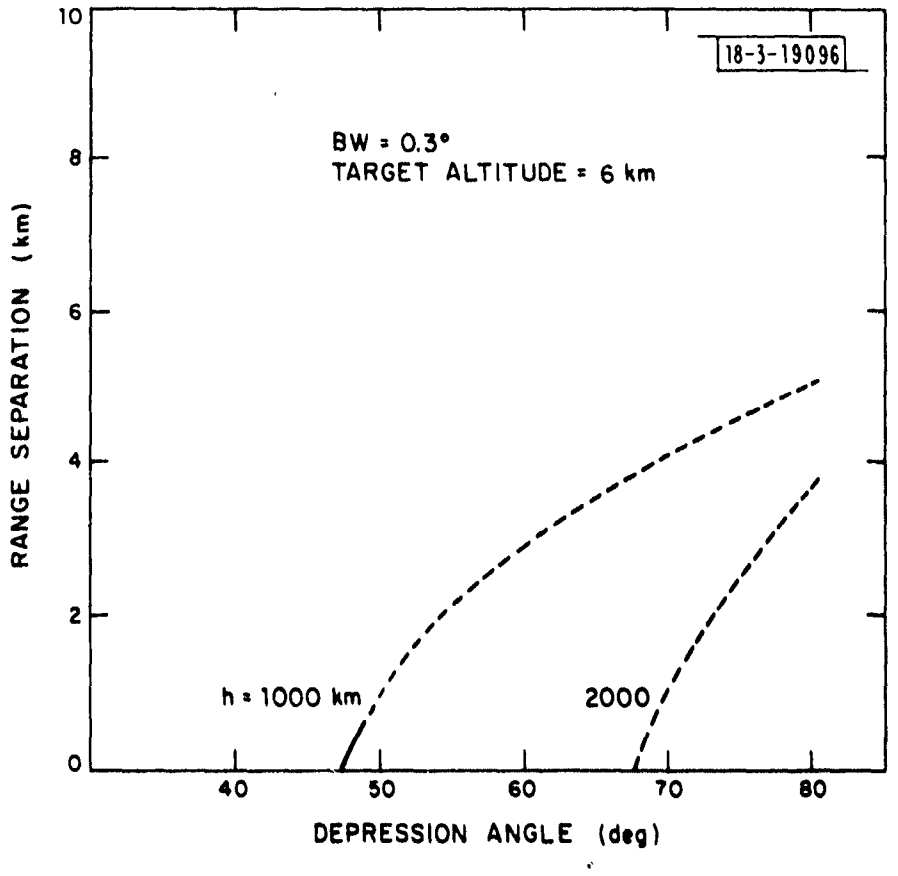


Fig. B-14. Range separation vs. depression angle.

clutter from the radar return in a satellite-borne radar searching an altitude regime above the surface of the earth. A wide range of satellite altitudes, target altitudes, sensor depression angle and beamwidths were investigated. This technique appears to be feasible for target altitudes above 6 km and 3 dB radar beamwidths smaller 0.3 degree. Operation against lower altitude targets is possible at the expense of covering a smaller ground swath.

REFERENCES

1. K. M. Siegel, H. A. Alperin, R. R. Bronski, J. W. Crispin, C. E. Schensted, I. V. Schensted "Bistatic Radar Cross-Sections of Surfaces of Revolution", Applied Physics 26, 297-305 (March 1955).

2. W. H. Peake, J. L. Oliver "The Response of Terrestial Surfaces at Microwave Frequencies", Technical Report AFAL-TR-70-301, Electro Science Laboratory, Ohio State University (May 1971), DDC-AD-884106.

3. Ibid.

4. "Spaceborne Radar Study Final Report" Grumman Report Number 74-21AF-1, Grumman Aerospace Corporation, Bethpage, N.Y.

5. M. I. Skolnik, "Radar Handbook" Chapter 28 (McGraw-Hill, New York, 1970).

6. D. K. Barton, "Radar System Analysis" (Prentice-Hall, 1964) Table 3.3, pg. 100.

7. L. Rabiner, B. Gold, "Theory and Application of Digital Signal Processing", (Prentice-Hall, 1975).

8. Ibid. Page 194, Computer Program by Jim McClellan, Rice University April 13, 1973.

UNCLASSIFIED

SECURITY CLASSIFICATION OF THIS PAGE (When Data Entered)

REPORT DOCUMENTATION PAGE	READ INSTRUCTIONS BEFORE COMPLETING FORM
1. REPORT NUMBER: ESD-TR-77-169	2. GOVT ACCESSION NO.	3. RECIPIENT'S CATALOG NUMBER
4. TITLE (and Subtitle): Waveform and Clutter Filter Design for a Satellite-Borne Bistatic Radar for Aircraft Detection	5. TYPE OF REPORT & PERIOD COVERED: Technical Note
	6. PERFORMING ORG. REPORT NUMBER: Technical Note 1977-7
7. AUTHOR(S): Robert A. Goundry and Chester J. Kurys	8. CONTRACT OR GRANT NUMBER(S): F19628-76-C-0002
9. PERFORMING ORGANIZATION NAME AND ADDRESS: Lincoln Laboratory, M.I.T., P.O. Box 73, Lexington, MA 02173	10. PROGRAM ELEMENT, PROJECT, TASK AREA & WORK UNIT NUMBERS: ARPA Order-600, Program Element No. 62301E, Project No. 7E20
11. CONTROLLING OFFICE NAME AND ADDRESS: Defense Advanced Research Projects Agency, 1400 Wilson Boulevard, Arlington, VA 22209	12. REPORT DATE: 28 June 1977; 13. NUMBER OF PAGES: 152
14. MONITORING AGENCY NAME & ADDRESS (if different from Controlling Office): Electronic Systems Division, Hanscom AFB, Bedford, MA 01731	15. SECURITY CLASS. (of this report): Unclassified; 15a. DECLASSIFICATION DOWNGRADING SCHEDULE

16. DISTRIBUTION STATEMENT (of this Report)

Approved for public release; distribution unlimited.

17. DISTRIBUTION STATEMENT (of the abstract entered in Block 20, if different from Report)

18. SUPPLEMENTARY NOTES

None

19. KEY WORDS (Continue on reverse side if necessary and identify by block number)

aircraft detection
satellite-borne radar
clutter filtering
waveform designs
clutter suppression
bistatic radar

20. ABSTRACT (Continue on reverse side if necessary and identify by block number)

Waveform and clutter filtering for the detection of moving aircraft in the presence of ground clutter by a spaceborne bistatic radar are described. The waveform designs are based on mappings of the aircraft and clutter onto the bistatic range-Doppler plane. Low sidelobe digital filter designs for the required clutter rejection, coverage characteristics of a bistatic radar on representative satellite orbits, and system requirements for a North American surveillance fence for bomber detection are included.

DD FORM 1 JAN 73 1473 EDITION OF 1 NOV 65 IS OBSOLETE

UNCLASSIFIED

SECURITY CLASSIFICATION OF THIS PAGE When Data Entered

20760 1